11-7-2015

Structure of Methane Inverse Diffusion Flames with Pre-heated Co-flowing Simulated Combustion Products

Xisheng Zhao
University of Windsor

Structure of Methane Inversed Diffusion Flames with Pre-heated Co-flowing Simulated Combustion Products

By

Xisheng Zhao

A Thesis
Submitted to the Faculty of Graduate Studies
through the Department of Mechanical, Automotive & Materials Engineering
in Partial Fulfillment of the Requirements for
the Degree of Master of Applied Science
at the University of Windsor

Windsor, Ontario, Canada

2015

Structure of Methane Inversed Diffusion Flames with Pre-heated Co-flowing Simulated Combustion Products

by

Xisheng Zhao

APPROVED BY:

_____

Dr. R. Barron
Department of Mathematics and Statistics, Cross-appointment with Mechanical, Automotive & Materials Engineering

_____

Dr. D. Ting
Department of Mechanical, Automotive & Materials Engineering

_____

Dr. Andrzej Sobiesiak, Advisor
Department of Mechanical, Automotive & Materials Engineering

July 29, 2015

DECLARATION OF CO-AUTHORSHIP / PREVIOUS PUBLICATION

I. Co-Authorship Declaration

I hereby declare that this thesis incorporates material that is result of joint research, as follows:

This thesis incorporates the outcome of a joint research undertaken in collaboration with C. Barks and D. Haggith under the supervision of Dr. Sobiesiak. The collaboration is covered in Chapter 2 and 3 of the thesis.

This thesis also incorporates the outcome of a joint research undertaken in collaboration with Z. Movahedi under the supervision of Dr. Sobiesiak. The collaboration is covered in Chapter 2 and 4 of the thesis.

In all cases, the key ideas, primary contributions, experimental designs, data analysis and interpretation, were performed by the author. The contribution of C. Barks and Z. Movahedi were primarily through the provision of numerical analysis, and D. Haggith was primarily through the provision of assistance for building experimental setup in the associated publications for annual meetings, congress and conference.

I am aware of the University of Windsor Senate Policy on Authorship and I certify that I have properly acknowledged the contribution of other researchers to my thesis, and have obtained written permission from each of the co-authors to include the above materials in my thesis.

I certify that, with the above qualification, this thesis, and the research to which it refers, is the product of my own work.

II. Declaration of Previous Publication

This thesis includes 3 original papers that have been previously published for publication in peer reviewed conference proceedings, as follows:

Thesis Chapter	Publication title/full citation	Publication status
Chapter 2,3	Barks, C., Haggith, D., Zhao, X., and Sobiesiak, A., Structure of methane inversed diffusion flames with cooled co-flowing combustion products. *Combustion Institute Canadian Section Meeting*, Quebec City, Quebec, Canada, May, 2013.	Published
Chapter 2,3	Barks, C., Haggith, D., Zhao, X., and Sobiesiak, A., Structure and NO emissions from methane inversion diffusion flames with cooled co-flowing combustion products. *6th European Combustion Meeting*, Lund, Sweden, July, 2013.	Poster Presented
Chapter 2,4	Movahedi, Z., Zhao, X., and Sobiesiak, A., Structure of methane inversed diffusion flames with simulated preheated co-flowing combustion products. *Combustion Institute Canadian Section Meeting*, Windsor, Ontario, Canada, May, 2014.	Published
Chapter 2,4	Zhao, X., Movahedi, Z., and Sobiesiak, A., Structure of methane inversed diffusion flames with simulated preheated co-flowing combustion products. *35th International Symposium on Combustion,* San Francisco, California, USA, August, 2014	Poster Presented
Chapter 2,4	Zhao, X., Movahedi, Z., and Sobiesiak, A., Structure and Species Concentration of Methane Inversed Diffusion Flames with Co-flowing and Pre-heated Simulated Combustion Products. *Combustion Institute Canadian Section Meeting*, Saskatoon, Saskatchewan, Canada, May, 2015.	Published

I hereby certify that I own the copyright to the above materials. I certify that the above material describes work completed during my registration as a graduate student at the University of Windsor.

I certify that, to the best of my knowledge, my thesis does not infringe upon anyone's copyright nor violate any proprietary rights and that any ideas, techniques, quotations, or any other material from the work of other people included in my thesis, published or otherwise, are fully acknowledged in accordance with the standard referencing practices. Furthermore, to the extent that I have included copyrighted material that surpasses the bounds of fair dealing within the meaning of the Canada Copyright Act, I certify that I have obtained a written permission from the copyright owners to include such materials in my thesis and have included copies of such copyright clearances to my appendix.

I declare that this is a true copy of my thesis, including any final revisions, as approved by my thesis committee and the Graduate Studies office, and that this thesis has not been submitted for a higher degree to any other University or Institution.

ABSTRACT

The inversed diffusion flame (IDF) burner which is characterized by a double flame structure and ultra-low nitrogen oxide emissions has been studied at the lab scale in this work. This experimental study is intend to investigate the structure of co-axial non-premixed diffusion flames with inversed flow arrangement of methane and air, surrounded with combustion products from a lean flat flame, simulated combustion products, nitrogen and air. The co-flow stream is to simulate the possible gases surrounding the flames inside an industrial furnace. The previous numerical and experimental investigation has studied central air jet flows into the co-annular fuel jet, and then both mixing with the surrounded hot combustion stream from premixed lean flat flame. The present investigation is focused on the same initially non-premixed inversed arrangement with central air and fuel streams flowing into hot combustion products, air, and pre-heated simulated combustion products.

DEDICATION

This thesis is dedicated to my family,

I love you all, each and every one.

ACKNOWLEDGEMENTS

Four years ago, at my “supposed to be” last term of my undergraduate program, Dr. Andrzej Sobiesiak sparked my interest in thermodynamics and combustion in Internal Combustion Engine course, and I failed this course at the first time. He talked to me to stay in school for another year just to get myself ready for whatever was waiting for me when I graduate. The second time I took the IC Engine course the year after, fortunately I passed, and even more luckily, I have the opportunity to work with Dr. Sobiesiak as his graduate student to pursue research on combustion. He was always there to give me very useful advice when I was facing difficult and frustrating times, and also asking questions to guide me how I should look at those things from different ways. As he left me a lot of freedom to try different ideas during my research, I learned different perspectives beyond the research project itself. I thank him for giving me the second chance, his help and support.

I thank Bruce Durfy for his support and advice for making the experimental setup, as I constantly bothered him for seeking help, he was always happy to deal with the problem I had, no matter how busy he was. His effort for teaching me the machining skills and working properly in the shop is invaluable and I really appreciated that. Thanks to Andrew Jenner as he was another major support for making the experimental setup, also he was the other person constantly who I was bothering with. He took care of the problems I had for the burner and other parts of the setup, and also he was willing to give very useful advice to improve it.

I like to appreciate Gangyong Zhang and Steve Budinsky at the Technical Support Centre for additional assistance with the control electronic hardware and machining; to Patrick Seguin for his help with the electric control boxes; to Dean Poublon for his help with supporting in the lab; and to Rose Gignac, Barb Denomey and Suzan Jappy for their administration assistance.

I thank Indika Gallage and Iain Cameron for their help and support of designing and fabricating the experiment facilities; to Zakaria Movahedi for his assistance of numerical modelling of this

project; to Christopher Barks and Nguyen Anh Tuan for their advice and support for my course work; to Dr. Vladmir Bokov for his advice on Design of Experiment; to Dale Haggith for his help initiating this project and technical support. I really appreciated the friendship we had in our research group, providing me such a wonderful place to research, study, and enjoy.

This work was funded by Auto 21and University of Windsor Faculty of Graduate Studies, I like to thank them for the grateful financial support of this project.

I thank my parents, Zhao Chuan and Wang Rongfen for their unconditional love and support for all these 7 years of study in Canada. Without them, I cannot be in part of this project, and cannot pursue the research in combustion.

TABLE OF CONTENTS

LIST OF TABLES

LIST OF FIGURES

LIST OF APPENDICES

LIST OF ABBREVIATIONS

IDF	Inversed diffusion flame
LCV	Also known as the Low Heating Value (LHV), it is determined by subtracting the heat of vaporization of the water vapor from the higher heating value.
LPM	Liters per minute
NDF	Normal diffusion flame
PAH	Polycyclic-aromatic-hydrocarbon
PLIF	Planar laser-induced fluorescence

NOMENCLATURE

A	Reaction frequency factor
E_a	Activation energy
I_u	$I_u \equiv \upsilon^{-1} \int_0^\infty u^2 r dr$
K_V	Recirculation rate
$\dot{M}_A$	Mass flow rate for air jet in the burner reaction zone
$\dot{M}_E$	Mass flow rate for the exhaust gas jet
$\dot{M}_F$	Mass flow rate for the hydrocarbon fuel jet
T	Average temperature of all measured temperatures from different locations in the furnace
T_i	Measured temperature at certain location
T_u	Temperature uniformity ratio
Γ	Exchange coefficient of fuel gas
k	Reaction rate coefficient
r	Radius
$r_{\frac{1}{2}}$	Radius at which the velocity has one half its axial velocity
u	Axial velocity
υ	$\upsilon \equiv \frac{\mu}{\rho} = \frac{\Gamma}{\rho}$
x	Width of a jet
x_c	Confluence point of the fuel and air jets
$\theta_{1,o}$	Angle between the axes
θ_{12}	Port-separation angle
λ	Excess air coefficient
μ	Viscosity
ρ	Density
φ	Equivalence ratio
ψ_{12}	Typical momentum flux ratio

CHAPTER 1

Introduction

1.1 Flameless Oxidation

Flameless oxidation is a mode of combustion which is characterized by the large extended reaction zone with no definite visible flame; it provides more uniform heat transfer to the load. Inside the furnace, fuel and air jets react with combustion products which have cooled down by heat transfer to the load creating the flameless oxidation regime. The concept of flameless oxidation was first introduced for around 70 years ago.

In order to minimize formation of nitrogen oxides and produce an oxidation effluent, Bell and McGill (1983) attempted to burn the stream which contained nitrogen oxides at 1093℃ and above, using excess amount of reducing agent, which led to flameless oxidation. This process allows combustion with much lower equivalence ratio. Wünning and Wünning (1997) pointed out the key features of flameless oxidation, in which the thermal NO emission can be reduced even with high air pre-heating temperature; the flameless oxidation could occur in the combustion chamber with

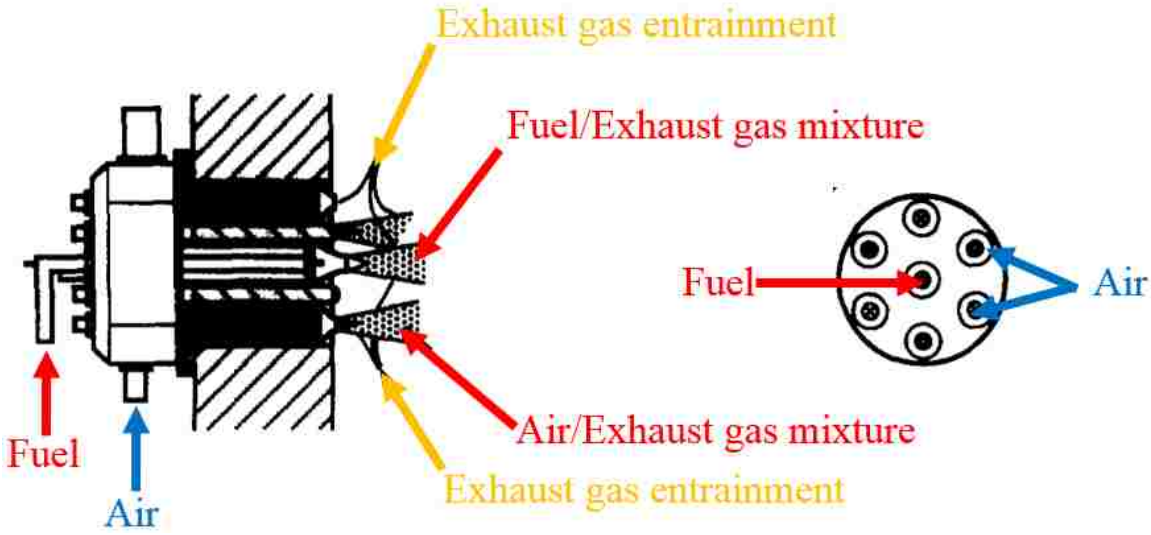

[redacted]

temperature higher than 800 °C; flameless oxidation occurs without any visible or audible flame at optimized condition. Their regenerative burner which operated in both flame and flameless oxidation mode contained mainly two jets, the central fuel jets and co-flow air jets. The exhaust gas was entrained and mixed with these two jets as shown in Figure 1.1, forming the reaction zone of fuel/exhaust gas mixed jets, plus air/exhaust gas mixed jets. This burner is designed to enhance the recirculation of the exhaust gas. The recirculation of the exhaust gas and mixing of the other two jets are the key factors for flameless oxidation. Wünning and Wünning (1997) characterized the recirculation rate by the following factor

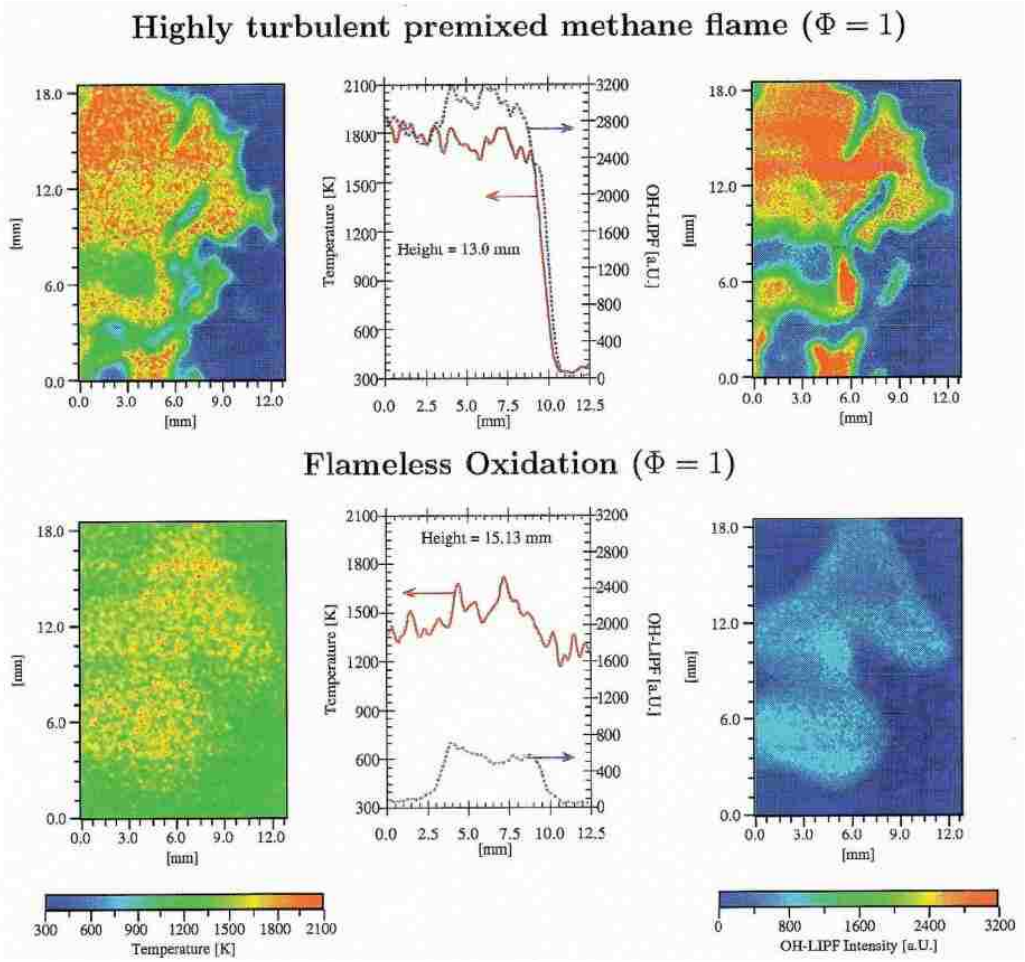

$$K_V = \frac{\dot{M}_E}{\dot{M}_F + \dot{M}_A} \tag{1.1}$$

where $\dot{M}$ is the mass flow rate for (E) as the exhaust gas jet, (F) as hydrocarbon fuel jet and (A) as air jet in the burner reaction zone. They found that to obtain the flammable mixture, the recirculation rate K_V should be equal or less than 0.5, and with even more reliable operation condition, K_V should be equal or less than 0.3. They explored the stability limits for flameless oxidation, and plotted the schematics of the stability limits over the stable flame, unstable flame and flameless oxidation by applying different recirculation rates.

Plessing et al. (1998) explored the actual difference of temperature and OH specie for flame and flameless oxidation by using laser measurement techniques as shown in Figure 1.2. Comparing with the turbulent flame mode with flameless oxidation mode, the peak temperature region is much lower in flameless oxidation mode, and temperatures are more uniformly distributed. Their finding has been confirmed by OH Laser-Induced Photodissociation and Fluorescence. The intensity of OH is much less in flameless oxidation mode, and more uniformly distributed. The results they obtained identifies the key features of the flameless oxidation.

As flameless oxidation shows dramatically decreased peak temperatures, the NO_x emissions also get affected. Mancini et al. (2002) has investigated the behavior of NO_x with numerical simulation and experimental validation. They found out that NO_x is formed in an elongated, thin shear layer located between the natural gas jet and the air jet, and NO_x is formed mainly by the thermal mechanism. The prompt NO plays a small role in NO_x formation process. Also, NO re-burning mechanism is negligible in the analyzed case. Cho et al. (2011) studied the behavior of a 300 kW_{th} regenerative multi-burner flameless oxidation furnace and tested two firing modes as shown in Figure 1.3. Lower NO emission was achieved by the parallel firing mode rather than the staggered mode, and the main reason for this phenomenon is related to the higher temperature uniformity ratio which is defined as

$$T_u = 1 - \sqrt{\frac{1}{N}\sum_{i=1}^{N}\left(\frac{(T_i - \bar{T})}{\bar{T}}\right)} \quad (1.2)$$

where T_i is the measured temperature at a certain location (i) and $\bar{T}$ is the average temperature of all measured temperature from different locations in the furnace. The temperature uniformity ratio T_u is in the range of 0 to 1, and 1 indicates perfectly uniform temperature inside the furnace. The CO emissions only slightly differ between parallel and staggered modes and the CO concentration is less than 40 ppm, which is relatively low.

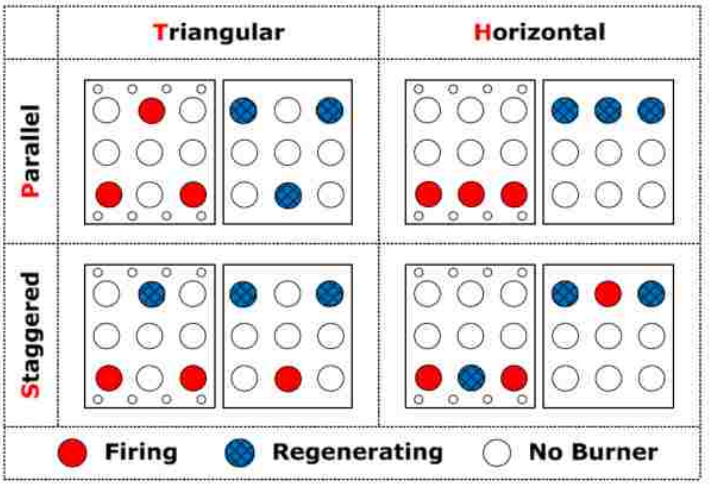

[redacted]

A large amount of work has been done on fairly large-scale furnaces, the regenerative burner which could be like refractory lined furnace with an 2 × 2 m cross-section and a length of 6.25 m (Mancini et al., 2002). Flamme (2004) investigated the FLOX® burner under gas turbine conditions. Different types of flameless oxidation burners were studied, the single nozzle burner, multi-air nozzle burner and a range of single nozzle burners. The results from experiment and numerical simulation indicate the lowest NO_x and CO emission has been achieved by the arrangement of several single nozzles FLOX® burners. For λ ratio of 2 and 2.5, NO_x emissions are between 1 and 3 ppm, and carbon monoxide is less than 10 ppm. Danon et al. (2010) has tested

flameless oxidation in a prototype FLOX® gas turbine combustor both numerically and experimentally. The Low Calorific Value (LCV) gas has been introduced as the primary fuel which is produced by a catalytic auto-thermal reforming unit. A mixture of CH_4, CO, CO_2, N_2 and H_2 has been fed into the reforming unit. The ultra-low emission combustion has been achieved, and two different recirculation zones were identified from calculation results. 90% of the NO was formed by the nitrous oxide mechanism, and rest 10% is formed by the thermal mechanism.

Sobiesiak et al. (1998) has investigated performance characteristics of the novel low-NO_x CGRI burner. The resultant combustion has the feature of visually flameless, which in this case they prefer to reaction zone as combustion zone rather than flames. It enabled the usage of high air pre-heating by matching with NOx emission standards. With the appropriate choice of fuel and oxidant port angles and spacing, the reasonably short, compact burner combustion zone has been achieved. FODI (Fuel/Oxidant Direct Injection) non-premixed firing strategy has been applied. Because FODI primarily depends on adequate entrainment by the fuel and oxidant jets of recirculation of the furnace gases (primarily combustion products) which has been cooled by heat transfer to the surroundings. The burner configuration has the clear advantage to enhance the entrainment, a large number of fuel and oxidant ports to shorten the burner combustion zones plus promotes stability, and with two common features in most furnace combustion chamber, namely ample of presence of cooled product gases, also the momentum of the fuel and oxidant feed-streams.

In achieving the flameless oxidation, the characteristics of individual jets play the key role. Ver ssimo et al. (2013) has examined the importance of the inlet air velocity on establishing the flameless combustion in a 10 kW laboratory scale combustor. As their results shows, by increasing the inlet air velocity, flameless combustion condition remains almost in the same region of the combustor, as the main reaction zone remains constant $\lambda = 1.3$. When $\lambda > 1.7$, flameless oxidation could be established regardless of the change in air jet momentum. It indicated that the central high-momentum air jet surrounded by a number of low-momentum fuel jets may have some difficulties to establish the flameless oxidation with the dilution of substantial amount of flue gases.

1.2 Fuel Reformation

Fuel reformation is a method to generate hydrogen or hydrogen-enriched products from hydrogen fuels such as natural gas. Since hydrogen has the property to significantly enlarge the flammable region and extend the flammability region to much lower equivalence ratio. Rabenstein and Hacker (2008) indicated the possible operation modes for hydrogen production by ethanol reforming as:

- Steam reforming;
- Partial-oxidation;
- Auto-thermal reforming.

1.2.1 Steam Reforming

Haryanto et al. (2005) claimed steam reforming of natural gas to produce hydrogen to be the most energy-efficient technology at that time, as this process can extract H_2 from both hydrocarbon fuels and water. Otsuka et al. (1998) indicated steam reforming is a highly endothermic reaction, so the high temperature which normally greater than $900℃$ is a need and large amount of energy is consumed to drive this reaction. The ideal steam reforming for methane is:

$$CH_4 + H_2O \rightarrow CO + 3H_2,\ \Delta H = +49.3\ kcal/mol \tag{1.3}$$

1.2.2 Partial-oxidation Reforming

Compared with steam reforming, the partial oxidation of methane is an exothermic reaction. The reaction can proceed at moderate temperature which is less than $500℃$ ideally. In reality the direct partial oxidation of methane is very difficult to achieve, due to partial oxidation process gets complete oxidation of methane to CO_2 and H_2O and steam reforming of remaining CH_4 with H_2O involved in. To resolve this issue, higher temperature $(> 800℃)$ is required to obtain high

selectivity of H_2 and CO, due to the reformatting reaction's limitation of thermodynamic equilibrium at low temperature. The ideal partial-oxidation for methane is:

$$CH_4 + 0.5O_2 \rightarrow CO + 2H_2,\ \Delta H = -8.5\ kcal/mol \quad (1.4)$$

1.2.3 Auto-thermal Reforming

Hoang and Chan (2004) defined the auto-thermal reforming as the combination reaction of partial-oxidation and steam reforming under thermally neutral conditions and with consideration of heat loss to the surroundings. There are basic eight auto-thermal related reactions come from both partial oxidation and steam reforming of methane, and they have been split to two streams of reactions. Sets of reactions include containing exothermic complete oxidation, followed by steam reforming, water-gas shift, and CO_2-reforming reactions of methane, and the second stream includes the cracking of methane and carbon monoxide to carbon deposition, plus gasifying carbon by steam and oxygen. Among these eight reactions, some reactions proceed with the combination of the others, while some has significantly low rate of reactions. The four major reactions to be considered is the exothermic complete combustion of a fraction of feed methane:

$$CH_4 + 2O_2 \rightarrow CO_2 + 2H_2O, \Delta H_{1(298)} = -802000kJ/kmol \quad (1.5)$$

With the endothermic steam reforming reaction to CO:

$$CH_4 + H_2O \leftrightarrow CO + 3H_2, \Delta H_{2(298)} = 206000kJ/kmol \quad (1.6)$$

Accompanied by a water-gas shift:

$$CO + H_2O \leftrightarrow CO_2 + H_2, \Delta H_{3(298)} = -41000kJ/kmol \quad (1.7)$$

Some methane steam-reformed directly to CO_2:

$$CH_4 + 2H_2O \leftrightarrow CO_2 + 4H_2, \Delta H_{4(298)} = 165000kJ/kmol \quad (1.8)$$

To operate the auto-thermal reformer, the catalyst of the reformer need to be heated up to 300℃ to lead the auto-thermal reaction to self-active proceed with predetermined mixture of methane, air and water. The main advantage of auto-thermal reforming is the thermal energy generated from partial oxidation can be absorbed by stream reforming as these two processes simultaneously occurring in the reactor.

1.3 Inversed Diffusion Flame

Mikofski et al. (2006) stated the Inversed Diffusion Flames (IDFs) are similar to normal diffusion flames (NDFs), and the difference is the exchanged relative position of fuel and oxidizer. The temperature and mixture fraction histories to form soot and polycyclic aromatic hydrocarbon (PAH) are different, and these soot and PAH escape to the surroundings without oxidization since they do not need to travel pass the high temperature reaction zone. A lot of studies have been done on different aspects of normal diffusion flames and also inversed diffusion flames. The following schematics in Figure 1.4 and Figure 1.5 compare a laminar NDF burner and IDF burner:

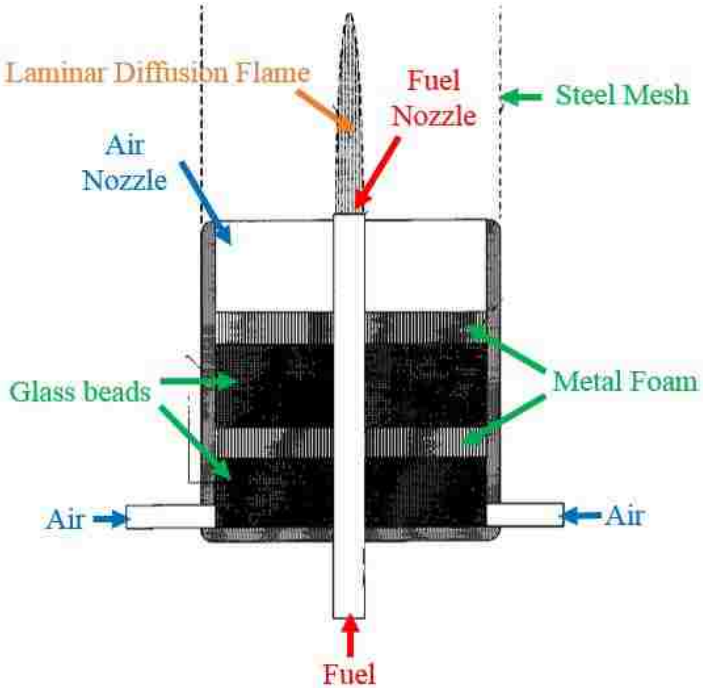

Wu and Essenhigh (1985) first identified six different flame types of methane inversed diffusion flame in one map. Only two types of flame had similar behavior that could represent IDF, and these flames occupied over 50% of total flame map. The Burke-Schumann flame (Burke and Schumann, 1928) surface with instantaneous reaction was used as the prediction model. The measurement of radial and axial temperature and species concentration profile were agreed with calculation results.

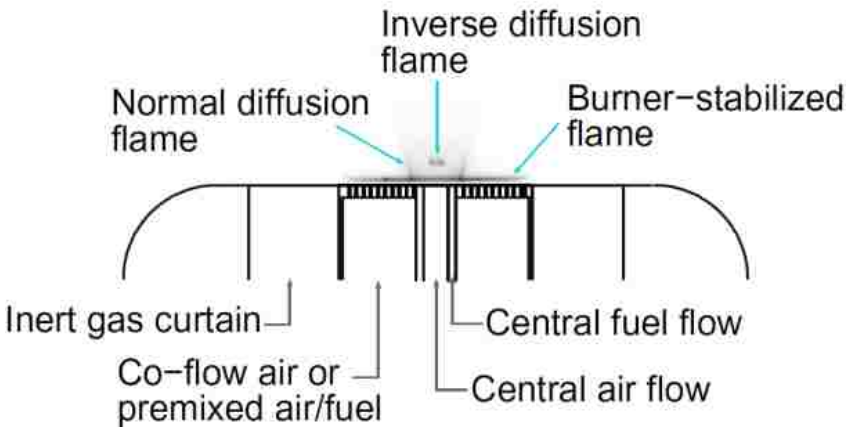

[redacted]

Sobiesiak and Wenzell (2005) extended the investigation of characteristics and structure for non-premixed flames of fuel/oxidizer direct injection and inversed fuel/oxidizer delivery. The results indicated velocity of the inner air jet and outer fuel jet has crucial impact of the flame length. By controlling velocity ratio, fuel/air nozzle diameter ratio, and fuel/air jet equivalence ratio, producing an extended uniform and high temperature region could be promising. The anchor diffusion flame at the nozzle could stabilize the whole flame by its presence. Johnson and Sobiesiak (2011) continued the studying of this non-premixed flame by adding a lean premixed, burner-stabilized methane/air flame as the source of combustion products to create the double flame structure. Both experimental measurements and numerical simulation had been applied to investigate IDFs. The hysteresis behavior had been found out by increasing of central air velocity, a partially premixed

flame was produced by mixing central air and fuel jets, and when the central velocity reached a critical level, the partially premixed flame propagated back and stabilized upstream closer to the burner face to from IDF.

The characteristics of inversed diffusion flame have investigated with different types of fuel and different burner configuration. Mikofski et al. (2006) studied the flame height associate with both ethylene and methane as primary fuel. They were using OH PLIF measurement, and it indicated that as luminous soot is above the reaction zone, the luminous height is greater than height of the reaction zone, so the luminous flame height is not effective to quantify the flame height. Sze et al. (2004) investigated the temperature distribution and heat transfer aspects of IDF with butane as fuel. The temperature profiles of the flame showed a cool core at low flame heights, and the maximum temperature region were presented instead at higher elevation. From the distribution combustion products, it shows high heat flux region is strongly bonded to where the intense reaction occurred, and the heat flux drops correspondingly where the post combustion is. Katta et al. (2005) studied the dynamics of IDF and how it affected the formation of PAH and soot by using ethylene as fuel. The results shows flame oscillation does not affect formation of radical and product species very significantly, but it has strong influence certain on slowly formed PAH species. Vortices at 17.2 Hz helped the mixing of species, resulting in more uniformly distribution of PAH species at downstream locations.

1.4 Thesis Objective

1) To identify the flame structures that occur when velocities and temperature of the central air, annular fuel flow and co-flow are changed. Different types of co-flow jets have been tested, namely air, nitrogen, combustion products produced by a burner stabilized lean flame and a synthetic gas to simulate the combustion products. Both the co-flowing combustion products and the simulated combustion products are representative of the furnace gases that air and fuel jests would entrain into.

2) To identify the operation conditions under fuel reformation and flameless oxidation. In some cases, the central fuel was delivered at various angles, and central air tube was raised above the burner surface to provide additional mixing time of central fuel/air and co-flow jets before the reactions, in order to create more homogenous mixture and enlarge the reaction zone. The pre-heating level of the co-flow jets has been varied as well to favor the temperature of fuel reformation and flameless oxidation. These parameters have been controlled to lead combustion or oxidation reaction taking over the entire mixing volume and avoid the visible thin flame front.

1.5 Methodology

Digital photographs and excited-state CH radical (CH*) chemiluminescence (Schefer, 1997) have been used for imaging the flames. The CH* images are post-processed and converted into a 2-D contour profile with spatial axis to describe the flame. The flame structures in these contour profiles are compared with a two-dimensional temperature profile from thermocouple measurement. With proper control of input conditions, the detailed characteristics of the flames are identified. The flame structure and temperature relations between flameless oxidation and fuel reformation has been analyzed.

1.6 Thesis Organization

This thesis is focused on the experimental analysis of an initially non-premixed inversed diffusion flame. The experimental burner assembly, gas delivery method, burner configuration, CH* chemiluminescence imaging system, temperature controlling/monitoring system and flame stability measurement system are described in Chapter 2. The preliminary results on the flame structure characteristics are discussed in Chapter 3. It includes IDFs with various flow arrangement and different co-flow conditions, and results are obtained by using unfiltered pictures and temperature measurements. The flames with different inlet conditions and co-flow gases are presented in Chapter 4. The comparison of flame structures from CH* chemiluminescence

distribution with temperature profile for various pre-heating level and different co-flow gases are included in this chapter. Detailed analysis for the characteristics of the flames follows, with discussions on the impact of different inlet conditions on inversed diffusion flames. The evidence of flameless oxidation and fuel reformation has also been described in this chapter. The conclusions and possible future work are presented in the final chapter.

CHAPTER 2

Experimental Apparatus

The design and fabrication of the initially non-premixed inversed diffusion flame burner experimental setup was carried out as a PhD dissertation project (Johnson, 2009). The detailed description of major experimental setup components are provided in his dissertation. When the experimental setup was adopted for this work, the main parts were in working condition, but additional connections and modifications were needed to put the system together in order to get it ready. The major additions and modifications done to the experimental setup during this research work include the following:

- Modification of the gas delivery system by introducing the simulated combustion products, nitrogen and additional compressed shop air into the system.
- The heat exchanger and its controlling system have been introduced in order to obtain different pre-heating temperature levels of the co-flowing gases.
- Modification of the temperature controlling program to measure and monitor the flame and burner temperature.
- Integration of imaging processing program for online processing of measurement to more accurately evaluate with the flame lifting heights, and quantify the flame oscillation of the unstable flames.

Since Johnson (2009) has described most of the key components, only an overview of the experimental apparatus and modifications that have been done during the course of research are discussed in this section. The detailed temperature measurement system with the control units is also covered in this section, additionally the CH* chemiluminescence system and post-processing code are discussed with proper literature support. Furthermore, some thermocouples have been replaced or reinstalled, and additional thermocouples have been added to the temperature measurement system. A newly designed imaging processing system by utilizing a webcam has been installed to monitor the flame oscillation.

2.1 Overview of the Experimental Setup

The experimental setup which consists of an inversed diffusion flame burner with two co-axial tubes in the center is shown in the Figure 2.1, the burner is covered by a transparent housing. One of the thermal control boxes, main parts of the traverse mechanism, and the USB portable data acquisition box are also shown in this figure.

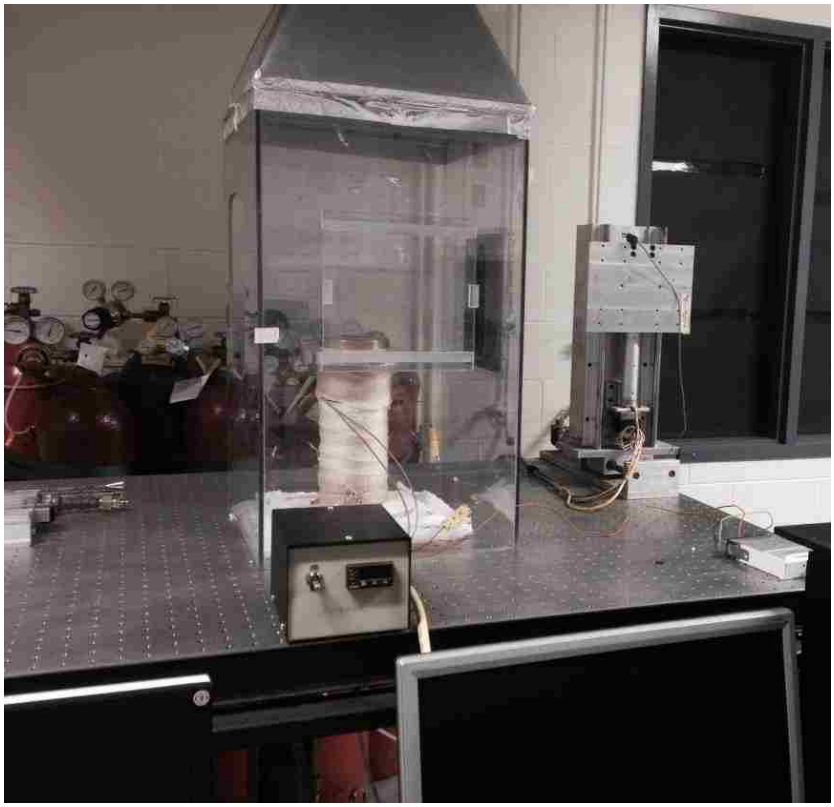

[redacted]

2.2 Gas Delivery System

Figure 2.2 shows the schematic of the gas delivery system for the IDF burner. All the gases are supplied from compressed gas bottles except one from a shop quality compressed air. The gases coming out from gas bottles are first controlled by regulators, after three-way valves (McMaster-Carr 4149T72) and shutoff valves (McMaster-Carr 4886K56 and Swagelok SS-44S6) on each line, the gas lines have the second metering devices which are rotameters (Omega FL-1466-S for central

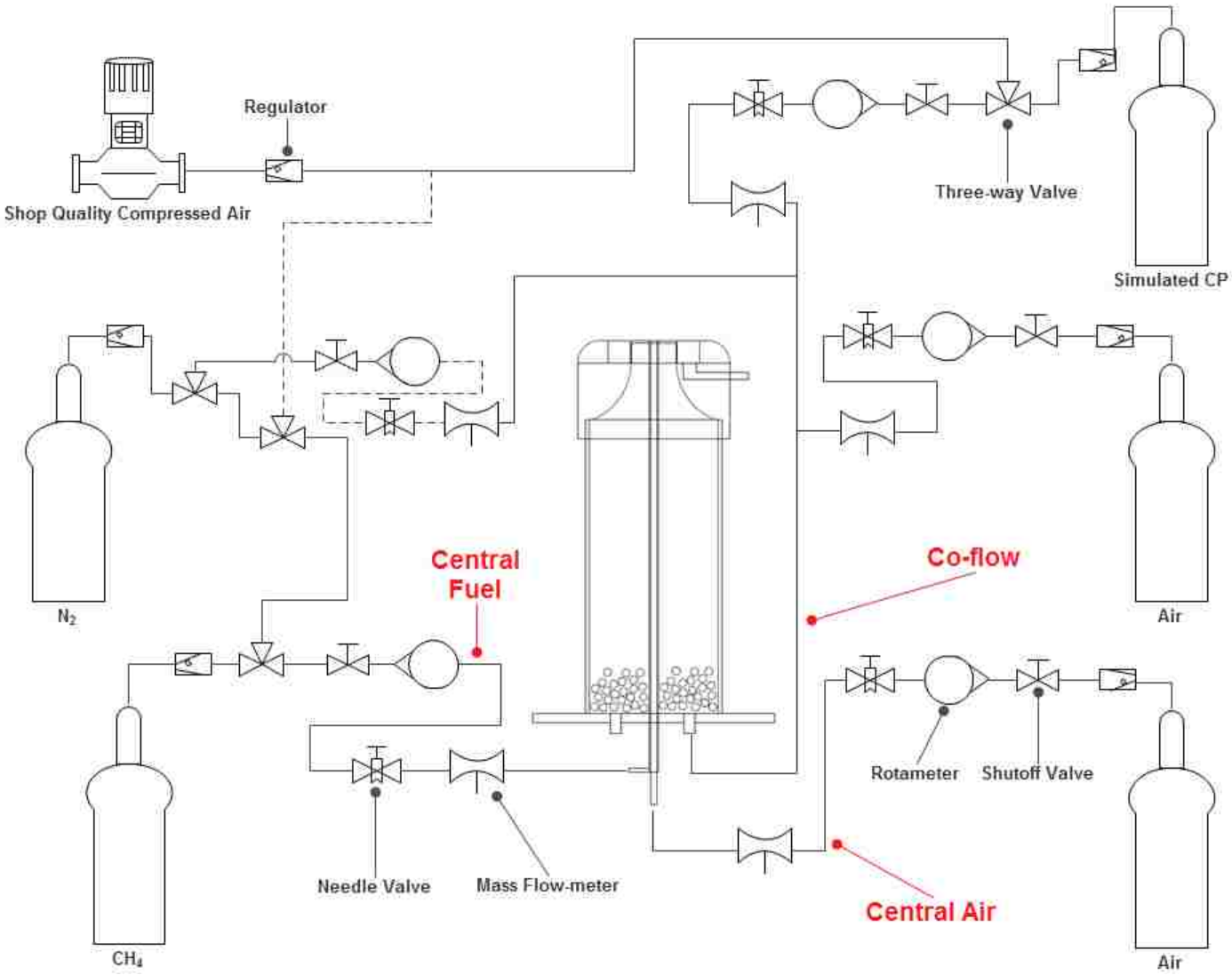
Regulator
Shop Quality Compressed Air
Three-way Valve
Simulated CP
N_2
Central Fuel
Co-flow
Air
Rotameter
Shutoff Valve
Needle Valve
Mass Flow-meter
Central Air
CH_4
Air

[redacted]

fuel, FL1448-G for central air, FL-1445-G for co-flow simulated combustion products, FL1447-S for co-flow nitrogen, and FL-1446-S for co-flow air). Due to the need of precision control for each flow stream, the needle valves (Swagelok B-SS2-D for co-flow combustion products and co-flow air, B-4MG for central fuel/air and co-flow nitrogen) are installed right after the rotameters. The measurements are don with electronic mass flow-meters (Alicat Scientific M-2SLPM-D/5M for central fuel, co-flow nitrogen and co-flow simulated combustion products, M-10SLPM-D/5M for central air and M-20SLPM-D/5M for co-flow air). All the flow measurements have been recorded in this course of work were taken with flow-rate fluctuation $\pm 0.05\ LPM$ during steady state operation. All the flow velocities are calculated based on the bulk velocities at the exit of burner top, and at room temperature and pressure.

2.3 Burner Configuration

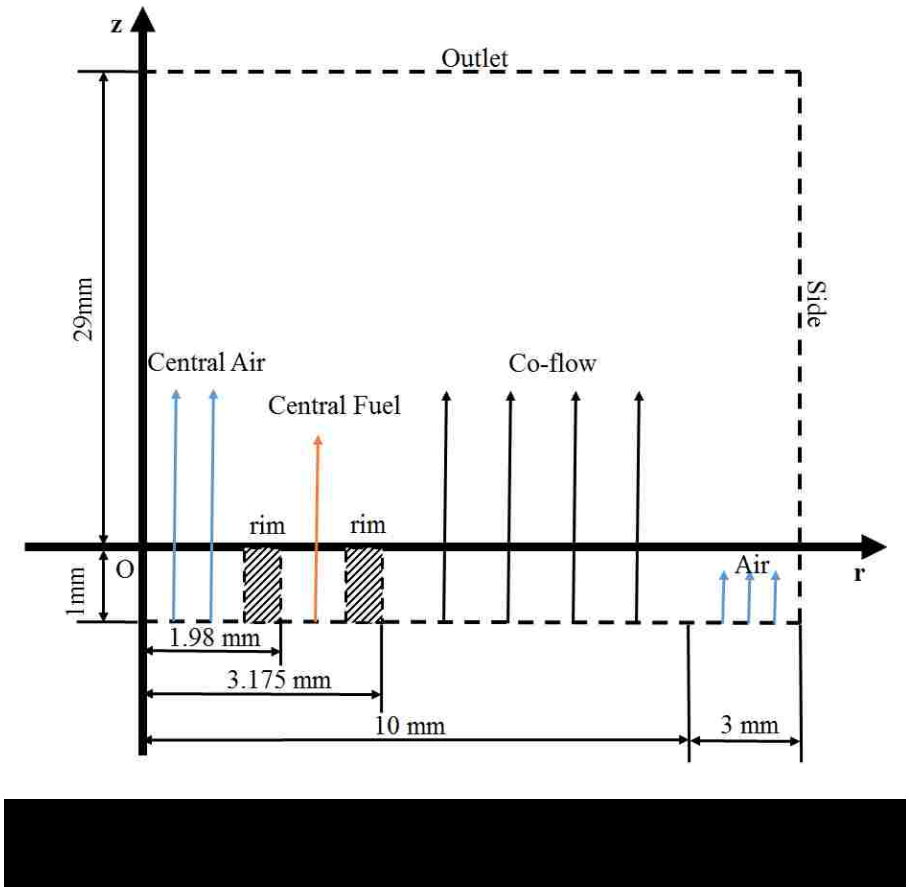

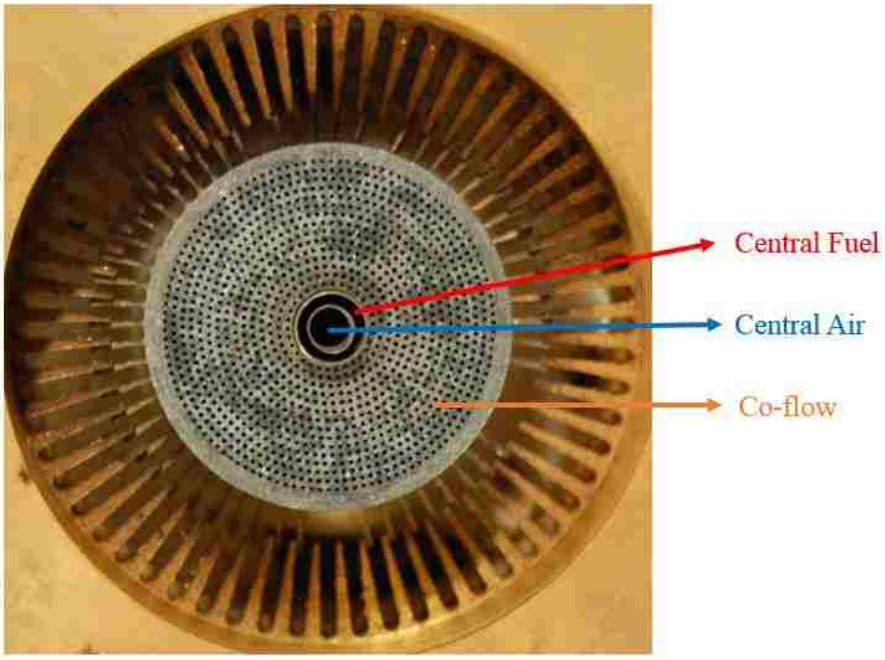
Central Fuel
Central Air
Co-flow

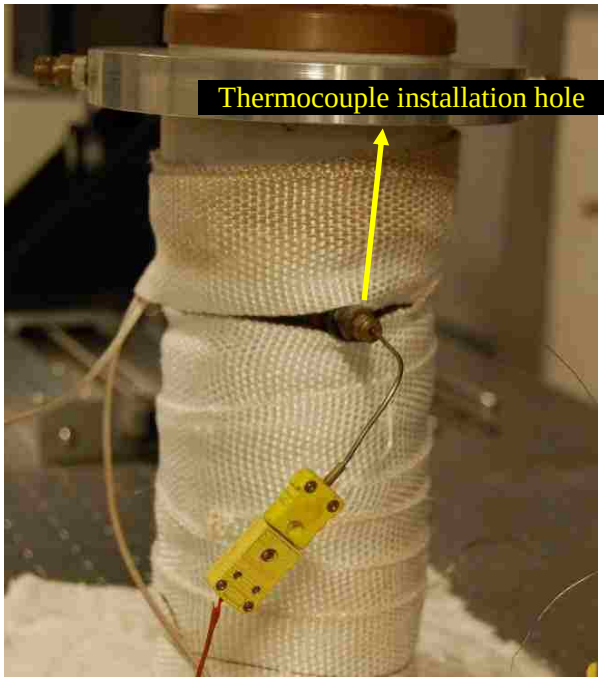
Thermocouple installation hole

Figure 2.3 shows the actual look of the burner face from the top, as is indicated in Figure 2.4, at the center, there is central air flow, and annular fuel flow is called in Figure 2.4 the central fuel flow. Both of the jets are surrounded by the co-flow as it shows in Figure 2.3, the entire co-flow is running through 1114 holes with size of 0.5mm. A port has been drilled for thermocouple installation, so the temperature inside the burner can be measured. It is shown in Figure 2.5.

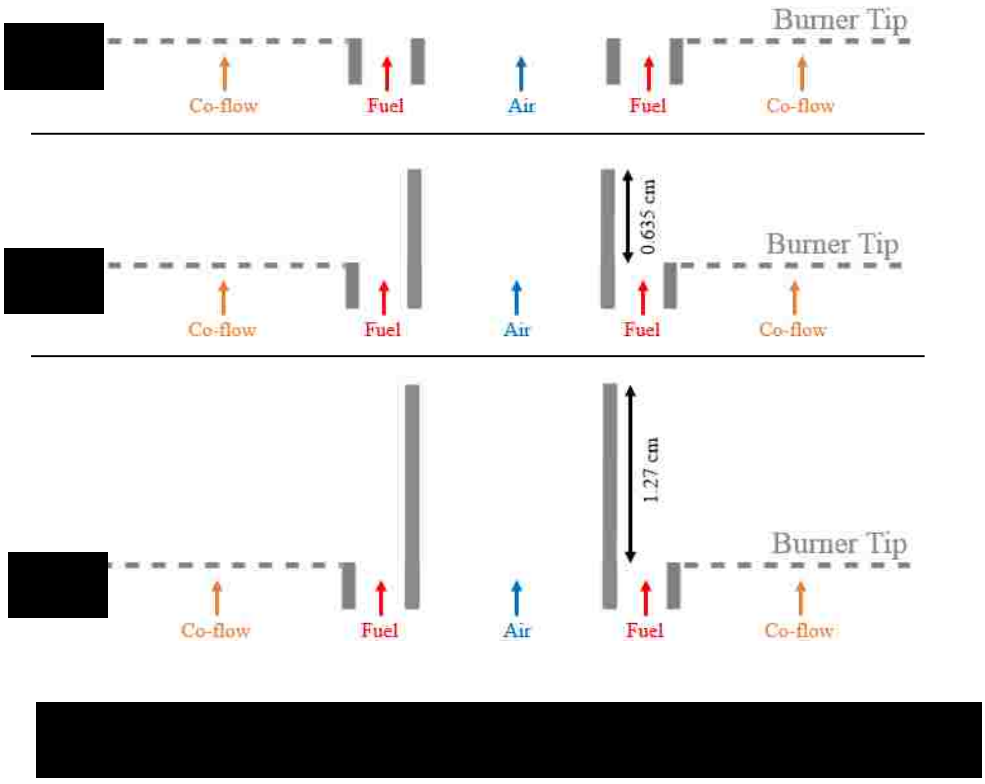

Figure 2.6 shows three central air tube cases that were studied: (1) the tube is flush with the burner surface; (2) raised above the burner surface at 0.635 cm; and (3) raised at 1.27 cm. That is one way to delay the mixing of central fuel/co-flow combustion products with central air flow. It has been investigated in dissertation by (Johnson, 2009) and continued here.

Also in course of this research, the idea for delaying mixing has been taken further. The angled delivery of central fuel has been introduced with inverted cones to guide the fuel flow. Grandmaison et al. (1998) studied the burners with the fuel and air ports axis were all divergent shows in Figure 2.7. The stream 1 has much smaller momentum flux than stream 2, the typical momentum flux ratio ψ_{12} for practical burner operation is 0.02. The angle between the axes is at $\theta_{1,o}$, in this

case $\theta_{1,o}$ equals the port-separation angle θ_{12}, and the range of port-separation angles is from $0 - 40°$. The results indicated that the normalized longitudinal position of the point of confluence has direct relation of the momentum flux ratio, and the port separation angle. d_{12} is generally the distance between the centers of fuel and air ports at exit. With the range of $\psi_{12} = 0.005 - 0.08$, and $\theta_{12} = 10 - 40°$, position at the confluence point of the fuel and air jets x_c is well fitted by the relation:

$$x_c = 6.5\mathrm{d}_{12}\psi_{12}^{0.1}\exp(0.0125\theta_{12}^{2}\psi_{12}^{0.5}) \quad (2.1)$$

In the two-jet mixing zone, Grandmaison et al. (1998) also pointed out while the fuel and air materials mix with each other, the two jets are mixing with more of the ambient combustion gases as well.

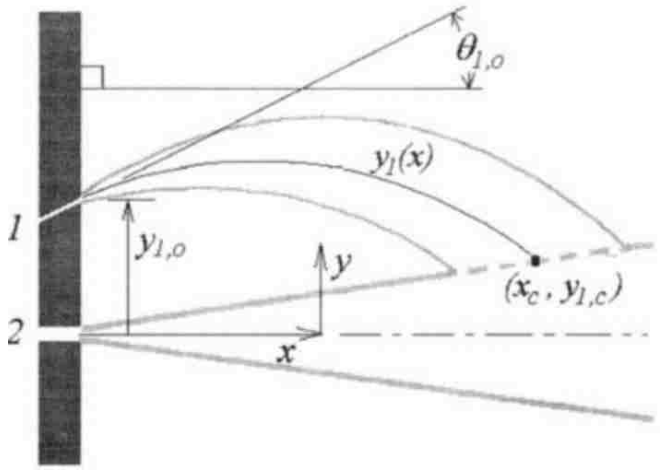

[redacted]

Based on the results illustrated from Grandmaison et al. (1998), the angled delivery methods has been applied with the same purpose to delay the mixing of fuel and air jets even more. As the angle between axes is in the range of $0 - 40°$, $15°$ has been selected as the angle to guide the fuel jet to mix with air jet. To compare with the case that central air tube raised from the burner face, the height of inverted cones are made the same as the level of the air tube raised. Figure 2.8 and Figure 2.9 show the draft and dimension of cones designed, the fuel flow is guided to flow over the surface

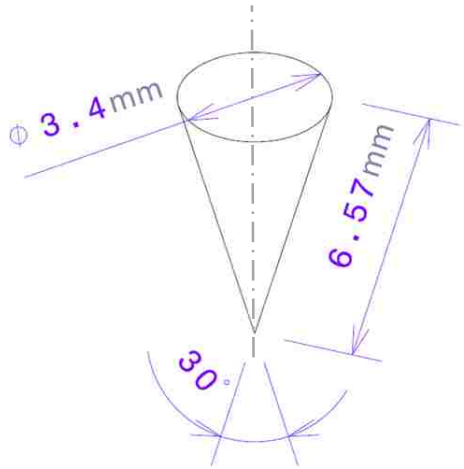

[redacted]

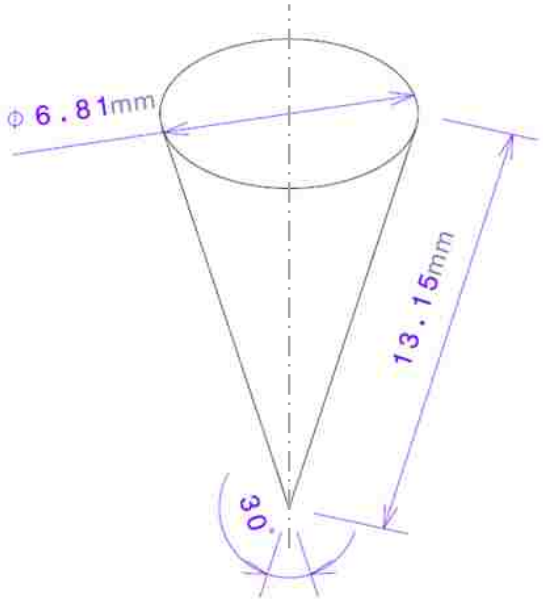

[redacted]

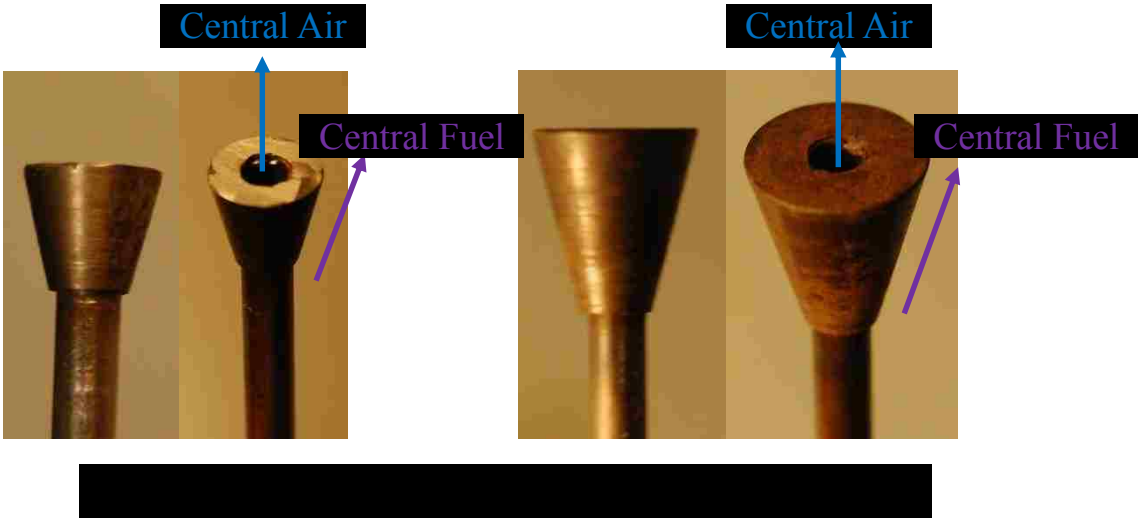

of the cone, and air flow is running through the center of the cone. Figure 2.10 illustrates the flow directions for central air and fuel flowing along the cone.

For experiments with co-flowing combustion products, these were generated from burning a lean methane-air mixture at equivalence ratio $\phi = 0.78$ with velocity of 16.27 cm/s. The co-flowing air velocities in this course of study are the range from 0 to over 61.71 cm/s, and co-flowing simulated combustion products velocities from 0 to 49.37 cm/s. The major geometric and flow configurations have been listed in Table 2.1.

2.4 Chemiluminescence Imaging System

In the PhD dissertation work (Johnson, 2009), excited-state CH radical (denoted CH*) was used as the measurement reference for flame-front location, because Crosley (1989) indicated that light emission from CH has been used to mark the reaction zones as it exists near the flame front which can reveal the location of the combustion chemistry taking place, and in this course of continuing work, same technique has been applied. Pimentel et al. (1960) identified the emitter $CH(\mathrm{A}^2\Delta)$, further denoted as CH*, but the elementary reactions of its formation remained unclear at that time. Williams and Smith (1970) found the oxidation of acetylene in flames is accompanied with strong radiation from ions, and this chemiluminescent radiation predominant in the main reaction zone. OH*, CH*, C_2*and CO are the major chemiluminescent emission radicals. They also stated that

[redacted]

Arrangment	Central Air Flow	Annular Fuel Flow	Co-flow of N_2	Co-flow of Air	Co-flow of CP	Co-flow of SCP
Delivering tube flushed	✓	✓	✓	✓	✓	✓
Delivering tube raised	✓					
Velocity varied	From 0 to 990 cm/s	From 0 to 18.4 cm/s	From 0 to 0.987 cm/s	From 0 to 185 cm/s	Air: From 0 to 2.163 cm/s Fuel: From 0 to 0.25 cm/s	From 0 to 3.4 cm/s
Volumatric flow rate varied	From 0 to 7.316 LPM	From 0 to 0.214 LPM	From 0 to 0.4 LPM	From 0 to 74.944 LPM	Air: From 0 to 0.876 LPM Fuel: From 0 to 0.101LPM	From 0 to 1.377 LPM
Cone		✓				
Temperature varied	From ambient temperature 25 °C to 200 °C	From ambient temperature 25 °C to 200 °C		✓		✓

CH* is formed by the following chemiluminescent reactions:

$$C_2H + O_2 \rightarrow CH^* + CO_2 \tag{2.2}$$

$$C_2H + O \rightarrow CH^* + CO \tag{2.3}$$

$$C_2 + OH \rightarrow CH^* + CO \tag{2.4}$$

Devriendt et al. (1996) indicated that the emitter CH* has intense blue emission at $\lambda \sim 430\ nm$, and it is the most notable features of hydrocarbon flames. Higgins et al. (2001) intend to use the non-intrusive measurement of CH chemiluminescence to provide feedback control of premixed gas turbine engines. The CH chemiluminescence was measured by a photo-multiplier tube (PMT) with a band-pass interference filter (centered at 431.5 nm with a full width at half height of 11.2 nm). Kojima et al. (2000) used chemiluminescence two-dimensional imaging for laminar methane/air premixed flames to overcome the problem of spatial resolution to detect the local flame front, as at that time most chemiluminescence measurements were collecting the global emission along the line of sights of typical optical lens. Kojima et al. (2005) continued their work by comparing the results of spatial intensity profiles of OH*, CH* and C_2 (d) chemiluminescence between spatial resolved measurements and a1-D flame simulation including the excited-state species. The C_2 (d) intensity profile has been found located at the middle of the OH*, CH* species in the reaction zone, and the sequence of the location of the peak intensity was OH*, flowed by C_2 (d) and then it is CH*. The Abel inverted technique has been used by Jeong et al. (2006) to produce the concise and exact solution for reconstruction of the CH* images. The CH* profile is extracted from intensity profile data by yielding two dimensional 'slices' of the flame.

The CH* chemiluminescence imaging system used here was described in the PhD work (Johnson, 2009), and it is used mostly unchanged in the current work. The post process program is based on the three-point Abel transform which is also been described in Johnson (2009). The details of modification of the image processing methodology can be found in Appendix A.

2.5 Temperature Controlling System

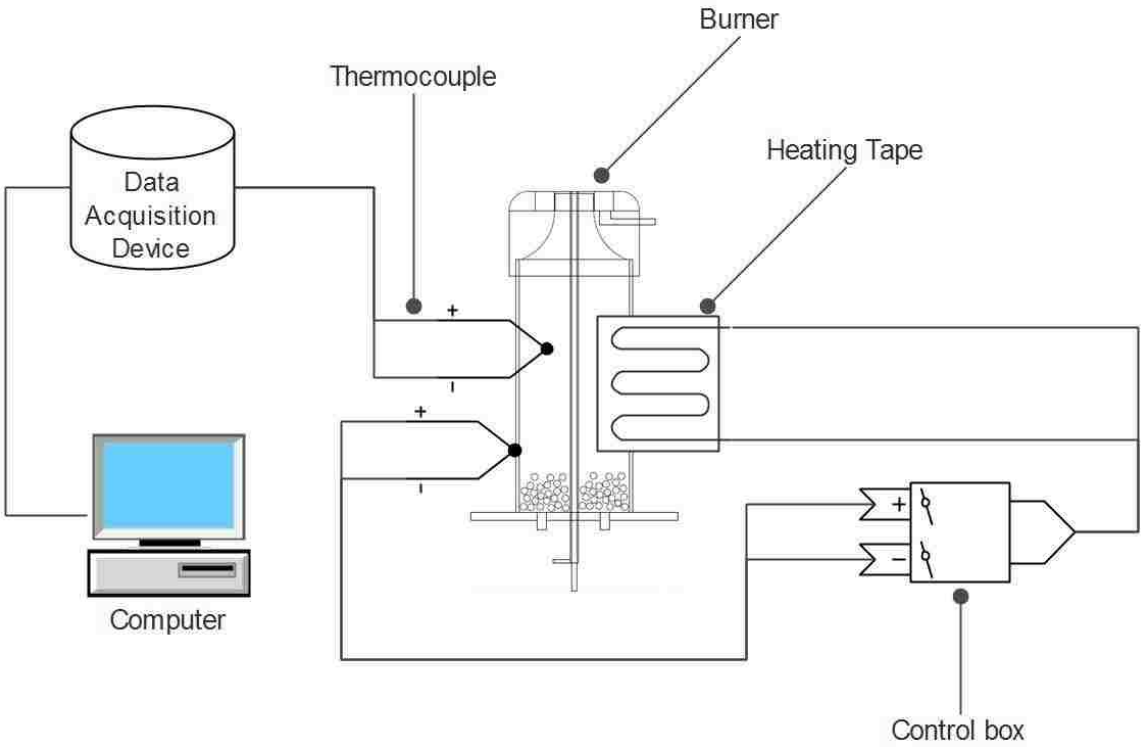

The overview schematic of the temperature controlling system shows in Figure 2.11. Since pre-heating the co-flow gases is essential factor to achieve the flameless oxidation and fuel reformation, to maintain the operating conditions of the IDF burner at a certain temperature range is crucial, and the temperature controlling system is severing this purpose. This system consists of two parts, the temperature monitoring and close loop temperature controlling. To monitor the temperature, K-type thermocouple (Omega KMQXL-125G-6) has been installed through the hole drilled on the burner wall which is shown in Figure 2.5. Break-up Board (NI SCB-68) and data acquisition card (NI PCI-MIO-16E-1) are collecting the temperature data from thermocouple and sending to the LabVIEW program in the computer, so the real time temperature reading are presented in the computer. The monitoring LabVIEW program is showing in Appendix B with details. On the

temperature controlling side, the close loop control is taking by the on and off controller showing in Figure 2.12. The thermocouple (Omega CHAL-005) signal is send to the controller, it processes the temperature reading in order to command the power switch of the heating tape (McMaster-Carr 4550T253). The temperature is maintained by an on and off switch of the heating tape, and the switch is controlled by the feedback from the thermocouple.

[redacted]

2.6 Temperature Measurement System

Figure 2.13 and Figure 2.14 are showing the traverse mechanism and control box which are the two major parts of the temperature measurement system. The traverse mechanism is built based on two actuators to support the motion in vertical and horizontal directions, as it connects to the thermocouple fork which supports the R type thermocouple (Omega SP13RH-003/SPPL-003). The traverse mechanism is controlled and powered from one of the modules inside the control box. The motion control module contains screw terminal (NI UMI-7764) and motion control card (NI PCI-7330) which is connected to the computer and operate through the LabVIEW program. The program is running based on target positions, and it has the minimum step of 0.01 mm for both horizontal and vertical directions. The other module inside the control box is used for the temperature measurements, the R type thermocouple readings are collected through data

acquisition card for temperature monitoring mentioned in section 2.5. The LabVIEW program of the temperature measurement is also shared with the temperature monitoring program.

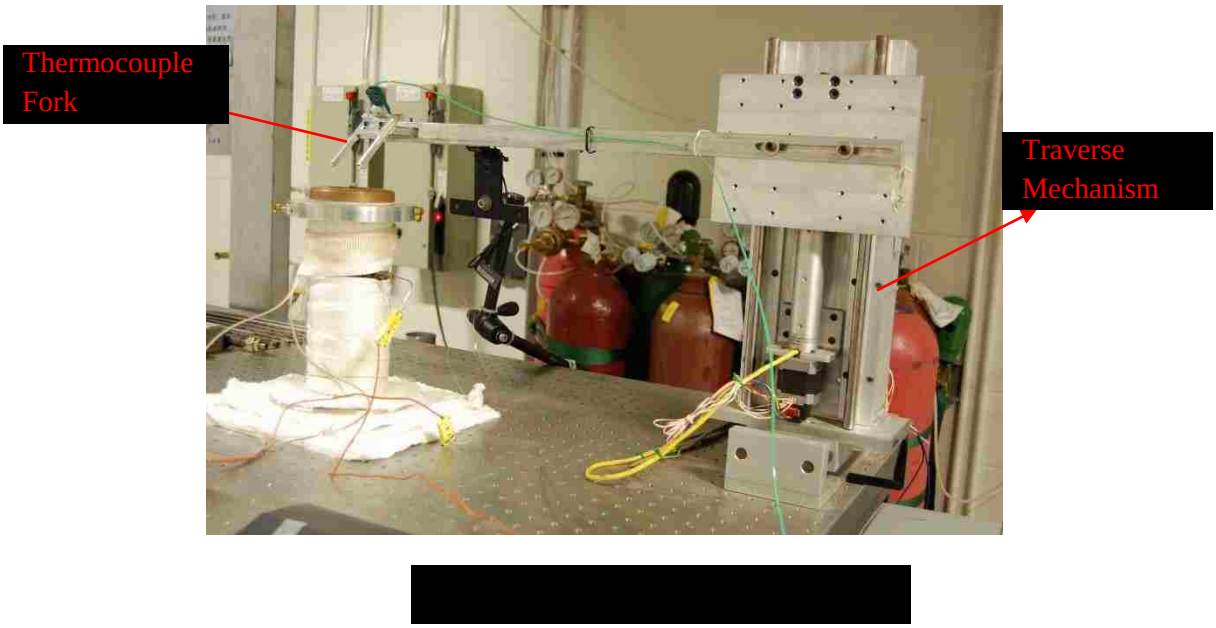

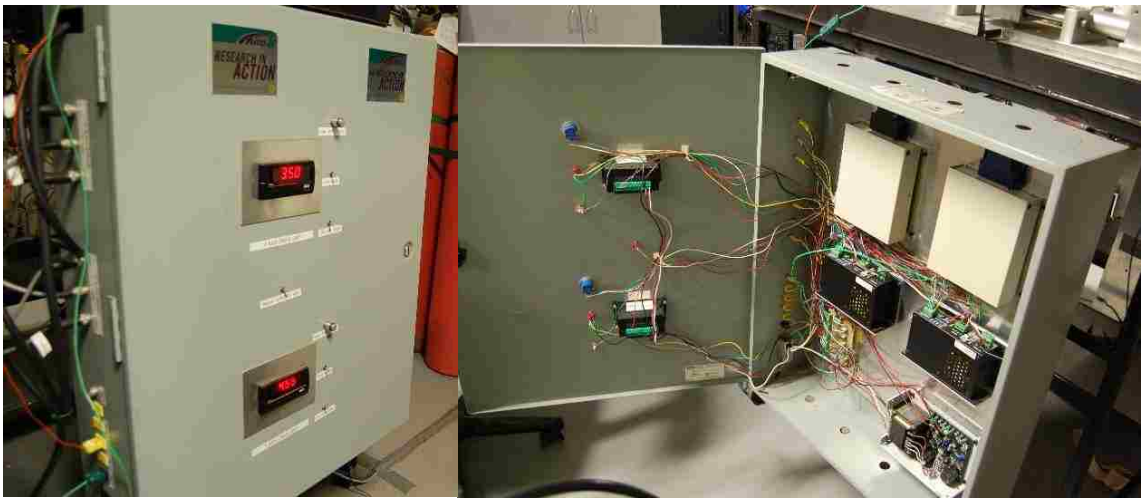

2.7 Flame Stability Measurement System

During this course of work, some flames were found to be highly unstable when the inversed diffusion flame is running with co-flow simulated combustion products, since the simulated combustion products contains only very small amount of oxygen. The composition of simulated combustion products are calculated based on the combustion products methane and air flame with equivalence ratio $\varphi = 0.78$,

$$CH_4 + 2.56(O_2 + 3.76N_2) \rightarrow CO_2 + 2H_2O + 9.64N_2 + 0.56O_2$$

Since the water in the real products is gaseous, in the simulated (bottled) combustion products, it was omitted. The final composition of simulated combustion products is 7.62% of carbon dioxide, 4.26% of oxygen, and 88.12% of nitrogen by volume.

As the flames are unstable with simulated combustion products, the flame characteristics vary all the time. To measure the flame lifting height, as the flame is moving up and down, capturing the lift-off height accurately is quite problematic. The flame stability measurement system has been introduced to overcome this issue. Huang et al. (1999) studied the on-line flicker measurement of gaseous flames by imaging processing. A CCD camera has been used, on-line imaging processing and subsequent was used to provide the control. They concluded that their system has the ability to monitoring the flicker and analyzing the dynamic nature of a flame, and the relative error of their measurements was no greater than 3%. In course of this work, the system is much simplified version, and it includes just contains a webcam (Microsoft LifeCam HD-3000) and a computer to run the MATLAB program. The webcam has the framing rate of 30 frames per second. The MATLAB imaging processing toolbox has been used for capture and process the images. Imaging geometric transformation and image conversion are the two major functions been selected for this program. The percentage of flame getting below certain height in 100 frames is calculated by the program. Total number of pixels the flame has taken are also been counted. The flame motion is

captured over 5 seconds, and the calculation results are taken into account to establish the lift-off height. The program details are described in Appendix C.

CHAPTER 3

Flame Characteristics with Co-flow of Combustion Products from a Flat Flame

This chapter discusses results of the experiments conducted on IDF flames with co-flow combustion products from a premixed flat flame shown in Figure 3.1. It is the continuation work of the PhD dissertation (Johnson, 2009), and it is focused on finding the evidence of flameless oxidation and fuel reformation at the initial state of this course work. Minor changes have been made to the experimental setup at this stage, the operation conditions and the gas delivery method has been modified to favor the targeted working conditions.

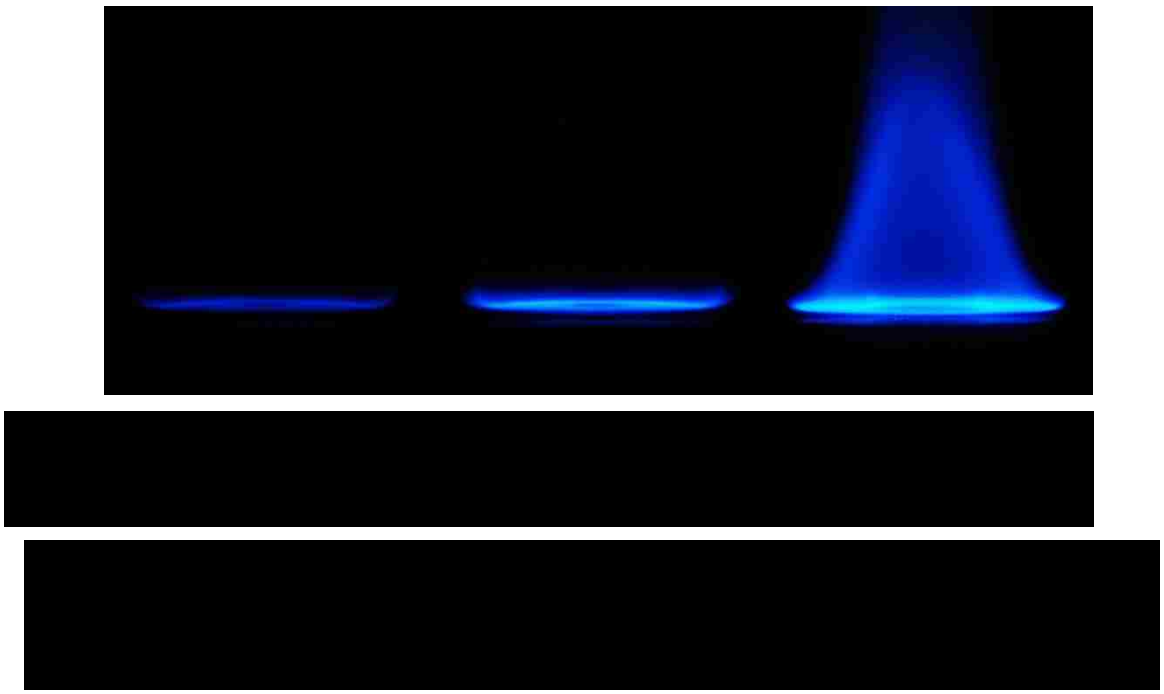

In Figure 3.1, from left to right are the burner-stabilized flames with increasing of equivalence ratio by decreasing the co-flow air velocity, so that the flame is getting richer.Various flow rate of co-flow air or fuel result in the premixed flame with different equivalence ratios. As the flat flame is serving as the source of combustion products, it results different composition of the combustion products. With different combination of central air and fuel velocities, the flame structure changes has been illustrated in Figure 3.2. A fuel rich premixed flame has been created with the fixed flow rate of uco-flow air = 0.65 cm/s and uco-flow fuel = 0.19 cm/s. By increasing the central air

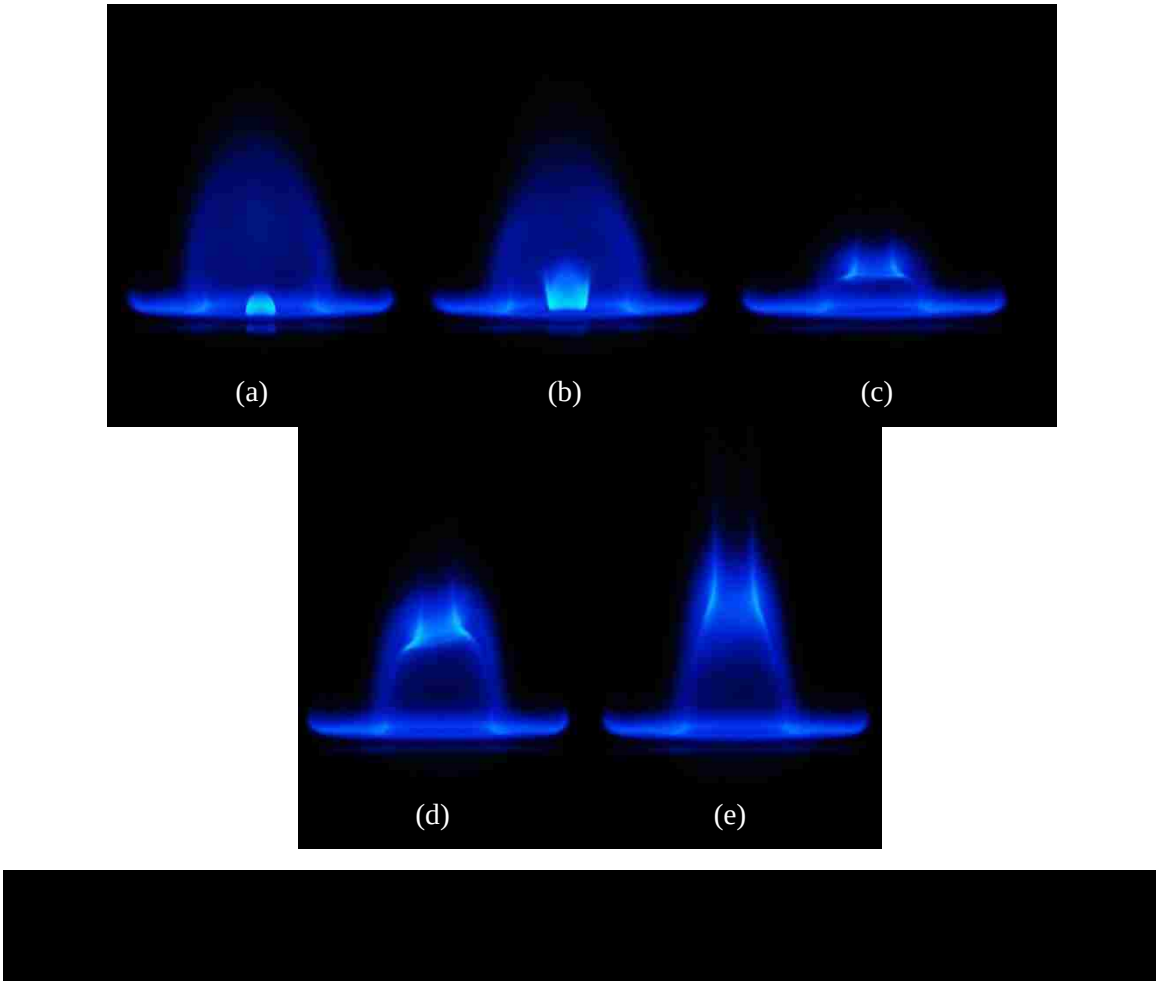

Table 3.1: Central air and fuel running conditions for Figure 3.2

Operating Conditions

Picture #	$u_{central\ fuel}$ (cm/s)	$u_{central\ air}$ (cm/s)
a	0.861	4.06
b	2.584	4.06
c	2.584	13.533
d	5.167	4.06
e	2.584	31.125

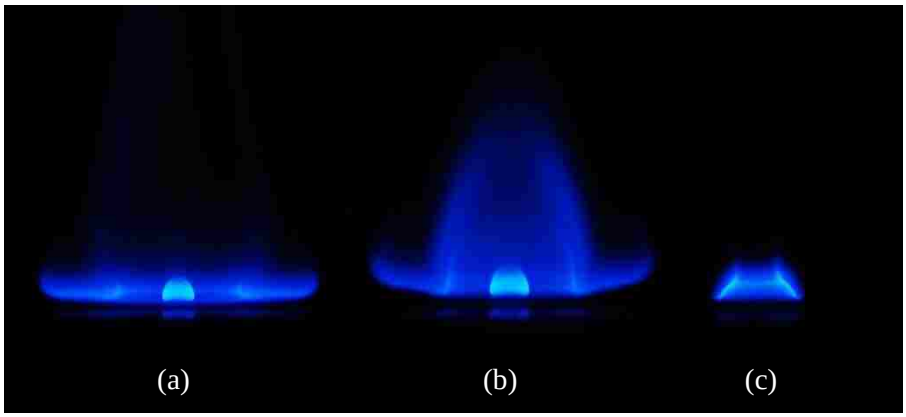

Table 3.2: Central air, fuel and curtain gas running conditions for Figure 3.3

Operating Conditions			
Picture #	$u_{central\ fuel}$ (cm/s)	$u_{central\ air}$ (cm/s)	$u_{certain\ gas}$ (cm/s)
a	0.75	4.06	0
b	2.584	4.06	1.06
c	2.584	13.533	5.3

velocity, inner flame of IDF grows longer and at same threshold velocity it gets detached from the burner top. With move velocity increase, the inner flame height keeps on increasing till it merges with the outer diffusion flame. On the other hand, if the annular fuel flow velocity is increased, the major outer diffusion flame changes is its elongation.

Figure 3.3 shows flames for a fixed flat flame in the first two pictures with different central air and fuel velocities. A curtain gas of nitrogen has also been introduced into the flow for the conditions shown Figure 3.3. The another stream of co-flowing gas surrounding the existed flow field acts like a 'shield' or 'curtain' to prevent the surrounding air entrainment to this flow field. When increasing the flow rate of the outside nitrogen, the first two pictures on the left clearly show that the edge of the flat flame has been curved up. Comparing with Figure 3.2, by adding the curtain gas, the flame structure does not change much except for the flat flame edge. The double flame structure is not sensitive to the surrounding entrainment of the surroundings. To take a look of the effect of the curtain gas on the IDF, the flat flame has been turned off in the third picture. High flow rate of nitrogen curtain does not lift the inner IDF. All these conditions are with relatively small central air and central fuel flow rates, and it indicates that with these operation conditions, the flame structure is relatively stable. Among conditions shown in Figure 3.2 and Figure 3.3, there is no clear evidence for fuel reformation and flameless oxidation. One way to possibly change this is to delay the mixing of central air and central fuel.

A sequence of pictures is shown in Figure 3.4, where the central air tube has been raised for 0.635 cm in order to delay the mixing, and the flat flame is for the co-flow mixture of air and fuel are fixed at lower equivalence ratio. Since the stainless steel tube is exposed to the flat flame, the high temperature from the flame is heating up the tip of the tube, so as the second picture of this sequence shows. Without any cooling of the tube and the central fuel is flowing, the pyrolysis process starts around the hot spot of the tube. That is the major reason for the red color from the fuel stream, as the fuel undergoes a thermochemical decomposition into species like hydrogen and carbon monoxide with some soot particles are also formed there to emit the red color light. When central

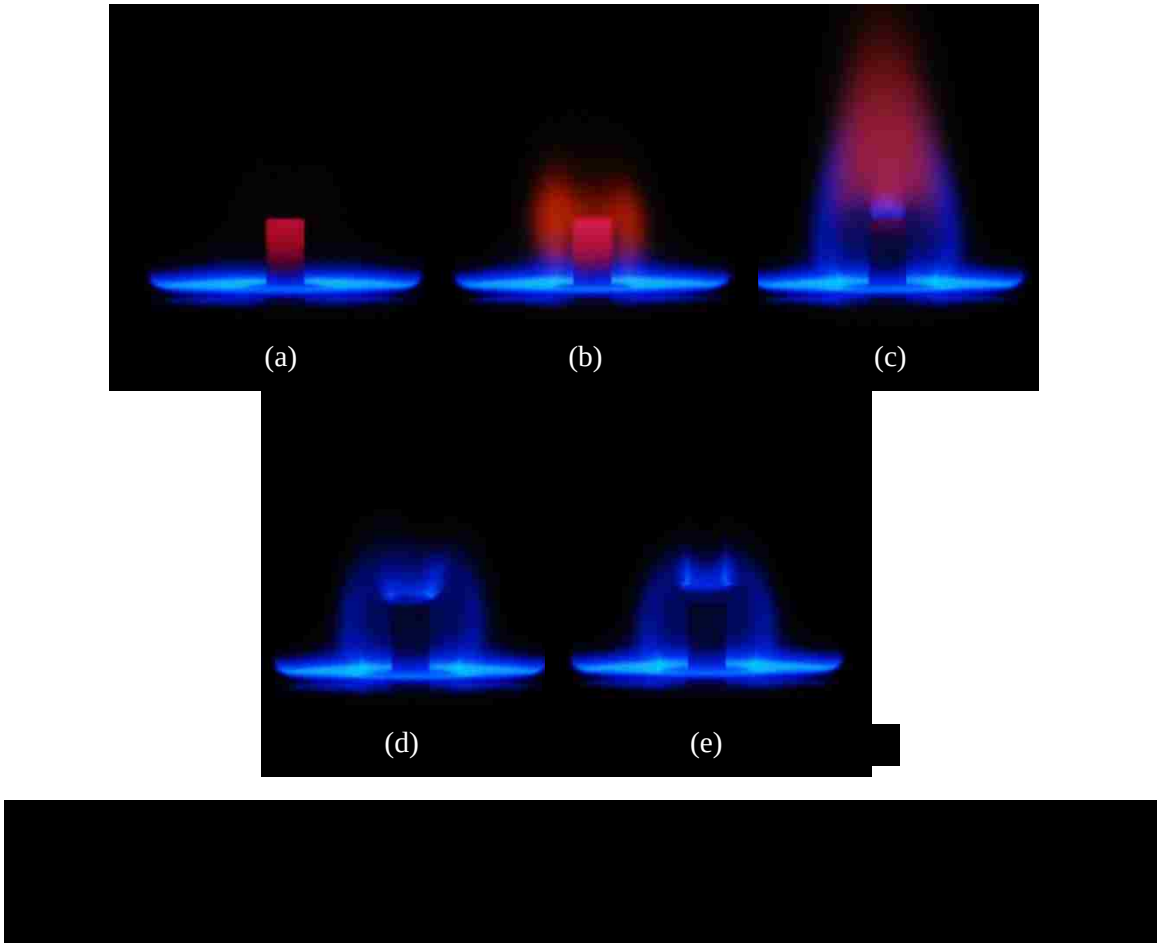

Table 3.3: Central air and fuel running conditions for Figure 3.4

Operation Conditions

Picture #	$u_{central\ fuel}$ (cm/s)	$u_{central\ air}$ (cm/s)
a	0	4.06
b	2.584	0
c	2.584	1.353
d	2.584	5.413
e	2.584	5.819

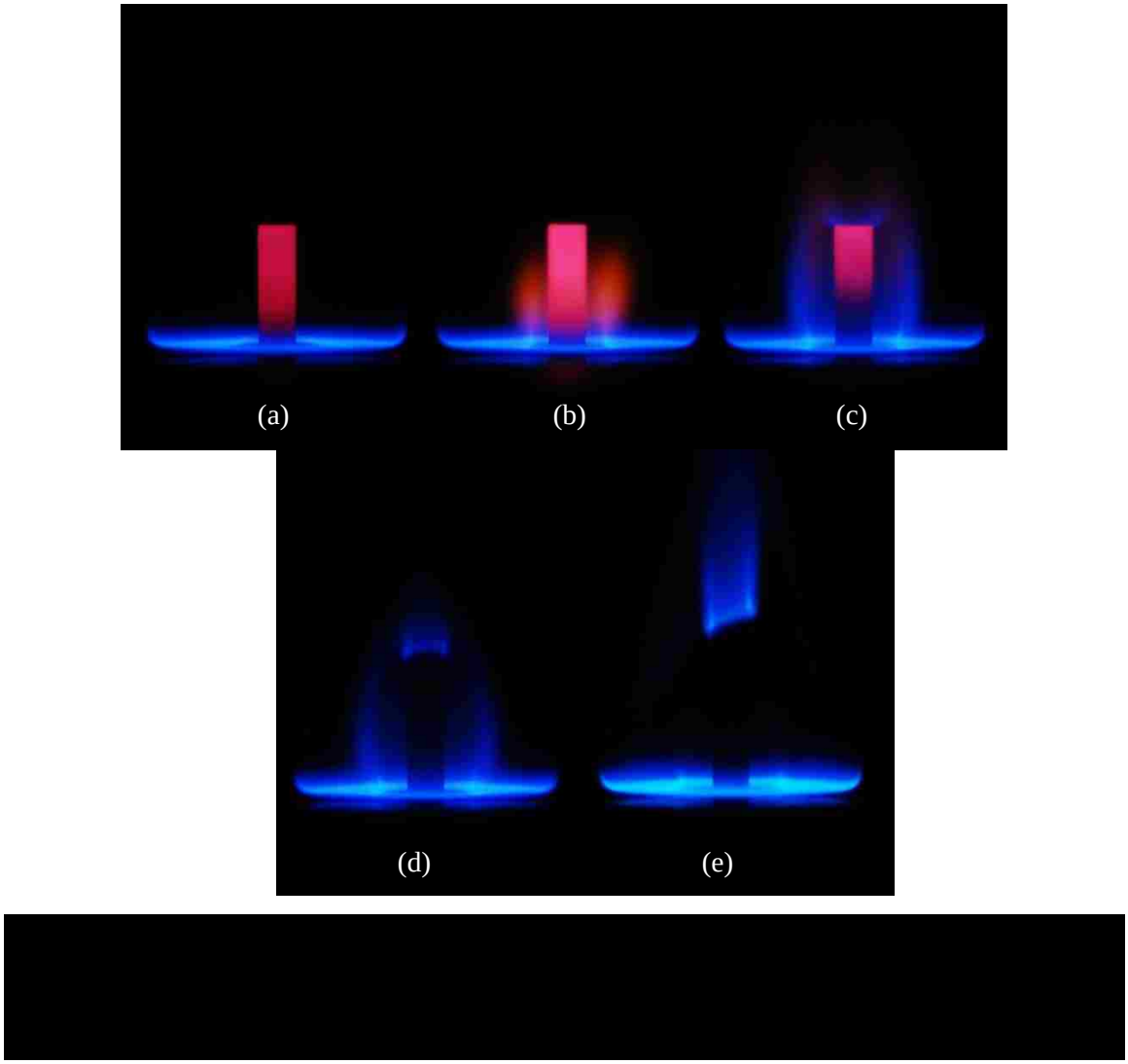

Table 3.4: Central air and fuel running conditions for Figure 3.5

Operation Conditions

Picture #	$u_{central\ fuel}$ (cm/s)	$u_{central\ air}$ (cm/s)
a	0	4.06
b	2.584	0
c	2.584	1.353
d	2.584	5.413
e	2.584	5.819

air being introduced to the flow field as shown in the third picture, the air flow also acting as a coolant of the tube. As the temperature of the tube decreases, the fuel pyrolysis is occurring at higher flame elevation, and the outer diffusion flame gets formed, with the inner flame attached to the tip of the tube. By increasing the flow rate of the central air even more, the cooling effect of the tube becomes stronger, and all the hot spots on the tube are eliminated, the fuel pyrolysis is terminated as well. As the central air tube raises closer to the tip of the outer flame, the inner flame start to merge with the outer flame with relatively lower central air flow rate. By increasing the central air velocity even more, the flame structure stays similar to the previous case except that the inner flame is lifted a little bit higher than before.

The flame structures at various operation conditions where central air tube is raised to 1.27 cm are shown in the sequence of pictures in Figure 3.5. The delaying time for mixing of the central fuel and central air has almost doubled as the distance for central fuel needs to travel to tip of the air tube. More of high temperature region has been created on the stainless steel tube as it exposed to the flat flame if there is no central air flowing at the center. The gaseous fuel starts to break up almost right after it makes contact with the red hot region of the tube as it is shown in the second picture. The pyrolysis is occurring along the tube tip similarly to the previous case. By introducing a small amount of central air flow to flame (b), the cooling effect decreases the area of hot region, and as the thermochemical break up process is reduced, the outer diffusion flame is formed. The inner diffusion flame is established at the central air exit and immediately connects with outer flame as the tube reaches almost the same elevation of the outer flame height. With increasing the flow rate of central air to flame (d), the hot region on the stainless tube is completely eliminated, also the double flame structure has been formed. The inner flame front was formed around the tube. The upper part of outer flame starts to fade as now the central air stronger momentum jet attracts the weaker fuel momentum jet, so the mixture is burning at the tip of the tube instead of occurring as upper part of outer flame. To explore this phenomenon furthermore, the central air velocity has been increased to even higher level in flame (e). The outer flame has disappeared in this case, and

all the gaseous fuel are entrained to the central air flow field, so only one diffusion or partially-premixed flame is formed at the tip of the tube. In the described above the two tube offset cases, the flame front still has formed indicating that the flameless oxidation did not occur.

The main issue to be considered at this stage is that just increasing the mixing delay is not enough. In the above cases, the mixing region of the co-flow combustion products and central fuel is still limited to the two jets narrow contact area. To improve the mixing conditions, the inverted cone has been introduced which can provide both, extended mixing time, and the enlarged mixing region as well. A sample sequence of flame images with inverted cone installed is shown in Figure 3.6. The cone height has the same height as the raise fuel tube to 1.27cm. When the cone is exposed to the flat flame, there is still a large hot area being created, similarly to the offset tube case. It causes the fuel to pyrolyze almost right at the exit of the fuel nozzle which is shown in the flame (b). When the small amount of central air starts flowing, the thermochemical decomposition effect start to diminish, and outer diffusion flame is formed. Due to the heat accumulated in the cone, still some of the fuel is broken up when flowing over the hot spots, so the soot particles are formed right beside the inner diffusion flame, flame (c). When the central air velocity is increased even more, flame (d) and (c), the two flames are merging together as a 'water drop' shape of flame, and the cooling of central air eliminates the hot spot on the cone. Further increasing of the central air velocity causes the diffusion flame to break apart again, flame (e), due to the strong air jet attraction of the weaker fuel jet to form the inner diffusion flame above the cone. With this geometrical configuration, the flame front still can be clearly observed, so the flameless oxidation mechanism is still not occurring.

To obtain a closer look at the structure of the flames for various operation conditions with co-flowing air and combustion products, the temperature profiles has been produced from thermocouple measurements. The ideal flameless oxidation would have a uniformed temperature distribution inside the reaction zone, as the oxidation reaction happens across the entire volume instead of located only in the narrow flame front area. Figure 3.7 shows the temperature contour

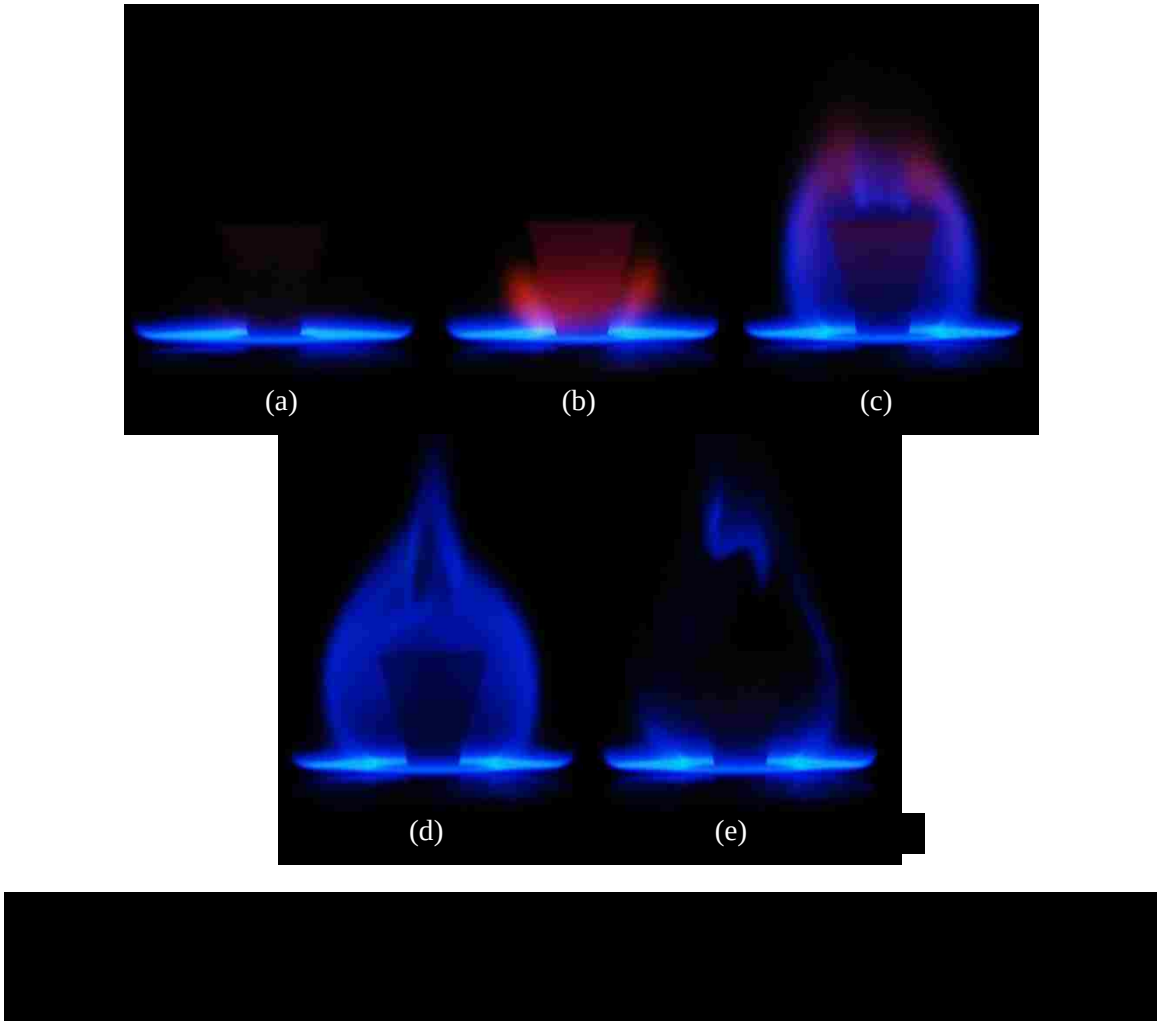

Table 3.5: Central air and fuel running conditions for Figure 3.6

Operation Conditions

Picture #	$u_{central\ fuel}$ (cm/s)	$u_{central\ air}$ (cm/s)
a	0	4.06
b	0.861	12.585
c	4.306	29.772
d	2.584	12.585
e	0.861	12.585

for a half of flame, and it covers 1.5 cm of the total flame height. This temperature contour field is compared with one of the numerical simulation results from Johnson (2009) as the reference. The maximum temperature of both experimental and simulation results are at the same level, around 1900K. As far as the flame location is concerned, the inner flame in the experiment is twice as high as the simulated flame, and the experimental outer diffusion flame is further away from the center axis when comparing to the results from simulation. There is a larger area with temperatures lower than simulation inside the outer diffusion flame. In both cases, the high temperature are clearly depicted to indicate the flame fronts. With co-flow air, the flameless oxidation is unlikely to happen, as combustion occurs in the thin mixing region of the central fuel jet with central air and co-flow air. There is not enough time for fuel and air to mix and form a homogenous mixture.

Figure 3.8 shows temperature fields for two operation conditions with co-flow combustion products from measurements. It compares with and without the inverted cone. The temperature profile is still shows half of the flame starts from the centerline. The figure on the left is the case without the cone. The high temperature region is formed along the mixing region of central air and central fuel, and central fuel and co-flowing combustion products as well. The ultra-high temperature region occurs at the inner flame which is located at 1.5 mm above the burner surface where maximum temperature is around 1800K. In this case, the high temperature region located at 0.2 - 0.8 cm in the horizontal direction. When compared with co-flow air case in Figure 3.7, the high temperature regions are even narrower. With the inverted cone installed, there is no clearly indication that inner flame has formed as there is no high temperature region along the central air and central fuel mixing path. The location of the outer flame has been pushed about 2 mm horizontally, but the combustion still occurs at the mixing region of co-flow combustion products and central fuel. The outer diffusion flame forms at the 0.4 to 1 cm in the horizontal direction. When the central air and central fuel jet mix and start the reaction, the flame merges with outer diffusion flame, and in this case the double flame structure is showing as a single unified

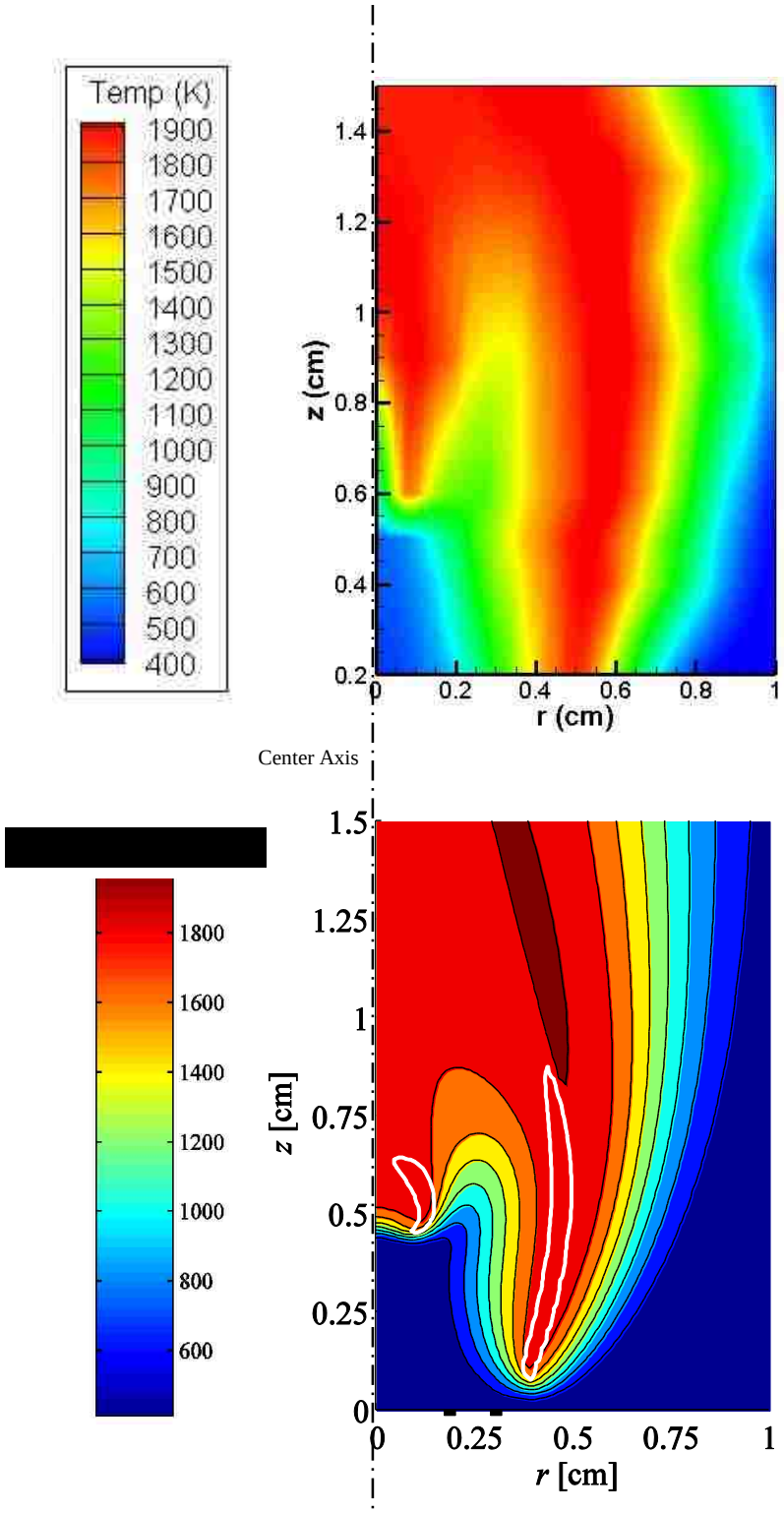
Temp (K)
1900
1800
1700
1600
1500
1400
1300
1200
1100
1000
900
800
700
600
500
400
z (cm)
r (cm)
Center Axis
1800
1600
1400
1200
1000
800
600
z [cm]
r [cm]

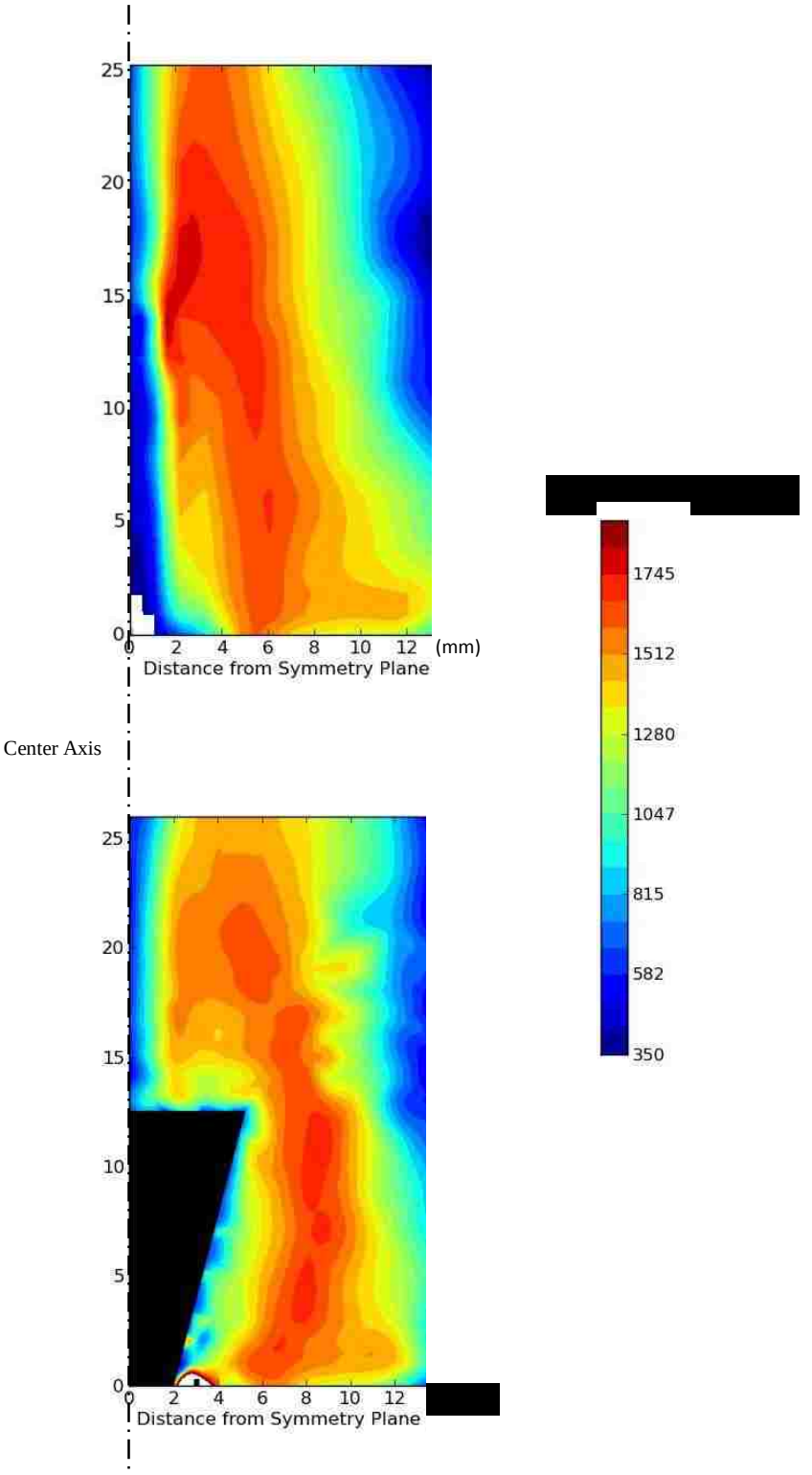
25
20
15
10
5
0
0 2 4 6 8 10 12 (mm)
Distance from Symmetry Plane
Center Axis
25
20
15
10
5
0
0 2 4 6 8 10 12
Distance from Symmetry Plane
1745
1512
1280
1047
815
582
350

[redacted]

flame. The high temperature region is formed extending from the bottom of the cone to more than 1cm above the cone. The maximum temperature is over 1750 K. The temperature region is still narrow, and it coincides with the mixing zone of central air and central fuel, central fuel and co-flowing combustion products. From Figure 3.8, the temperature of combustion products entering the flow field is over 1300K, and flow field mostly covered by high temperature region which is above 1200K.

For all the operation conditions presented and discussed in this chapter, the flameless oxidation is hard to identify based on the flame images and temperature profiles from thermocouple measurements. The area of high temperature are formed as flame fronts and not as uniform distributed reaction zones with much lower temperature. Initial idea for solving this was to delay the mixing time. However with the inverted cone mounted, the thin flame front is still exist in the mixing zone. In conclusion, delaying mixing is not enough to achieve flameless oxidation. The hot combustion products emerging from the lean flat flame have temperature over 1300K which acts as the heat source to increase the temperature of the entire flow field. To explore the fuel reformation aspect of the IDF under these operation conditions, the parallel work (Barks et al., 2013) was set-up with the use of 2-D simulation to find out the evidence of fuel reformation. The major species indicating fuel reformation are hydrogen and carbon monoxide. Results have shown that for the parallel co-flow case, there is a region which CO and H_2 are produced, and in the angled co-flow case, these two species are consumed very fast at higher elevations. The amount of hydrogen and carbon monoxide produced in both cases are still very small amount compare to the other species. These two species produced inside the reaction zone are really hard to differentiate if coming from fuel reformation or the thermochemical decomposition since the amounts are quite small. Because of the high temperature across the flow field, the two species generation is most likely due to the thermal break up instead of fuel reformation since the optimum temperature to obtain partial oxidation reformation is around 1100K, and the temperature profiles are clearly showing temperature much higher in the mixing zone.

As the co-flowing combustion products are the major heat source to warm up the flow field, to overcome the high temperature issue, the temperature of the co-flowing combustion products has to decrease to the level of temperatures that are conducive to the flameless oxidation and fuel reformation. The delay of mixing did not show much of effect as far as flameless oxidation and fuel reformation are concerned.

CHAPTER 4

Flame Characteristics with Pre-heated Co-flow of Simulated Combustion Products

4.1 Flame Structure Based On Digital Imaging

Co-flowing combustion products from the premixed lean flat flame might be too hot for fuel reformation and flameless oxidation to occur. To overcome this issue, the simulated combustion products have been introduced. In this chapter, the experiments on IDFs with co-flowing air, nitrogen and simulated combustion products will be discussed. The primary objectives are to explore the variable flame structures and to find those that can favour fuel reformation and flameless oxidation.

For all experiments, the simulated combustion products have fixed composition, 7.62% of carbon dioxide, 4.26% of oxygen, and 88.12% of nitrogen by volume. The results of experiments will be compared with the operating conditions with co-flowing combustion products from the lean flat flame with the similar composition.

To demonstrate with the impact for feeding simulated combustion products into the co-axial flows, Figure 4.1 shows flames for the fixed central fuel flow rate, and with different selection of co-flow gases with same flow rate. With simulated combustion products flowing, the diffusion flame lifts off to a higher elevation compare with co-flowing air, since in simulated combustion products. When the outside air is entrained into the flow field, the flammable mixture can finally be established at the flame base to form the diffusion flame. Thus the simulated combustion products are acting like a shield to prevent the mixing of central fuel stream and oxygen from surroundings, forcing the mixture to burn at higher elevation.

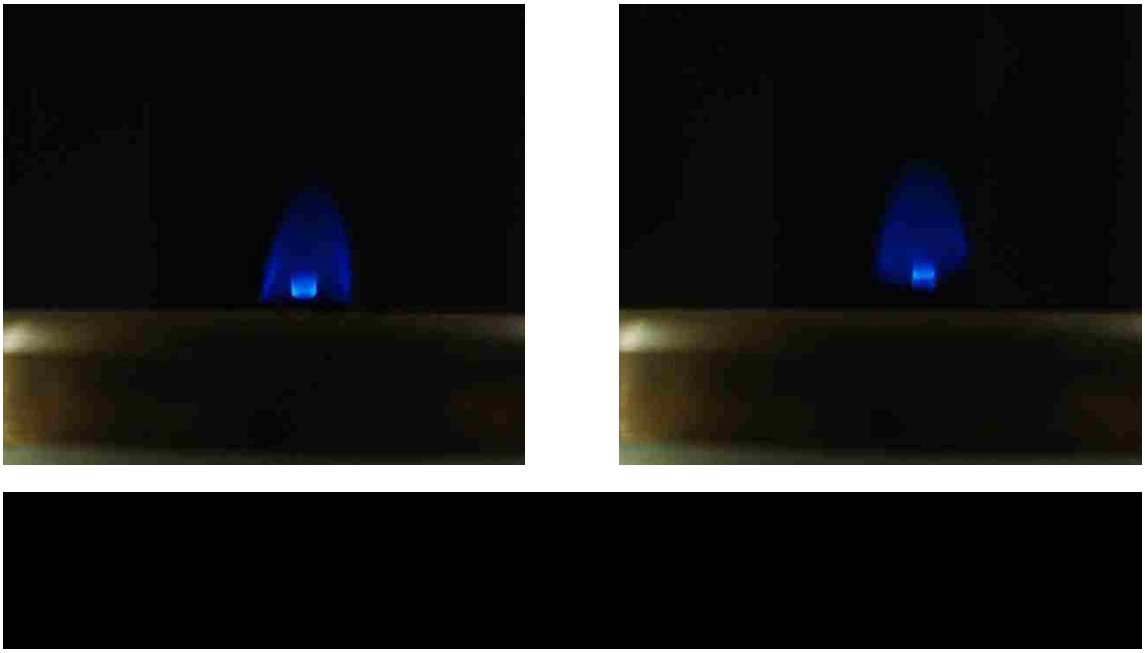

Figure 4.2 shows the second feature change when the simulated combustion products are mixing with central fuel and central air. The shatter speed of the camera is exactly the same when taking these two pictures, but picture on the right shows images of several flames in the same frame, because the flame on the right is oscillating up and down all the time. The flame base is not stable because of the low oxygen concentration at lower elevation, the randomized entrainment of air produces the flammable mixture at different elevation. With simulated combustion products, the IDF is transfered from stable flame to the unstable region. Because the IDF constantly struggles for finding the oxygen, with high simulated combustion products, the flame can be completely

blown-off. Comparing with the co-flowing air case, the blow-off condition can only be achieved by ultra-high flow rate of air.

To explore the feasible flame structures for IDFs with the flow of simulated combustion products, the space diagram has been found. The space diagram serves the purpose to illustrate how the flame structure changes with variation of the velocity of co-flows. As the fuel reformation and flameless oxidation mechanisms are favored by temperature higher than 1000K, the co-flowing simulated combustion products have been pre-heated. Due to the temperature limit of the experimental setup, all experiments with pre-heating, the pre-heat levels are close 700K. Total of eight distinct flames have been identified with co-flowing air and co-flowing simulated combustion products cases with both non-preheating and pre-heating operating conditions. The eight distinct structures are categorized by the relative position of inner flame and outer diffusion flame, and they are:

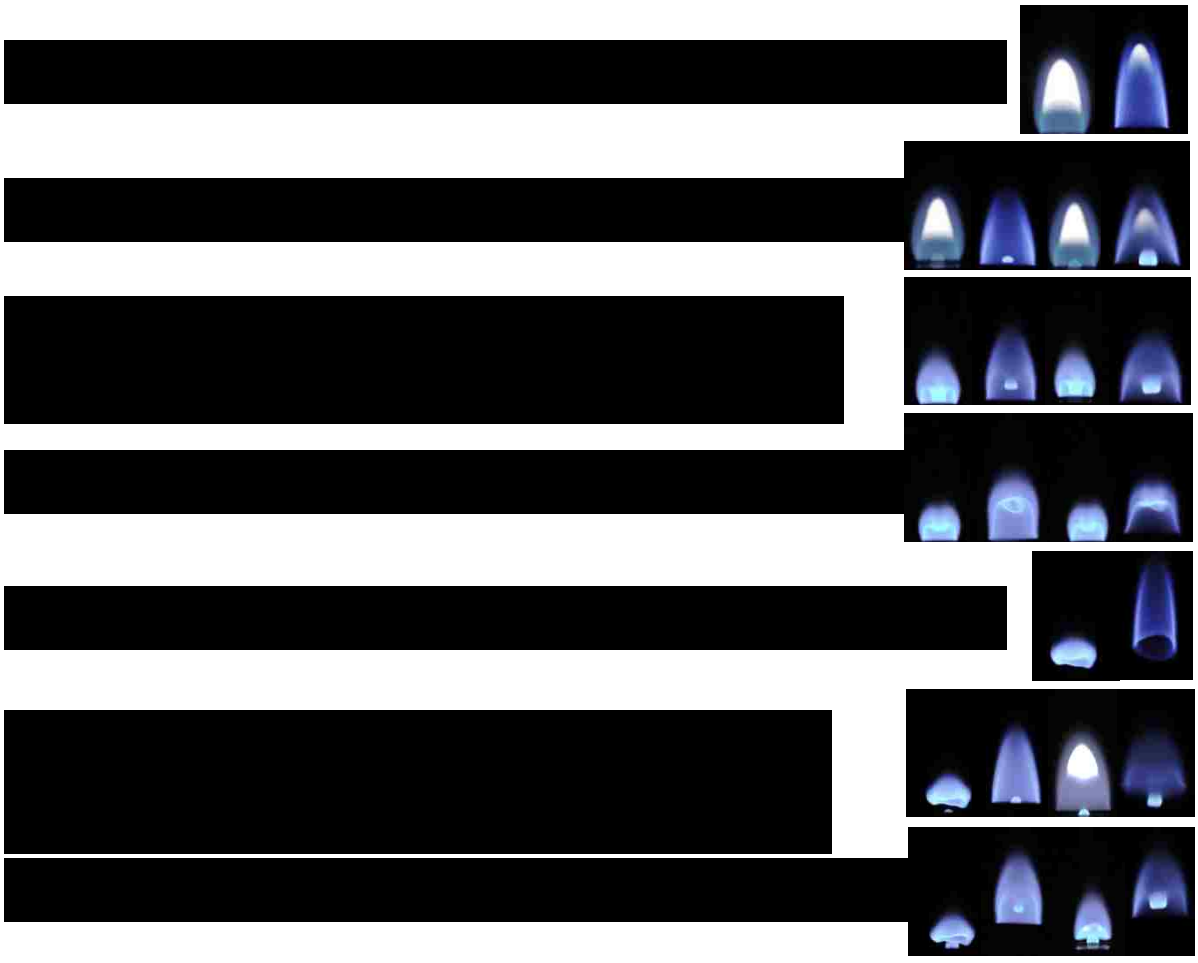

The ‘jointed flame’ is when as the inner flame merged with the outer flame to form an ‘overlapped’ flame. In experiments reported here, the central fuel flow rate is fixed as u_{cf} =9.47 cm/s. The flame structures which inner flame could attach to the burner lip need to a relatively small central fuel velocity. In this study, the volume flow rate of 0.1 liters per minute is selected which is the flow velocity of 9.47 cm/s after conversion.

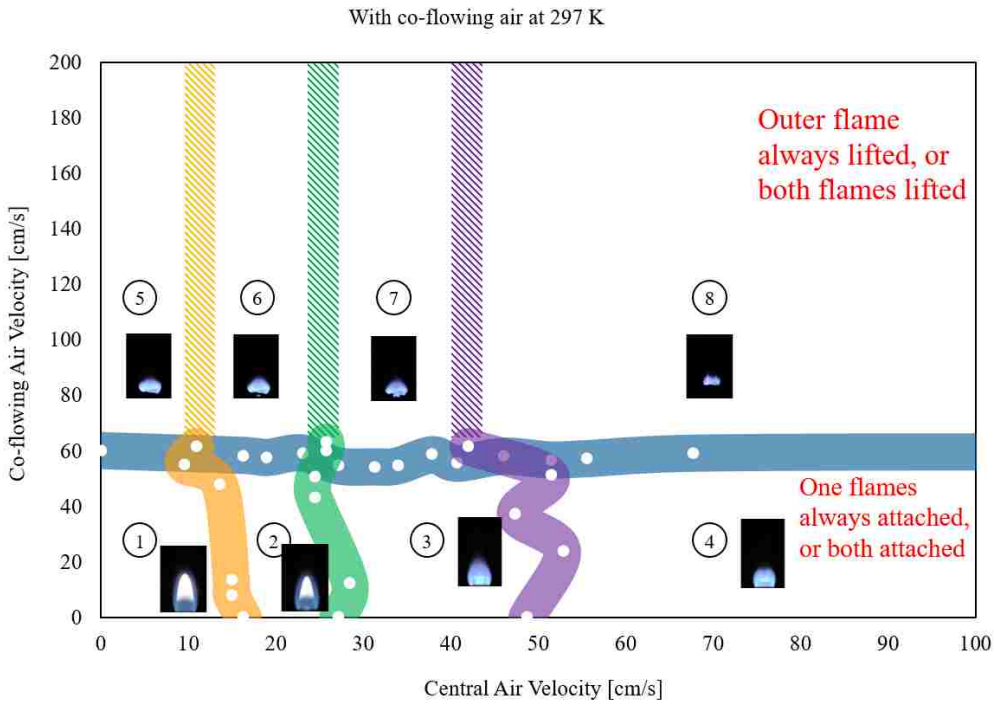

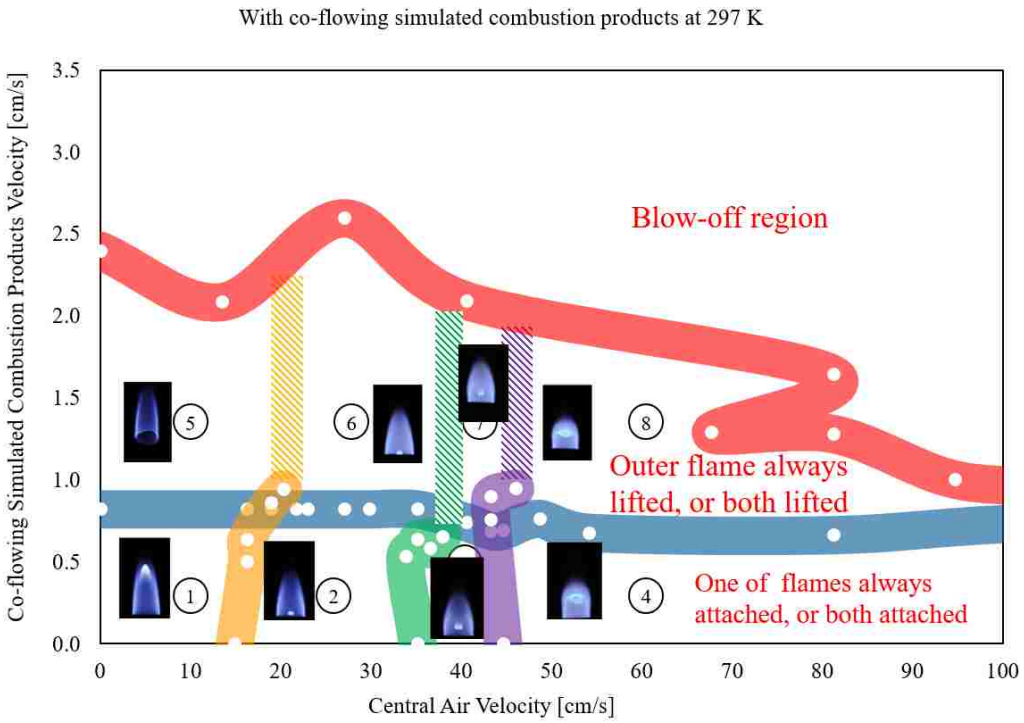

Figure 4.3 and Figure 4.4 shows the space diagram of IDFs with co-flowing air and simulated combustion products without any pre-heating, and illustrate how the central air velocity and co-flow velocity affect the flame structure. Comparing these two figures, the change of scale of co-flow velocity needs to be noticed. For the co-flowing simulated combustion products velocities beyond 2.5 cm/s, the IDF will be extinguished as it enters the blow off region. In contrast, for the co-flowing air case, there is no blow-off region unless the co-flow air running with ultra-high speed. Below the blow-off region, the figures have been divided horizontally to upper part and lower part by the line which represents the separation point of the outer diffusion flame attachment to the burner lip and outer diffusion flame lifted away from the burner surface for all the operating conditions. For the co-flowing air case, the separation occurs at co-flowing air velocity around 60 cm/s, and for co-flowing simulated combustion products, the separation point is around co-flow velocity at 0.75 cm/s. Above the separation curve, the outer flame is always lifted, or both flame

are lifted when the central air velocity is increased. Below the separation curve one of flame is always attached to the burner nozzle or both are attached. As the outer diffusion flame is formed by the mixing of central fuel jet and co-flow, the lift-off characteristic of the outer diffusion flame is governed by the co-flow velocity for the central fuel velocity is constant. Similarly, the inner partially premixed flame is formed by the mixture of central air jets and central fuel jets, the lift off characteristic is controlled by the central air flow rate at fixed central fuel velocity. For flame configuration ① to ② or ⑤ to ⑥ in the space diagram, with the central air velocity increasing from 0, the IDF starts with no inner flame, then inner flame is established inside the outer diffusion. Because of the hysteresis behavior of the inner flame, the first occurrence of inner flame starts at the lifted position from the burner surface. The hysteresis effect has been discussed in Johnson (2009). By reducing the central air flow rate, the inner flame position jumps back to the burner top. For making the space diagram, the hysteresis effect is discarded, so for all the conditions the inner flame position starts as attached to the burner top. As Figure 4.3 and Figure 4.4 show, from flame configuration ② to ④ or ⑥ to ⑧ in the space diagram, once the inner flame is presented in the IDFs, with central air velocity increasing the inner flame position is lift off and eventually merges with outer diffusion flame to form the joined flame. For same inner flame cases, there are dash lines extending across the boundary to the lifted outer diffusion flames. When IDFs enters the lifted outer flame diffusion flame region, the flame structure is really hard to be evaluated just by the visual images, so the dash line separates the potentially different flame structures. In this work, these operating conditions under which the dash line occurs were not explored in details. Even if the co-flowing air and co-flowing simulated combustion products are sharing the same type of flame structure, but the shape of outer diffusion flames are quite different because the co-flow velocities are in different scales.

Figure 4.5 and Figure 4.6 show the space diagram for both types of co-flow with pre-heating to 673 K. Compared with the non-preheating cases, both IDFs with co- flowing air and co-flowing

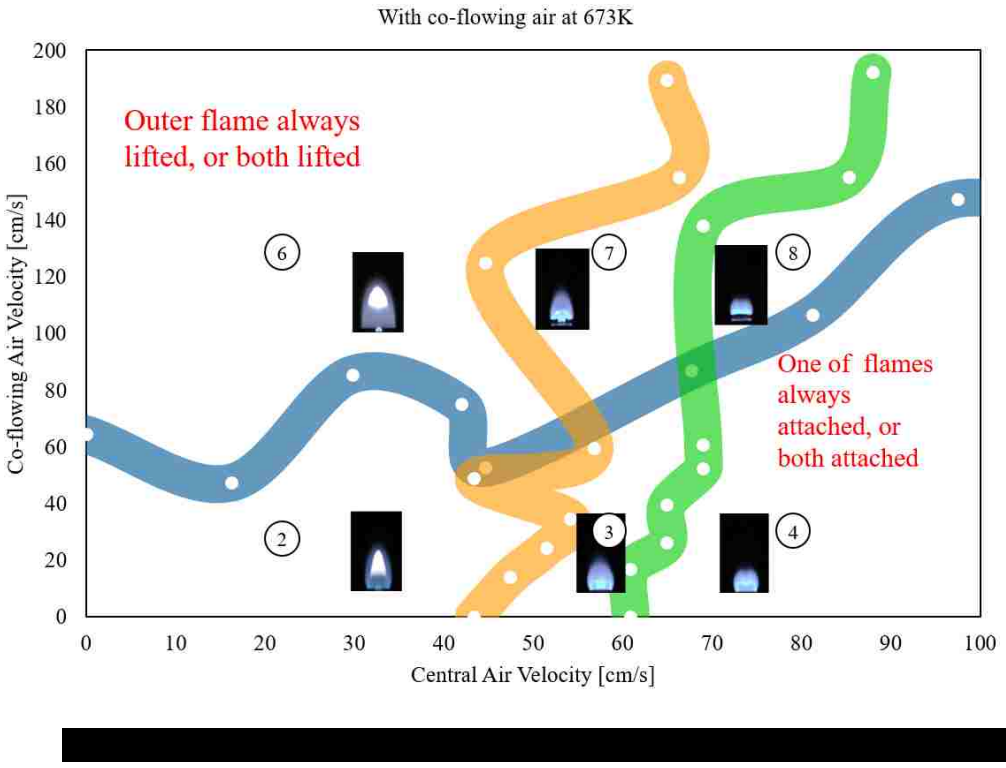
With co-flowing air at 673K
Co-flowing Air Velocity [cm/s]
Central Air Velocity [cm/s]
Outer flame always lifted, or both lifted
One of flames always attached, or both attached
0
20
40
60
80
100
120
140
160
180
200
0
10
20
30
40
50
60
70
80
90
100
2
3
4
6
7
8

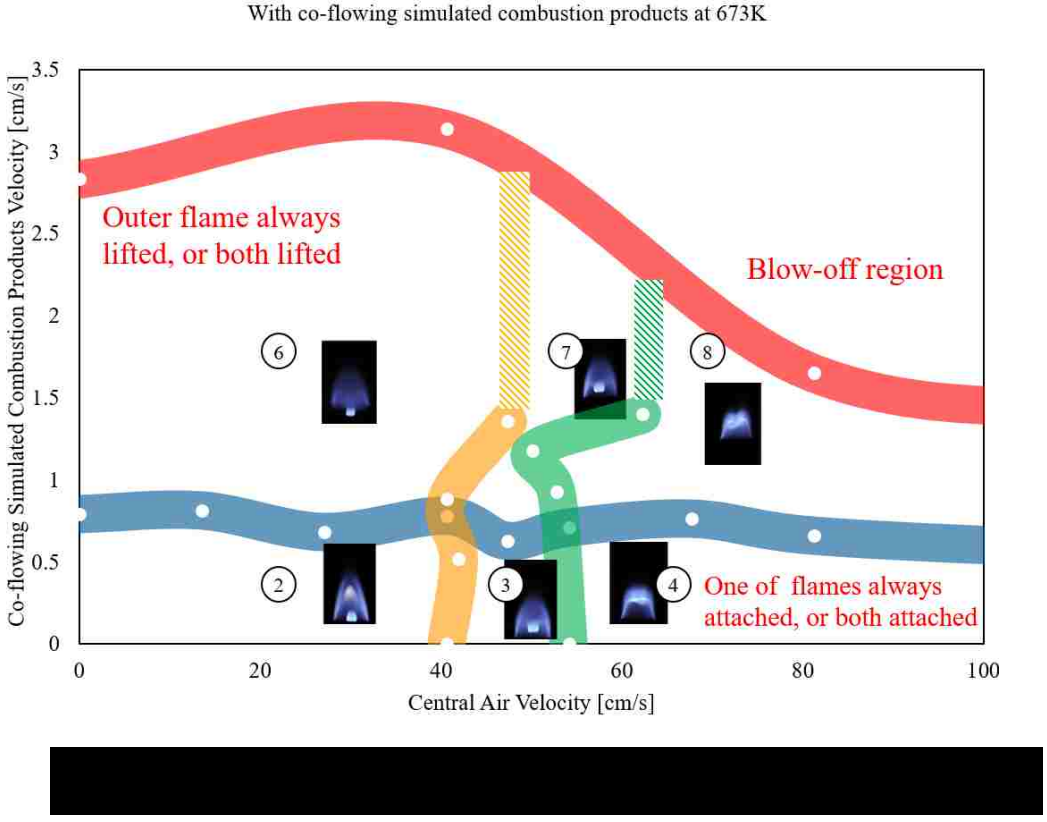
With co-flowing simulated combustion products at 673K
Co-flowing Simulated Combustion Products Velocity [cm/s]
Central Air Velocity [cm/s]
Outer flame always lifted, or both lifted
Blow-off region
One of flames always attached, or both attached
0
0.5
1
1.5
2
2.5
3
3.5
0
20
40
60
80
100
2
3
4
6
7
8

simulate combustion products do not for flame configuration ① and ⑤ in the space diagram (no inner flame and attached outer flame). Instead the space diagram starts (at low central air velocities) with region ② (inner and outer flame attached) for low co-flow velocities, and region ⑥ (inner flame attached and outer flame lifted) for the co-flow velocities above the threshold level. This indicates that at low central air flow rate, pre-heating prevents establishing of the attached outer flame when co-flow has a low velocity, or a lifted outer flame when the co-flow velocity is higher, when there is no inner flame. For the co-flowing air pre-heating case, the separation points for lifted flame and attached flame show large variations with different central air velocities. There is no dash line in this space diagram, as the all the structure types are clearly identify till the upper boundary. Trends in the structure changes are same as the non-preheating case with increasing both central air and co-flowing air velocity. For pre-heated co-flowing simulated combustion products, the operating conditions are still limited to small range of co-flow velocities, and there are some region of operation conditions that outer diffusion flame is lifted and the flame structure cannot be clearly identified. Compare with the non-preheating case, the space diagram follows the same trends in flame structure changes as well. For all the IDFs with pre-heated co-flows, the flame structures become more unstable, especially with co-flowing simulated combustion products as central fuel jet struggled to mix with oxygenate flows to create the mixture in the flame limit region. The shaded line indicates region in which the flame structure is poorly identified as the flame is highly unstable. All the curves are thickened, and they are not necessarily represent the boundaries. The flame structures here have has some differences compared with the non-preheating case.

Figure 4.7 and Figure 4.8 show the details of the flame structure of inversed diffusion flames with both co-flowing air and co-flowing simulated combustion products in non-preheating condition. The flames with co-flowing air case are much brighter than the flames with co-flowing simulated combustion products as there is much more oxygen to mix with central fuel flow. The flame front is much clear with co-flowing air flames which indicates the temperature is also higher since most

of the reaction are happening around the thin narrow flame front region. Haynes and Wagner (1981) concluded that the production of carbon black requires a maximum yield of soot from the flame pyrolysis of a hydrocarbon feedstock. The temperatures between 1500 and 2500 K with carbon present in the fuel create condition for formation of large amount of soot. Soot emissions from a practical combustion appliance reflects poor combustion conditions and a loss of efficiency. In Figure 4.7 ①and②, this two flame structures have large amounts of soot as the fuel stream is exposed to the high temperature at the flame front. These are typical the diffusion flame, so the amount of oxygen is not sufficient to oxidize the carbon particles at the soot formation region. In Figure 4.8 ①and②, with simulated combustion products, the soot formation is suppressed as there is less oxygen mixing with central fuel to form the high temperature reaction region. The outer appearance is dramatically different in co-flowing air case, as the velocity of co-flow is increased. With co-flowing air, the outer diffusion flame is much harder to lift off compare with co-flowing simulated combustion products. Stable IDFs with co-flow air can be formed with small amount of co-flow, as the mixture of central fuel and co-flow is within the flammable limit region when co-flow velocity increases, the outer diffusion flame remains stable. The high co-flow velocity can help to create a much leaner mixture below the lifted outer flame, which there is no combustion occurring. On the contrary, with co-flowing simulated combustion products, there is much less oxygen inside the co-flow, the mixture is at the lower flammable limit region to begin with. Comparing flame configurations ⑤ to ⑧ in Figure 4.7 and Figure 4.8, increasing the velocity of co-flowing simulated combustion products can easy lead to the formation of mixture leaner than the lower limit, so with small amount of co-flowing simulated combustion products, the outer diffusion flame is much easier to lift up compare to co-flowing air cases. The equivalence ratio $\phi = 0.57$ is the lower flammable limit for methane air mixture, and much larger amount of lean combustion products are needed to reach the flammable limit for methane and lean combustion products mixture, since less oxygen concentration inside the combustion products. Because of the

high co-flowing air velocity for flame configurations ⑤ to ⑧ in Figure 4.7, the lifted outer flame structures are compressed to a much smaller flame compare IDFs with co-flowing simulated combustion products. In Figure 4.7 flame configurations ⑤ to ⑧, and Figure 4.8 flame configurations ⑤ to ⑧, the inner flame of both co-flowing air and simulated combustion products remains almost the same with increasing co-flow velocity when the flow rate of central air is fixed. In the space diagram, flame structures in the explored region clearly show the thin flame fronts as the temperature for the mixture is not in the region where fuel reformation and flameless oxidation occurs, and the mixing of central fuel and air jets with co-flow is not well distributed to form a uniformed mixture. The pre-heating is needed to get closer to the flameless oxidation and fuel reformation operation region, and better mixing strategy as well.

To pre-heat the co-flowing to over 1000K is above the maximum temperature limit of the experimental setup in this work. The pre-heating temperature is set to around 673K which is the maximum temperature that currently can be achieved. In Figure 4.9 and Figure 4.10, the IDF structure with co-flowing air and simulated combustion products at 673K. As there is no cases with no inner flame, only six type of structures are presented in the space diagram. Compare flame configurations ② to ④ and ⑥ to ⑧ in Figure 4.9 and Figure 4.10, the outer diffusion flame in co-flowing air cases is still much brighter than it is in co-flowing simulated combustion products cases due to the oxygen concentration difference between these two co-flows. In the space diagram, because of the co-flow velocity scale difference, the outer flame heights shows the similar trend compare with non-preheating case as the outer flame is much shorter as it lifts from the burner surface. Soot emission in flame configurations ② and ③ (in Figure 4.9), in co-flowing air case remains large as the high temperature around flame front breaks up the fuel to form a bright soot region, with co-flowing simulate combustion products the yellowish flame is only present in flame configuration ②, and it is much less luminescent as less soot has been produced. When the co-flow

flow rate increases to lifted outer flame, the mixing of co-flow and central fuel is enhanced, the soot formation decreases dramatically as yellow color is eliminated from IDF. Comparing with pre-heated co-flowing air case, pre-heating of co-flowing simulated combustion products makes the flame highly unstable as the flames in Figure 4.10 is highly non-symmetric. For these unstable flames with co-flowing simulated combustion products, the outer diffusion flame is lighter in color the non-preheating case. In contrast, for flames with co-flowing air, outer diffusion flame is shown a bright thin reaction zone except flame configuration ⑥ in Figure 4.9. With outer diffusion flame lifted, the co-flow velocity is higher than the attached case. Because of the higher velocity, the interaction of co-flow and central fuel jet is increased, resulting in better mixing. Comparing flame configuration ② and ⑥ in Figure 4.9, with smaller central air interact with central fuel jet, the lifted outer flame eliminated the thin flame front, and the outer flame is more distributed to two side of the burner compare with the non-preheating case. With co-flowing simulated combustion products, the outer flame is not presented as a bright thin reaction zone any more, instead it presented as a dim flame zone surrounds the inner flame, and reaction area gets extended comparing flame configuration ⑥ with the non-preheating case. The flame configuration ⑥ in Figure 4.10 with co-flowing simulated combustion products has the outer diffusion flame which is distinct from other cases, as the outer flame is hard to visualize now, and the reaction zone extends to even wider position. From the visual image, the outer flame region is approaching the features of flameless oxidation. For simulated combustion products, the main component is nitrogen, and to identify the cause of flame structure difference between two different co-flows, the nitrogen co-flow has been introduced to explore the nitrogen concentration effect on the IDFs.

Figure 4.11 depicts the six types of flame structure, the attached inner flame with attached/lifted outer flame cases is not shown here. The outer flames of all flame structure types have distinct thin flame front, and is always lifted. With co-flow nitrogen, the outer flame can only be formed by combustion of the mixture of central fuel and entrained surrounding air, and nitrogen is acting as

the curtain gas here. For this case, the formation of outer flame is no different than that with non-pre-heated co-flowing air case, except outer flame has always been lifted with co-flowing nitrogen as the extra distance is needed for central fuel jet travel to the higher elevation to mix with outside air entrained into the flow field. Figure 4.11 indicates the high concentration of nitrogen does not change the flame structure too much. The carbon dioxide and oxygen concentrations play a very important role in the flame structure formation as that is the major difference of co-flowing air and simulated combustion products.

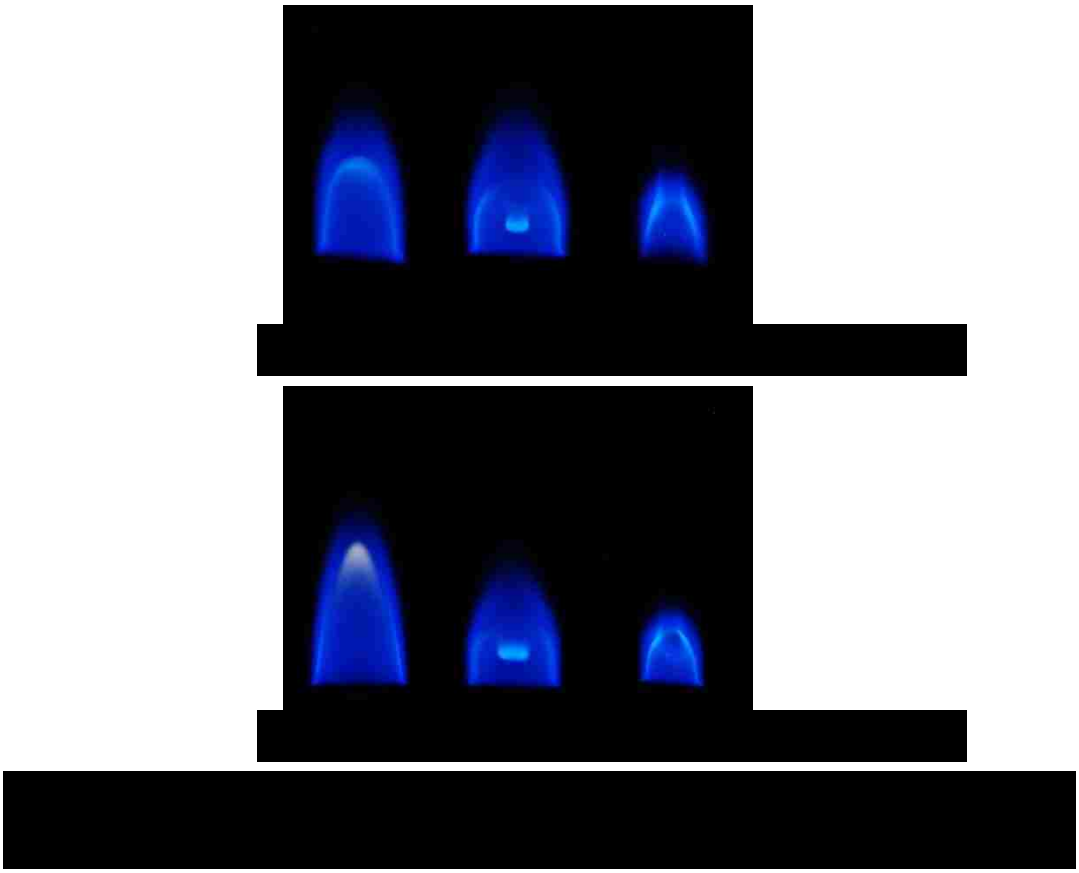

Table 4.1: Central air and co-flow running conditions for Figure 4.11

Operation Conditions

Picture #	$u_{central\ fuel}$ (cm/s)	$u_{co\text{-}flow}$ (cm/s)
1	0	0
3	36.538	0.493
4	147.5	0.493
5	0	0.839
7	36.538	0.667
8	167.804	0.987

4.2 Flame Structure Based On CH Imaging*

To explore the details of flame structure, the CH* contours can indicate the relative positon of inner flame and outer flame. The exposure time was adjusted to 20ms with 256 images being averaged. For unstable flame, short exposure times are needed to compensate for the flame position variation when the images are being taken. The same exposure time setting has been applied to all the other conditions. The relative chemiluminescence intensity has been used to process all the CH* images instead of the absolute chemiluminescence intensity. The reconstructed flame shapes and locations are processed based on the relative chemiluminescence intensity of CH* images as well. An artificial filter has been applied on each image during image processing. The area of CH* intensity value less than 20% of highest CH* intensity value has been filtered out. The regular CH* images have been inverted, so the dark region corresponding to high levels of CH* intensity emission. Based on the space diagram with 4 different co-flow conditions, the CH* images are sampled for each flame structure category at various operation condition.

In the following figures, the first picture in each group is the inverted CH* image, followed by the half of original CH* image after Abel transform divided by centerline, and the last picture is the CH* contour after image processing of the second picture.

4.2.1 Cold Co-flowing Air

With co-flowing air at ambient temperature, there is an outer diffusion flame always existing in each case which indicated by the dark region along the central fuel and co-flow mixing region. The inner partially premixed flame appears as a ‘bubble’ shape of flame attach to the burner surface as dark black region at the center (u_{ca}=20.3 cm/s). As the central air velocity increases, the inner flame moves higher till reaches the outer flame. For outer diffusion flame, increasing the co-flow velocity results for a short lifted of the flame position, and dramatically shrink the flame size, and position is moving towards the centerline. With increasing the co-flow air velocity, the outer flame moves upwards and then just stays at a certain elevation, as the co-flow velocity is large enough to trap

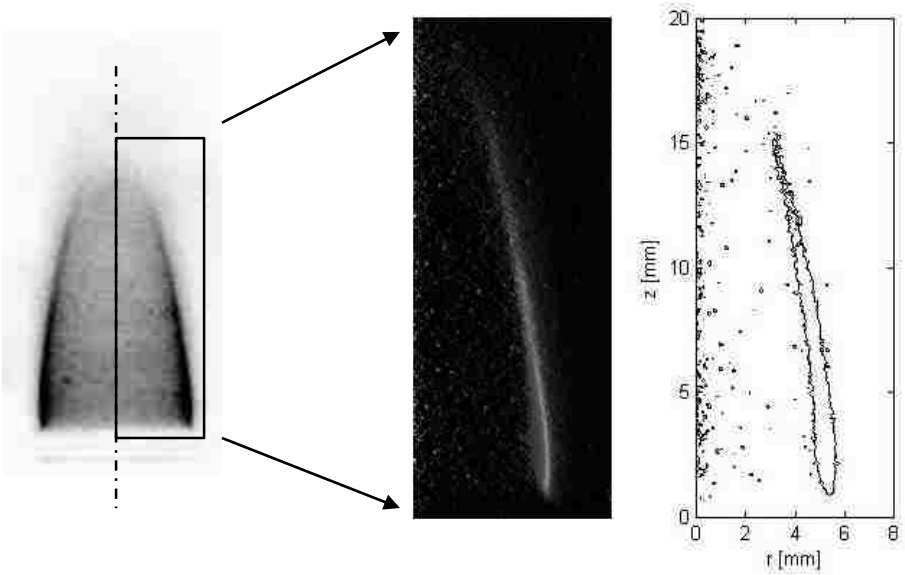

[redacted]

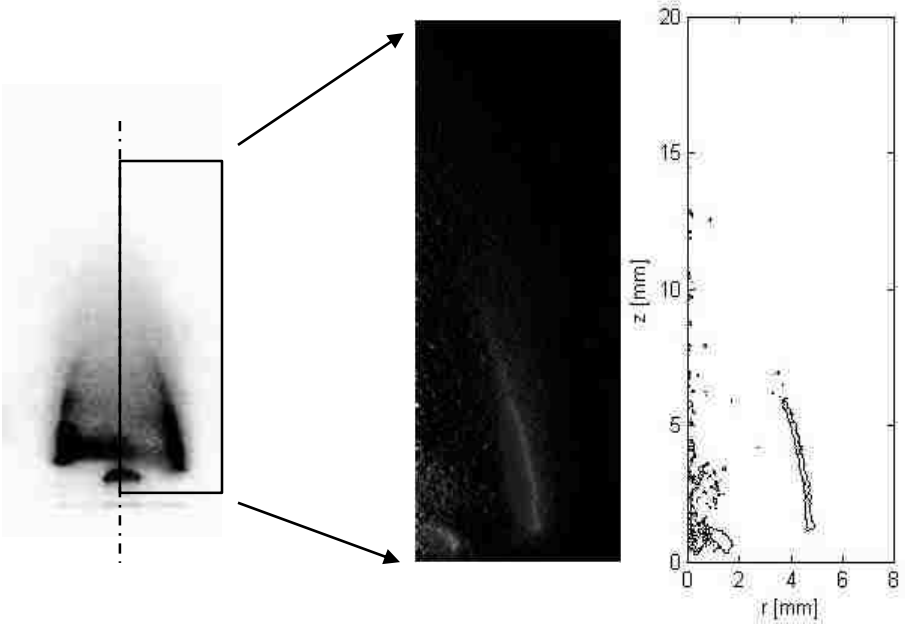

[redacted]

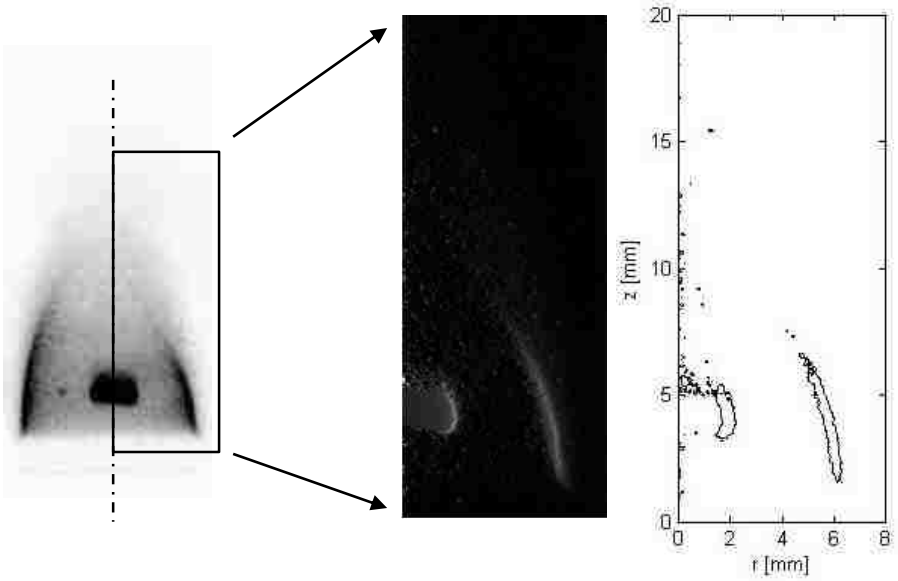

[redacted]

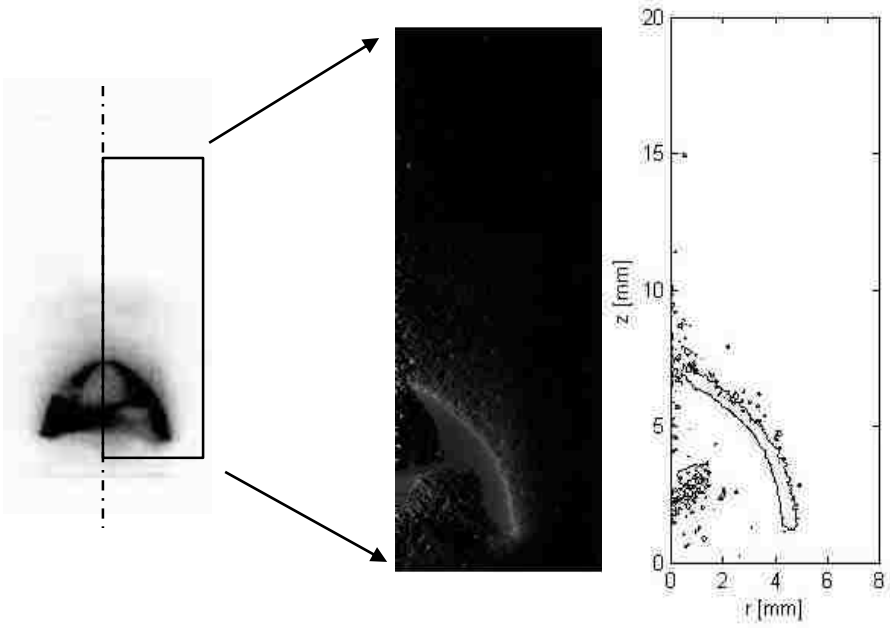

[redacted]

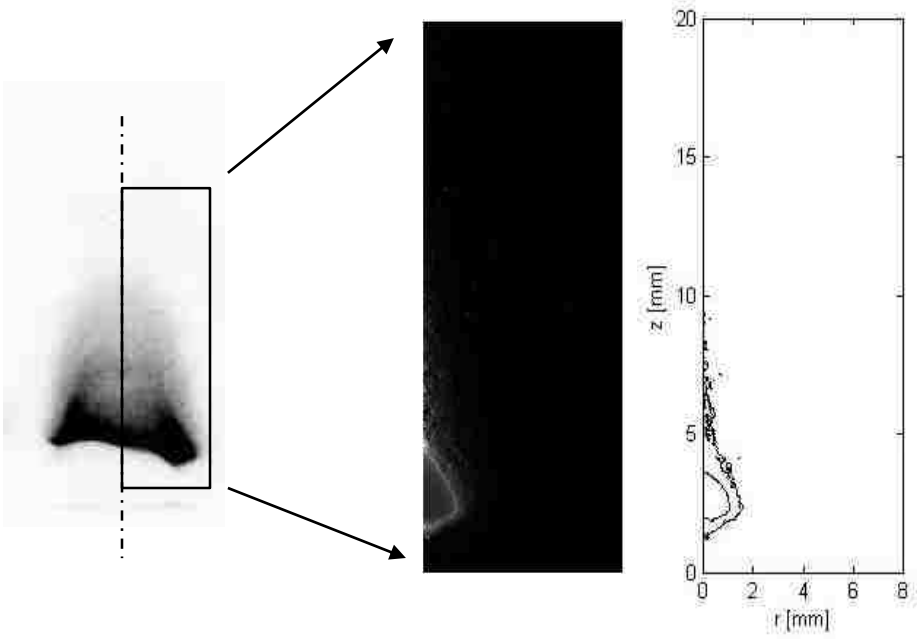
z [mm]
r [mm]
0
5
10
15
20
0
2
4
6
8

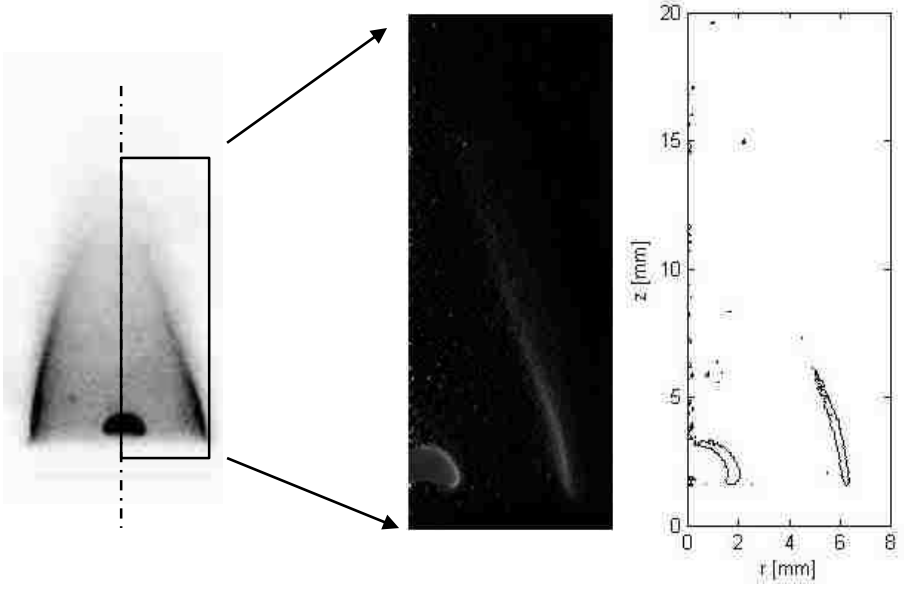
z [mm]
r [mm]
0
5
10
15
20
0
2
4
6
8

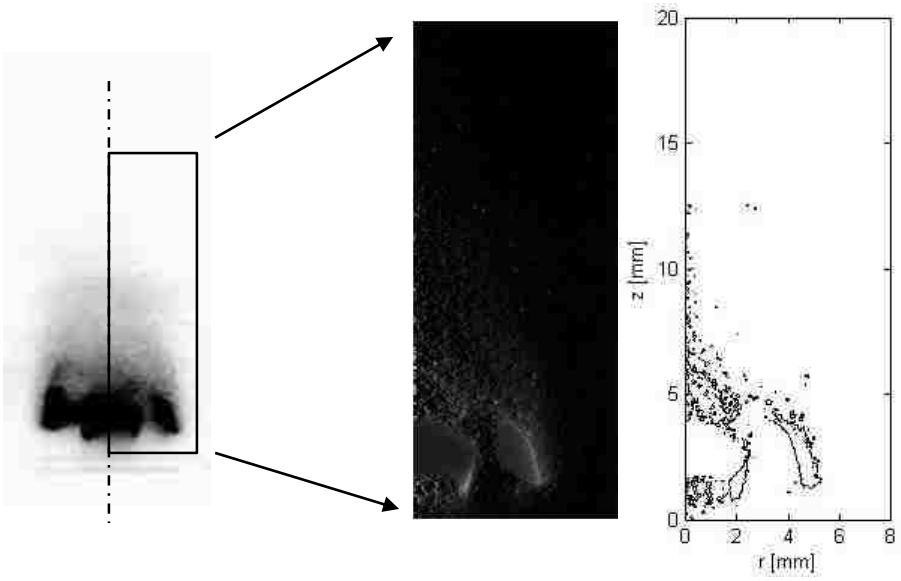
20
15
10
5
0
z [mm]
0
2
4
6
8
r [mm]

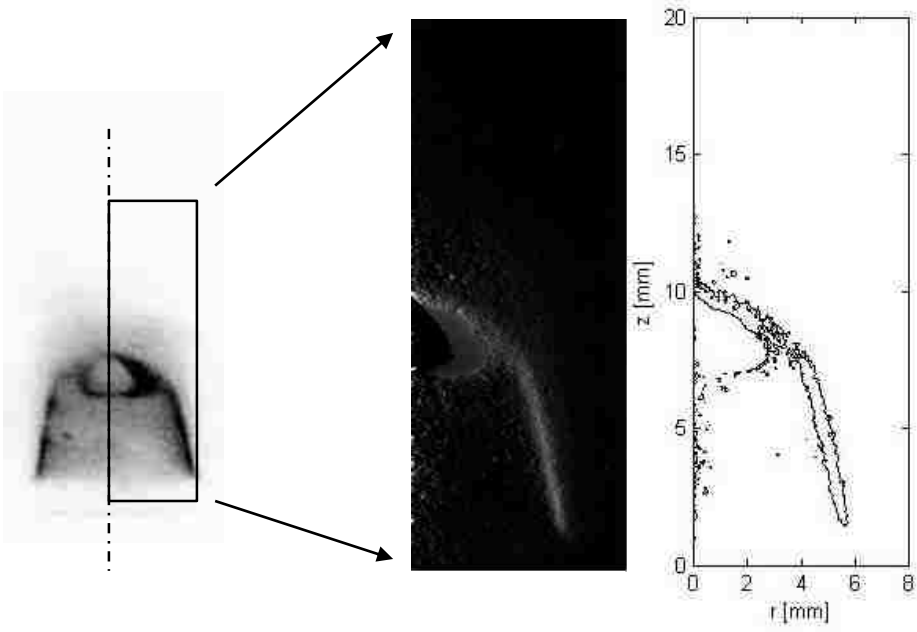
20
15
10
5
0
z [mm]
0
2
4
6
8
r [mm]

the central fuel jet at this height, and force the mixing and reaction occurs at this particular location. With high of central air and co-flow velocity, the double flame merges together to form a flame which flame center is hollowed as a ring shape eventually. The outer flame lifting distance is quite small comparing with the non-lifting case, so in the CH* contours the bottom of outer flame locates around a small height rage.

After the inner flame presents in the reaction zone, the position change can be clearly identified. The inner flame is much sensitive to central air velocity change comparing with influence of outer flame by co-flow. The different mixing characteristics results in dramatic sensitivity difference between inner flame and outer flame. When central air velocity start increasing from 0, the mixture start from infinite rich condition, when the equivalence ratio enter the flammable region and inner flame presents. The outer flame is formed at the very beginning as a diffusion flame when co-flow velocity is 0. Sufficient amount of oxygen exists at the surrounding is making sure the equivalence ration of outer flame always falls in the flammable limit region. Higher the co-flow velocity, the stronger the co-flow jets become, as fuel jet velocity is fixed in a small value, the weaker fuel jet gets pushed towards the center axis. Rapid mixing of central fuel jet and co-flowing air jets allows the outer flame occurs at a very large range of co-flow velocity, only extreme high co-flow velocity will distinguish the outer flame which is not showing in the space diagram and will not be discussed in this work. From all the CH* contours showing above, the distinct outer flame presents in all flame types which gets proved again from the colored images.

4.2.2 Hot Co-flowing Air

To favor to flameless oxidation mechanism, the co-flow get pre-heated to a higher temperature. The chain effect of pre-heating the co-flow is both central air and central fuel jets gets pre-heated as well. Temperature at the exit of both jets is around 200℃ since at the time co-flow gets pre-heated at premix chamber, the entire burner has been heated up which including the stainless steel pipes delivering central air and central fuel. In results, the flame structure is quite different from

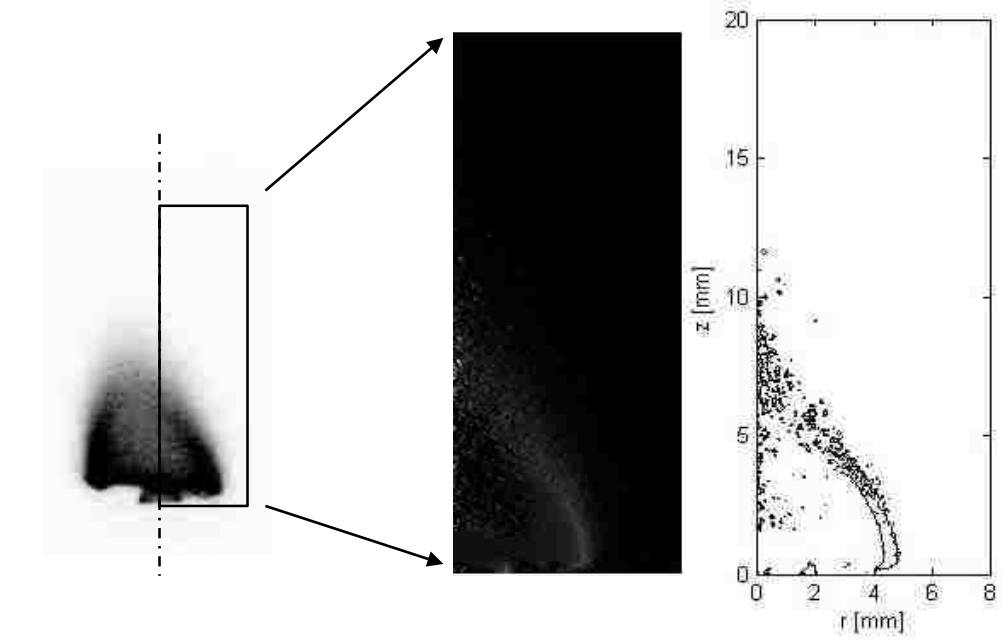
20
15
10
5
0
z [mm]
0
2
4
6
8
r [mm]

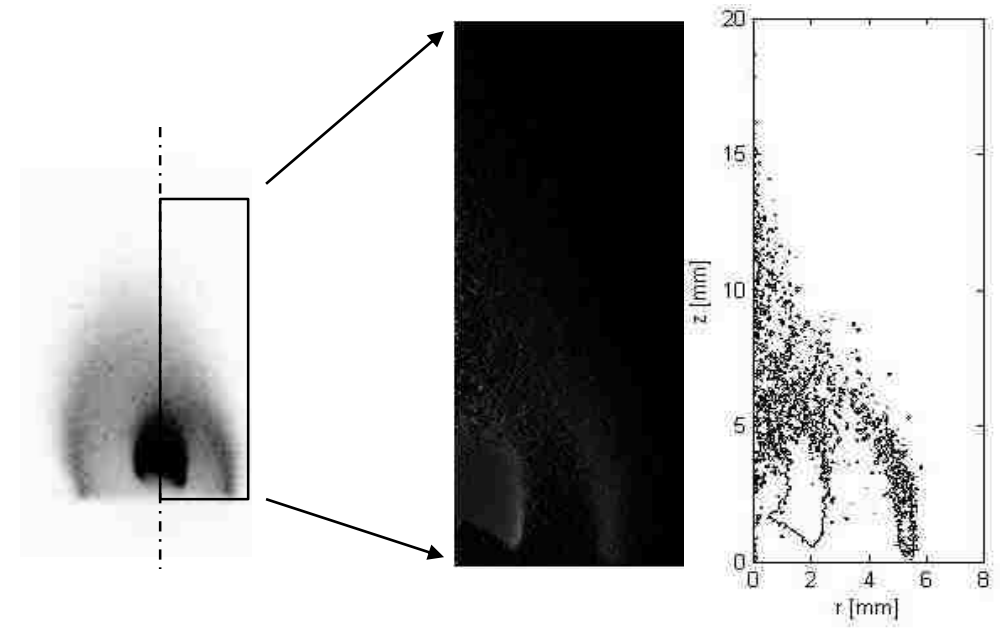
20
15
10
5
0
z [mm]
0
2
4
6
8
r [mm]

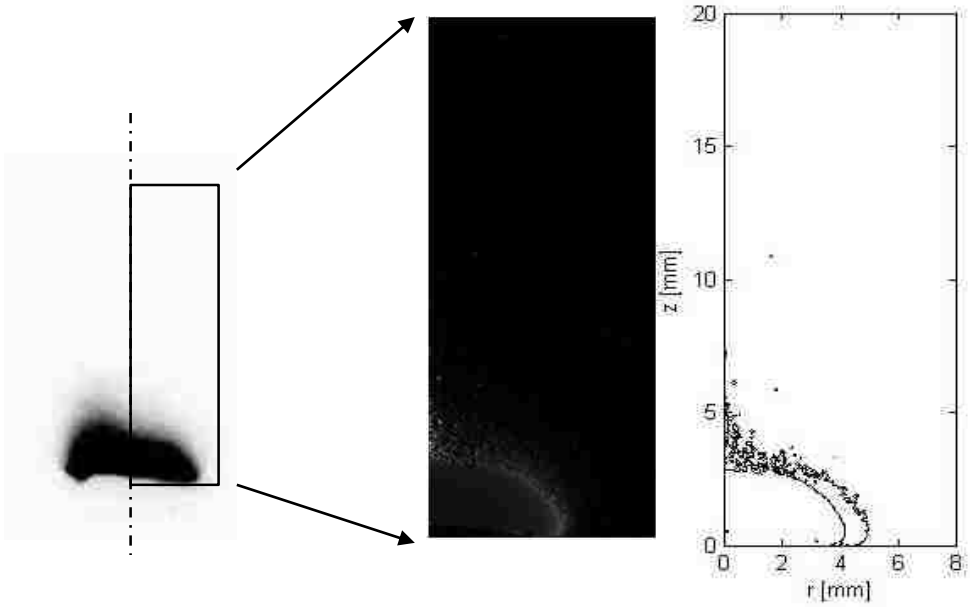
20
15
10
5
0
z [mm]
0
2
4
6
8
r [mm]

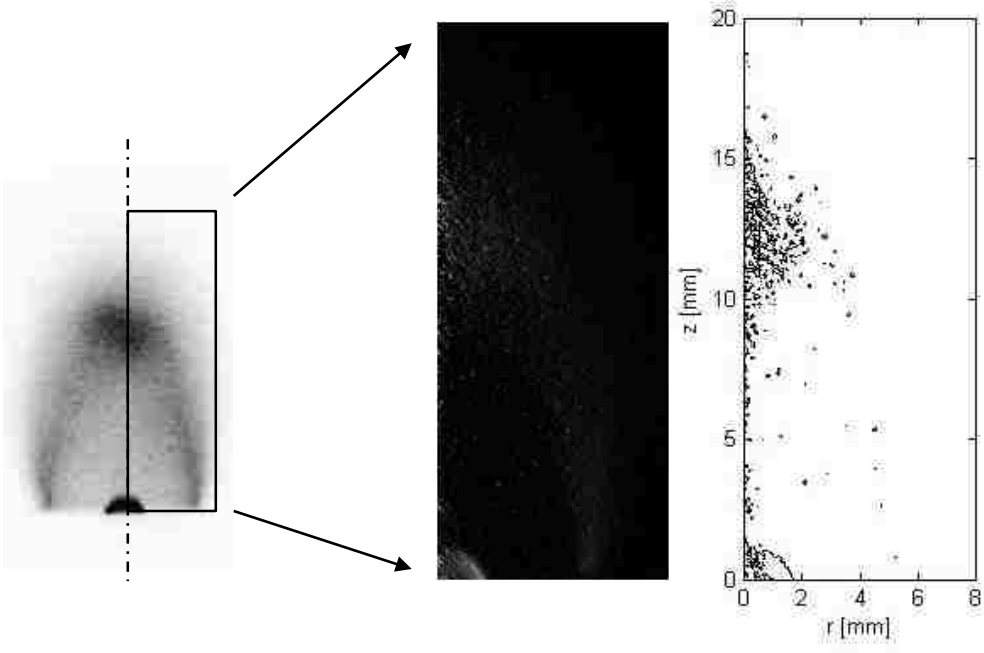
20
15
10
5
0
z [mm]
0
2
4
6
8
r [mm]

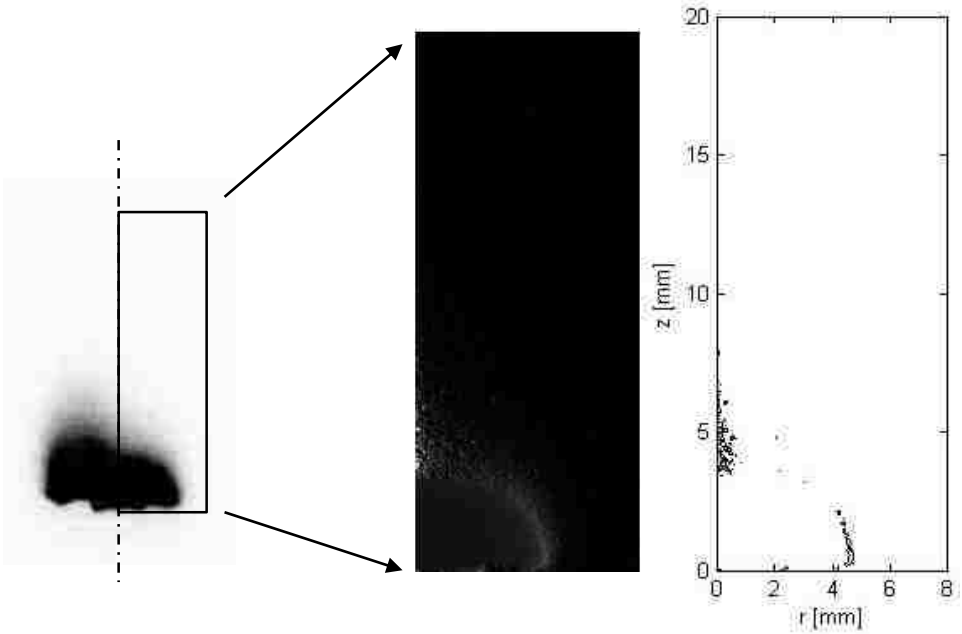
20
15
10
5
0
z [mm]
0
2
4
6
8
r [mm]

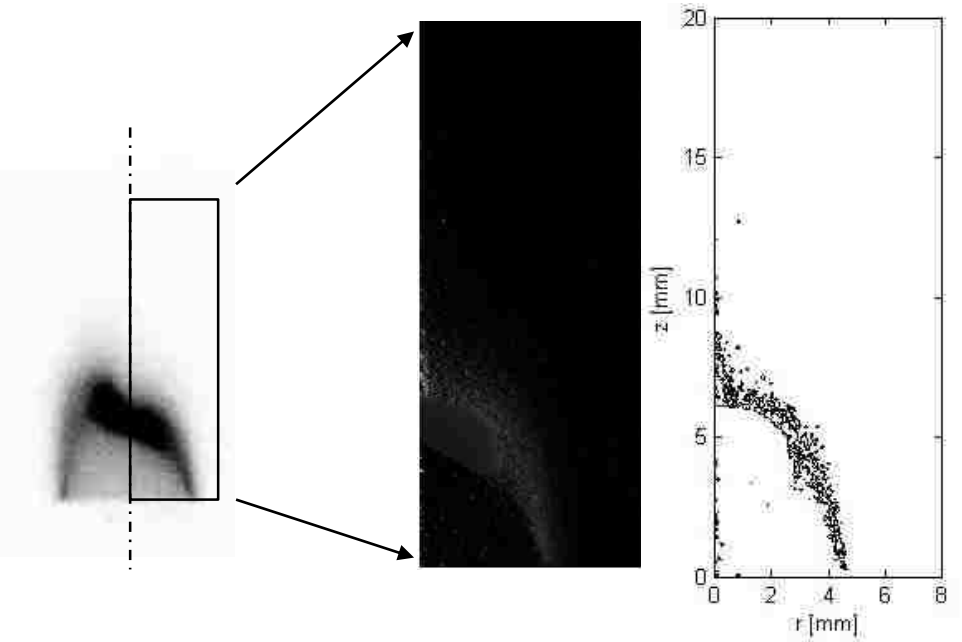
20
15
10
5
0
z [mm]
0
2
4
6
8
r [mm]

the non-pre-heating case. With co-flowing air, the outer flame still cannot be lifted without a high co-flow velocity which the similar characteristic are shared with non-preheating case as well. The outer flame position gets pushed away from center axis when co-flow velocity is low, but eventually the high co-flow velocity squishes the out flame back towards the center axis to end up with tiny flame ball shape which ends up similar to the non-preheating co-flowing air case with high co-flow velocity. The double flame cannot be blew off unless the ultra-high co-flow velocity presents, which as the space diagram shows, the blow-off region remains unidentified in this case. From Figure 4.20 and Figure 4.25, the CH* level of outer flame has a dramastic decrease, and no thin flame front can be identified from CH* contour, scattered CH* species is crowded at the tip of the outer flame along the center axis.CH* contour of Figure 4.21 does not pick up two much CH* species around outer flame region due to the aritifical filter has been applied on. CH* image after Abel transform has more clear indication of the CH* species distribution. By increasing co-flowing air velocity, the bright outer flame is reformed which is the black region of the inverted CH* images, and thin flame front occurs in reaction zone. In some cases, the flame is too bright which after Abel transform, large portion of CH* species has been blocked like Figure 4.22. When co-flow velocity is high, the central fuel jet expansion gets limited, and the mixture gets pushed towards the center axis again. The oxygen and fuel mixture are highly concentrated at a small region to form a normal diffusion flame at the outer flame region which CH* species are crowed in this region as well. Thin flame fronts can still be identified at each case except flame configuration⑥. To explore the potential operation conditions for fuel reformation and flameless oxidation, the pre-heated simulated combustion products is introduced to compare with co-flowing pre-heated air case.

4.2.3 Cold Co-flowing Simulated Combustion Products

With non-preheated simulated combustion products case, the oxygen concentration changes to make the flame structure different from the non-preheating air case as the figures show as followed. The velocity range of co-flowing simulated combustion products has been limited to a much

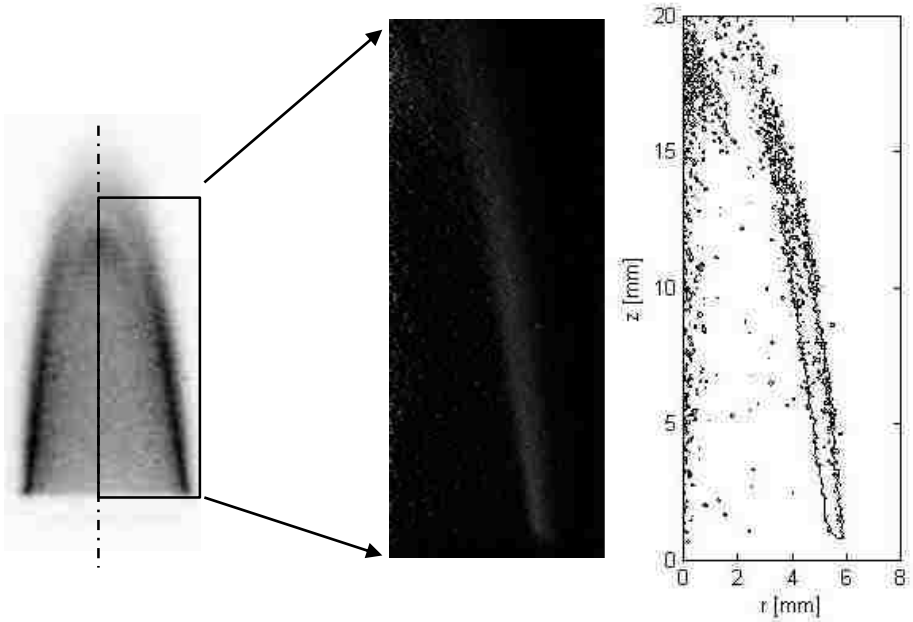

[redacted]

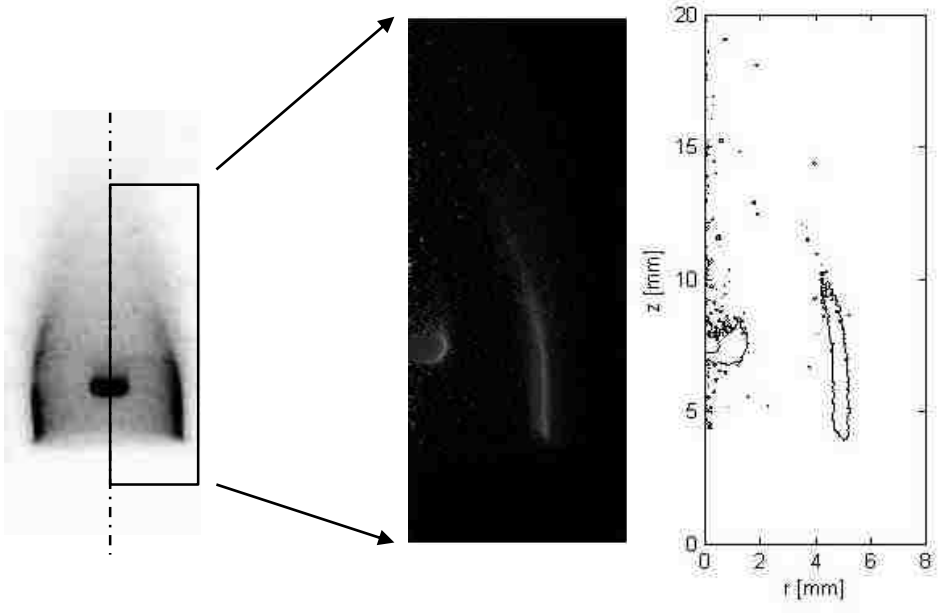

[redacted]

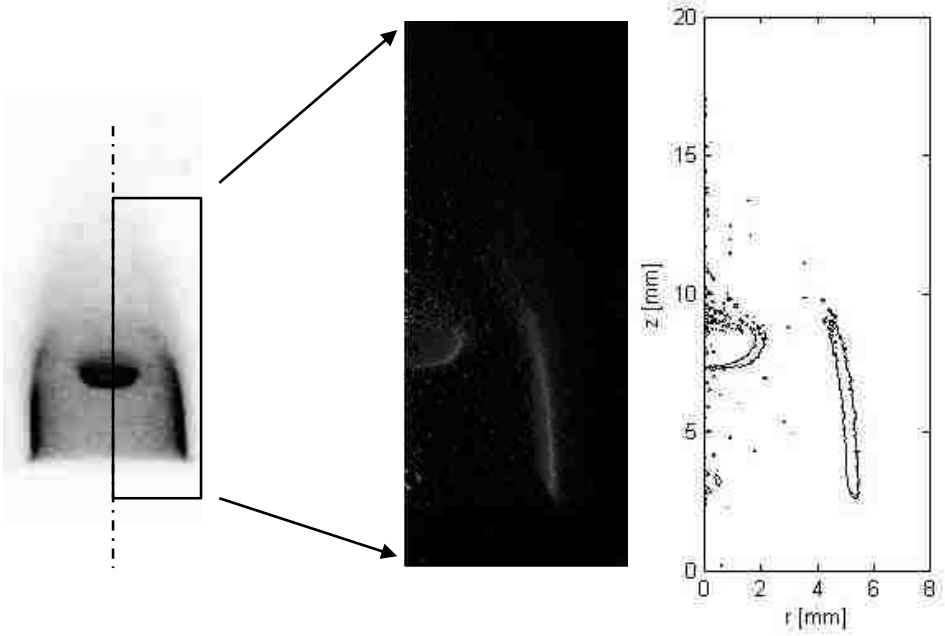
20
15
10
5
0
z [mm]
0
2
4
6
8
r [mm]

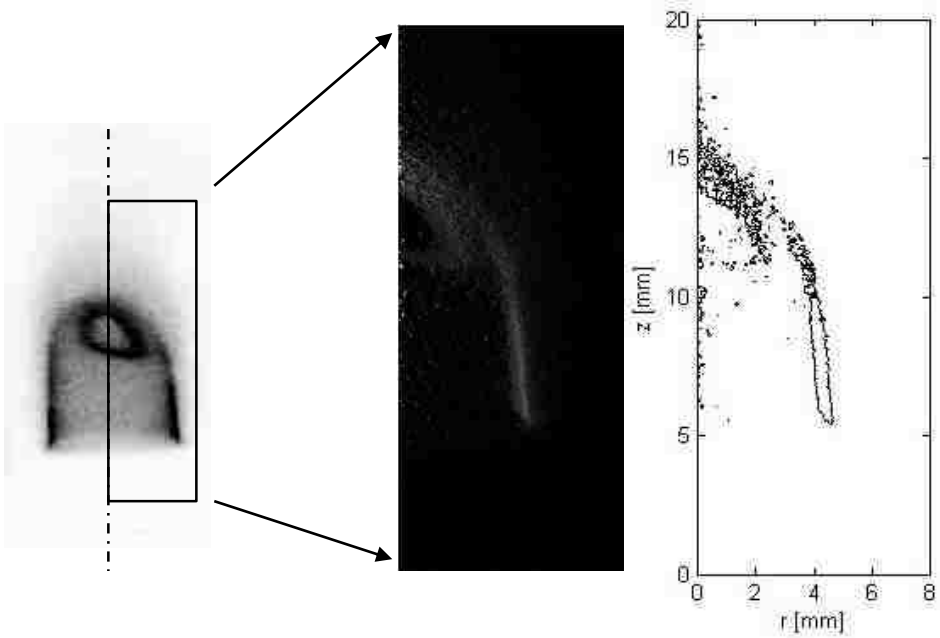
20
15
10
5
0
z [mm]
0
2
4
6
8
r [mm]

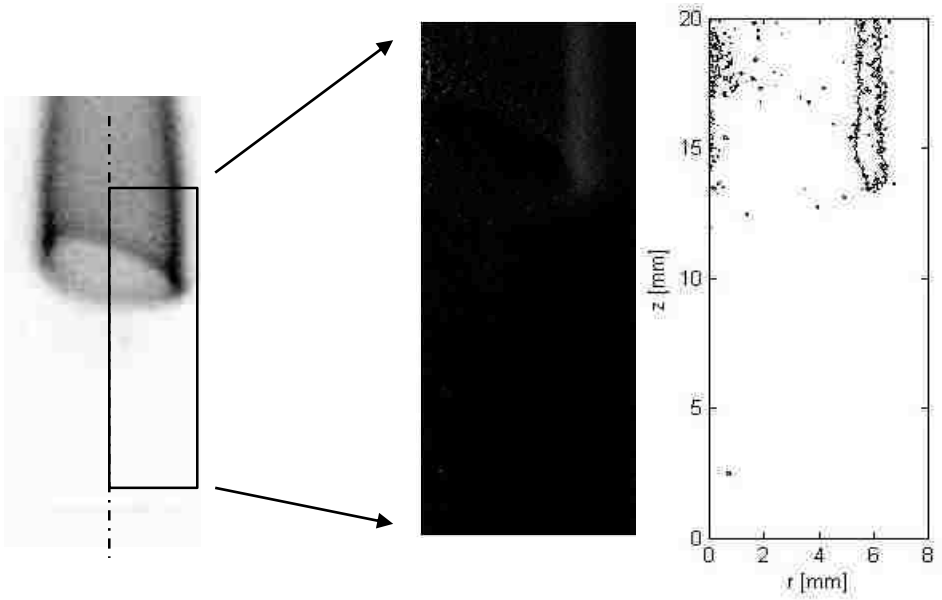
20
15
10
5
0
z [mm]
0
2
4
6
8
r [mm]

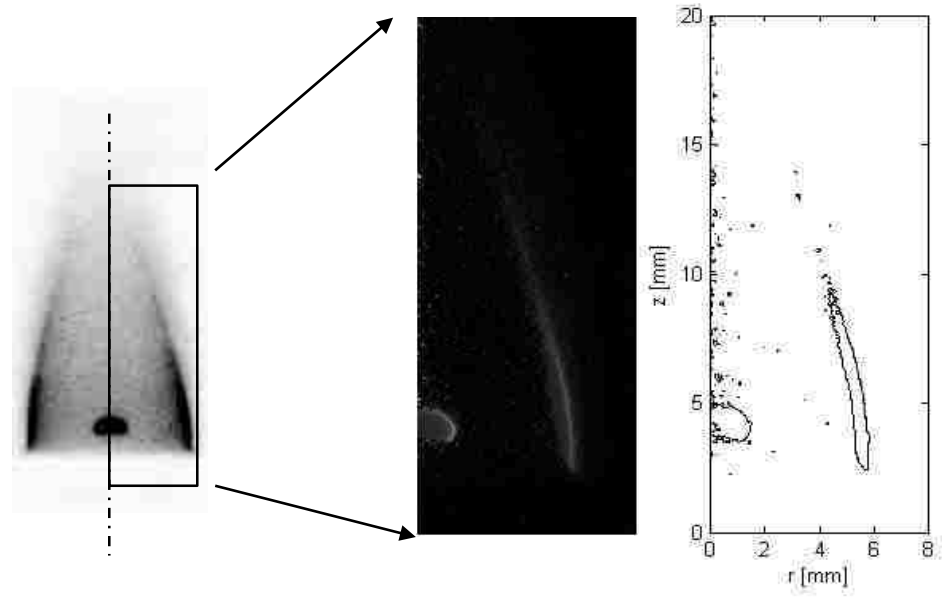
20
15
10
5
0
z [mm]
0
2
4
6
8
r [mm]

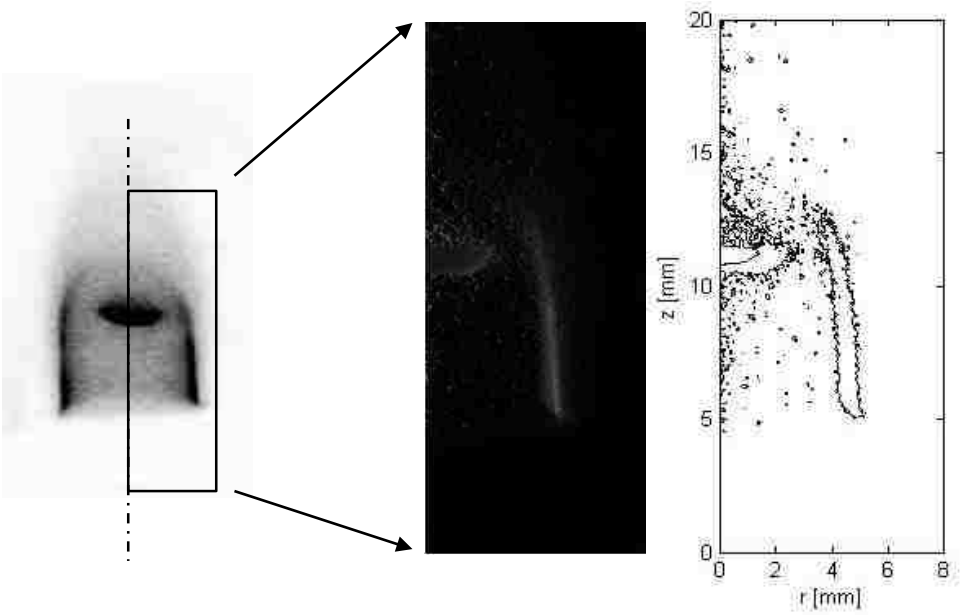

[redacted]

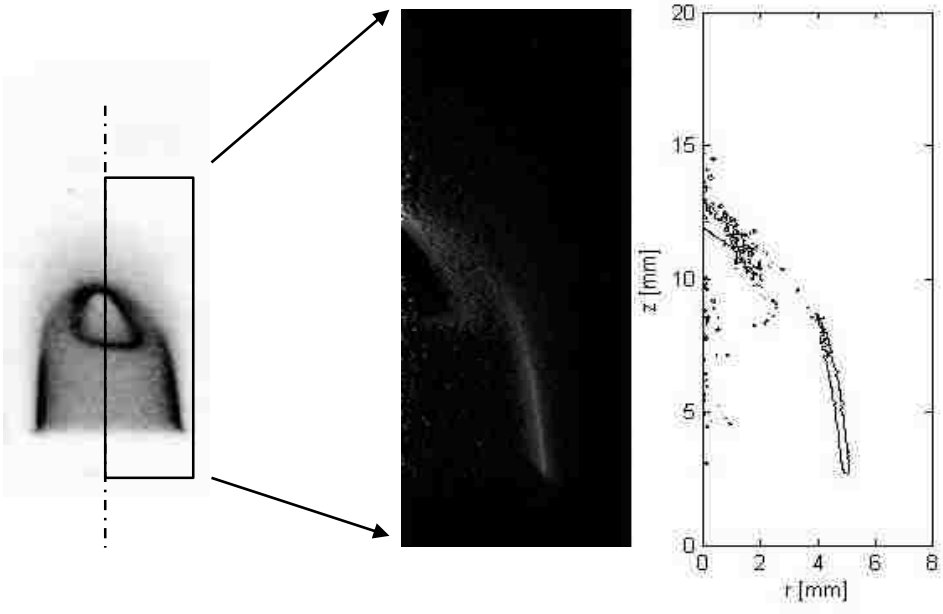

[redacted]

narrower range compare with co-flowing air as the mixture is surpassing the upper limit of the flammable region with a much smaller co-flow velocity. Low concentration of oxygen makes the equivalence ratio of mixture easily getting into the fuel rich region resulting the outer flame gets lifted up as the flammable mixture can be formed when surrounding air gets entrained, so when the co-flow velocity is higher, the harder air can get entrained to the same level. From the CH* contours, the outer flame is much more easy to lift up comparing with co-flowing air case. The outer flame is formed mainly by the mixture of central fuel and surrounded air instead of just central fuel with simulated combustion products. At lower levels, the flammable mixture is hardly to form when co-flow is running. The flame structure of attached and lifted outer flame case are very similar except the flame heights are different. For Figure 4.27 and Figure 4.31, the inner flames are a little bit offset from the tip of central air pipe, especially the inner flame in Figure 4.27, it is lifted with outer flame. After several experimental test for the same case, the inner flame cannot independently exists underneath the outer flame when co-flowing simulated combustion products are running, the entrainment of co-flow eliminates the central "bubble" shape of flame by lowering down the oxygen concentration. As the figure shows, the inner flame can only presents at the bottom edge of the flame. Distinct thin outer flame still can be clearly identified from the CH* contours, by introducing simulated combustion products as co-flow, the chemical reaction gets delayed as combustion occurs at higher elevation for outer flame. Entrainment of ambient air brought the low oxygen concentration mixture back to flammable limit region and diffusion flame gets immediately formed so the thin reaction zone occurs. No evidence of flameless oxidation has been shown in all the flame types in this operation condition with non-preheated co-flowing simulated combustion products.

4.2.4 Hot Co-flowing Simulated Combustion Products

With pre-heated simulated combustion products, the flame structure turns to be quite different comparing with all the other cases. For co-flowing pre-heated air case, the outer flame start to

oscillate at a very low frequence which short exposure time can reduce the uncertainty when image gets captured, but with co-flowing simulated combustion products, the outer flame becomes highly unstable which the flame oscillate at much higher frequency. In some CH* images, multiple outer flames with different location have been captured in a single frame. In Figure 4.34, it shows at least two outer flame has been captured when pre-heated co-flowing simulated combustion products is running with a small velocity. This is primary due to the co-flow which got pre-heated at the premix chamber does not have a uniformed velocity at the exit of burner top since the heating of co-flow is done at the wall surface, and low oxygen concentration co-flowing simulated combustion products mix with central fuel to form the mixture which is too rich, reaction can only occur when the mixture travels to the higher elevation to mix with the entrained air. To compare with the other co-flow conditions, the outer flame distributed away from center axis similar to pre-heated co-flowing air case, and also CH* emission is much lower which the dark outer flame from inverted CH* pictures turns to light gray color. This kind of outer flame only appears at flame configuration ⑥ in pre-heated co-flowing air case which the effect of co-flowing air is not dominating outer flame. The low CH* emission at outer flame located occurs in all flame types with pre-heated co-flowing simulated combustion products running. With different composition of co-flow gas, the

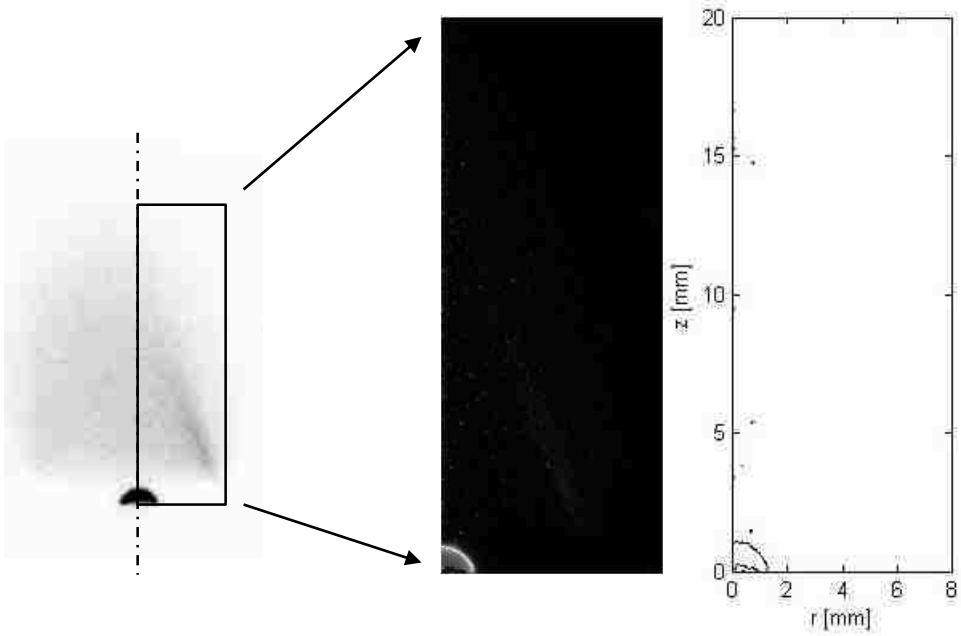

Figure 4.35: Sample image of flame configuration ②, inverted CH* image (left), CH* image after Abel transform (middle) and CH* contour (right). In this case, central air velocity u_{ca}=17.59 cm/s, central fuel velocity u_{cf}=9.47 cm/s, and co-flow velocity $u_{co\text{-}flow}$=3.53cm/s

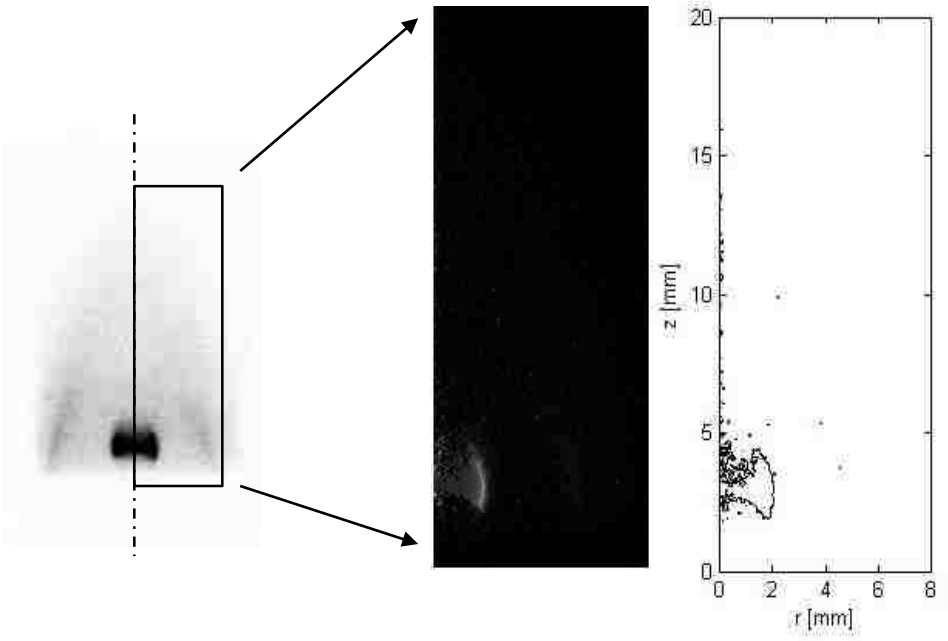

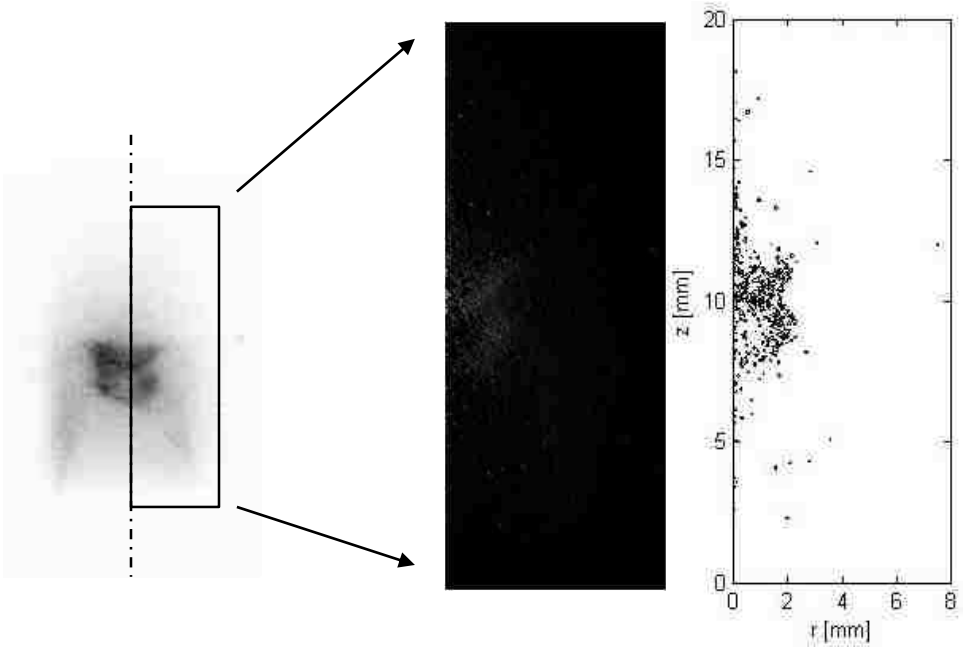
20
15
10
5
0
z [mm]
0
2
4
6
8
r [mm]

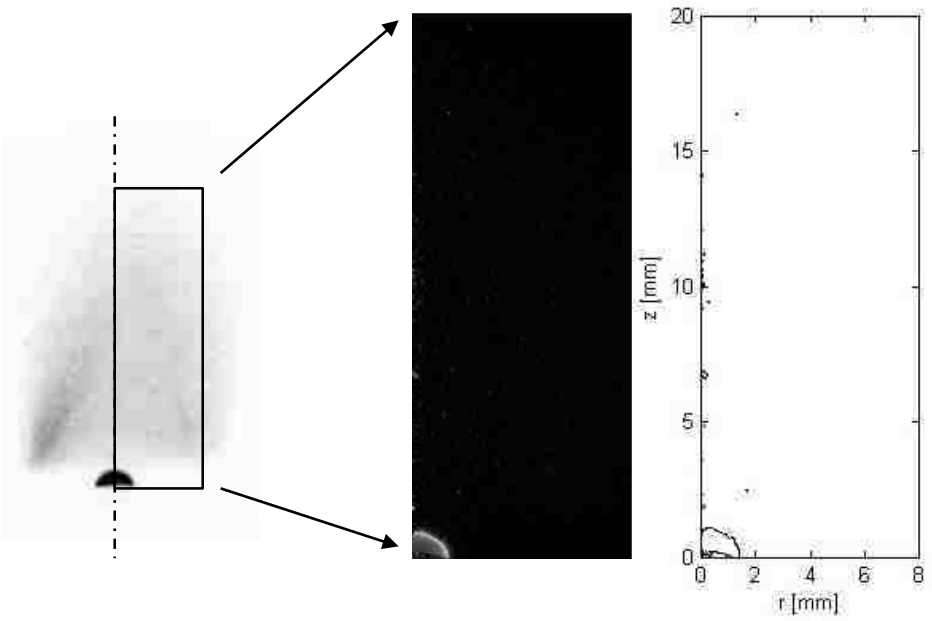
20
15
10
5
0
z [mm]
0
2
4
6
8
r [mm]

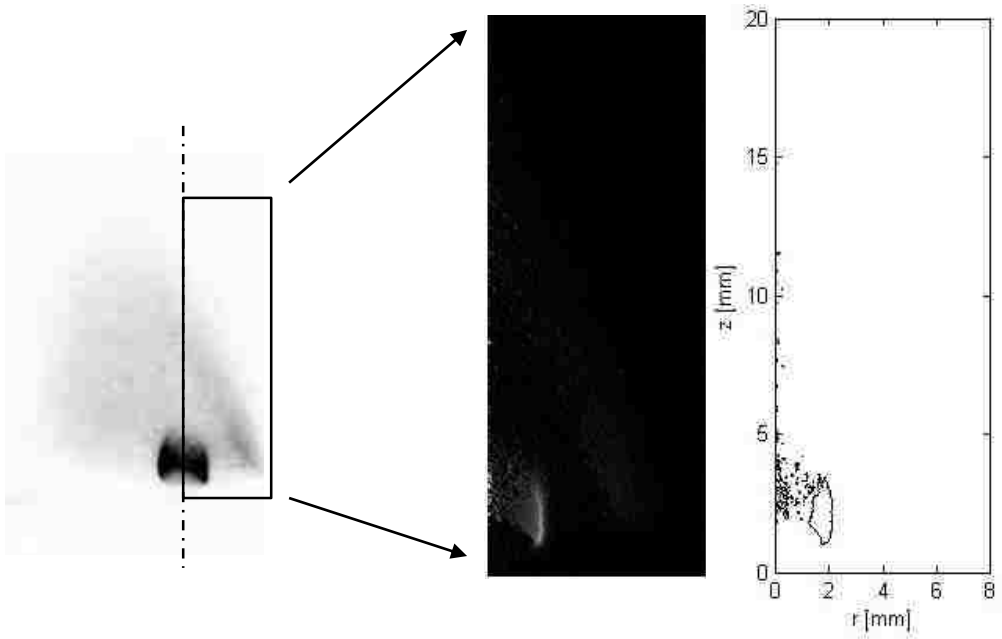
20
15
10
5
0
z [mm]
0
2
4
6
8
r [mm]

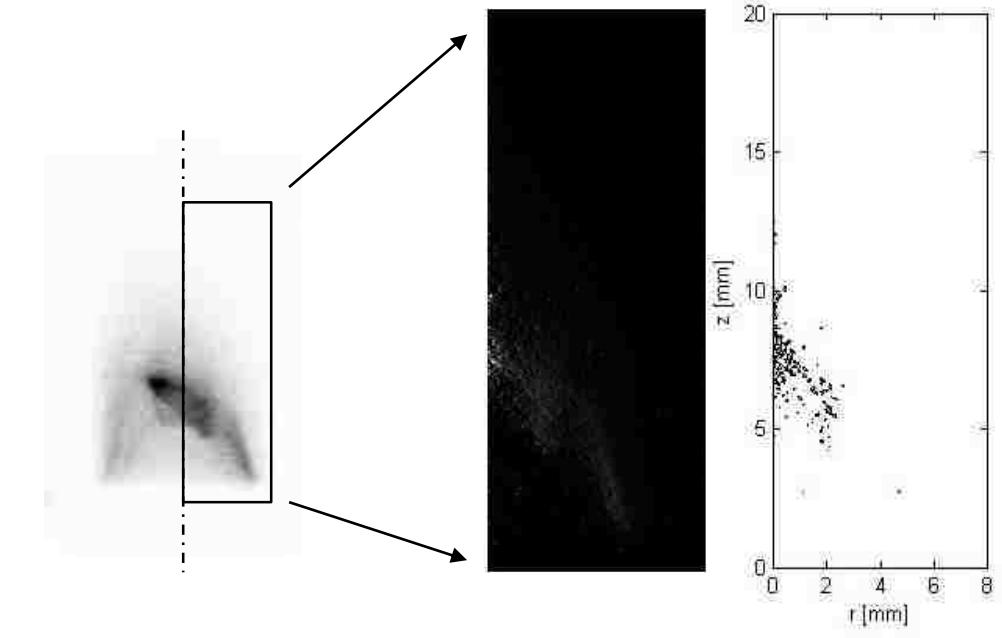
20
15
10
5
0
z [mm]
0
2
4
6
8
r [mm]

CH* behaviour at outer flame changes dramastically. Low oxygen concentration mixture of central fuel and co-flow mixture delays combustion which provides extra mixing time, and higher the chance more distributed reaction zone can be created.Another factor plays that an important role is pre-heating of co-flow, comparing with non-preheating simulated combustion products, igniting the mixture of central fuel and co-flow at ambient tempeature only forms outer flame with thin flame fronts. As co-flow gets pre-heated, the velocity of co-flow at exit of the nozzle is increasing spontenously, and density of co-flow is deceasing as well. By pre-heating the co-flow, the phsical properties of the laminar jet becomes quite different comparing with ambinent conditions. In reality of the experiments, the co-flow is pre-heated inside the burner, meanwhile ambient air surrounded the burner gets pre-heated as well. In results, the hot laminar co-flow jet expands away from center axis after exiting the nozzle, more distributed reaction zone can be formed when combustion occurs, and that is the primary reason in pre-heated co-flowing air case, a low CH* emission outer flame can be observed for flame flame configuration ⑥. By the book of "Combustion and Mass Transfer" (Spalding, 2013), it points out the correlation between the width of a jet and radius at which the jet velocity has one half its axial velocity:

$$\frac{r_{\frac{1}{2}}}{x} = 1.287\left(\frac{8\upsilon}{3I_u}\right)^{\frac{1}{2}} \tag{4.1}$$

where $r_{\frac{1}{2}}$ is the radius at which the jet velocity has one half its axial velocity, x is the width of the jet, υ is defined as $\upsilon \equiv \frac{\mu}{\rho} = \frac{\Gamma}{\rho}$, and μ is viscosity, ρ is density, Γ is exchange coefficient of fuel gas, I_u is defined as $I_u \equiv \upsilon^{-1}\int_0^\infty u^2 r dr$ and u is axial velocity and r is the radius. When the laminar flow gets pre-heated, viscosity and density is decreasing, and axial velocity is increasing, if assuming $r_{\frac{1}{2}}$ does not change in this case, the width of the jet is increasing, and the jet travels to wider position which favors to form a unified mixture of central fuel and co-flow gas.

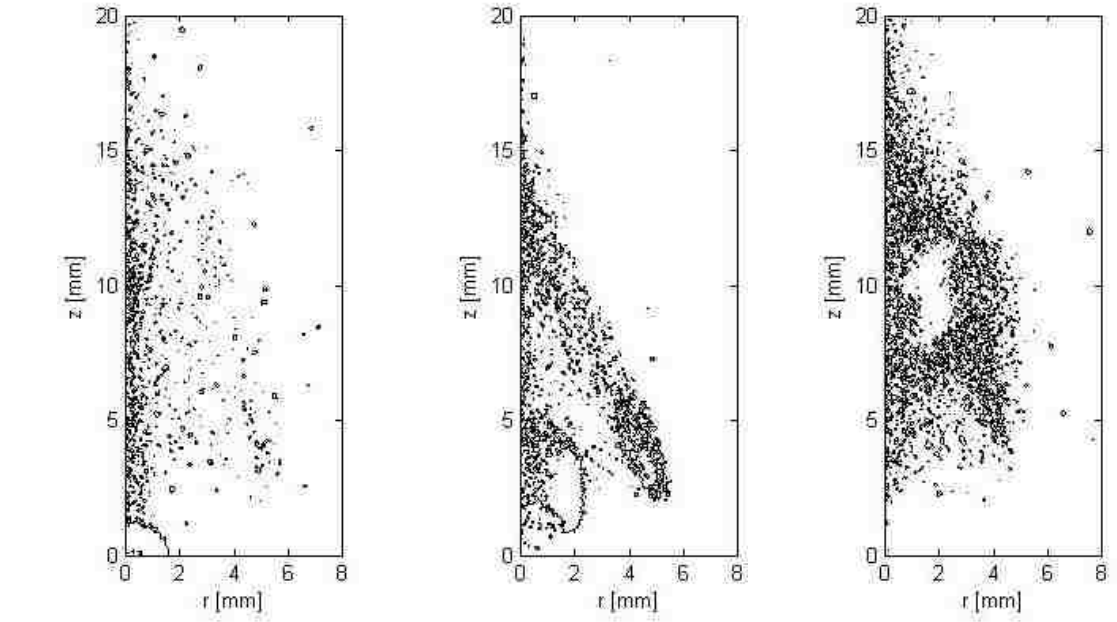
z [mm]
r [mm]
0
5
10
15
20
0
2
4
6
8

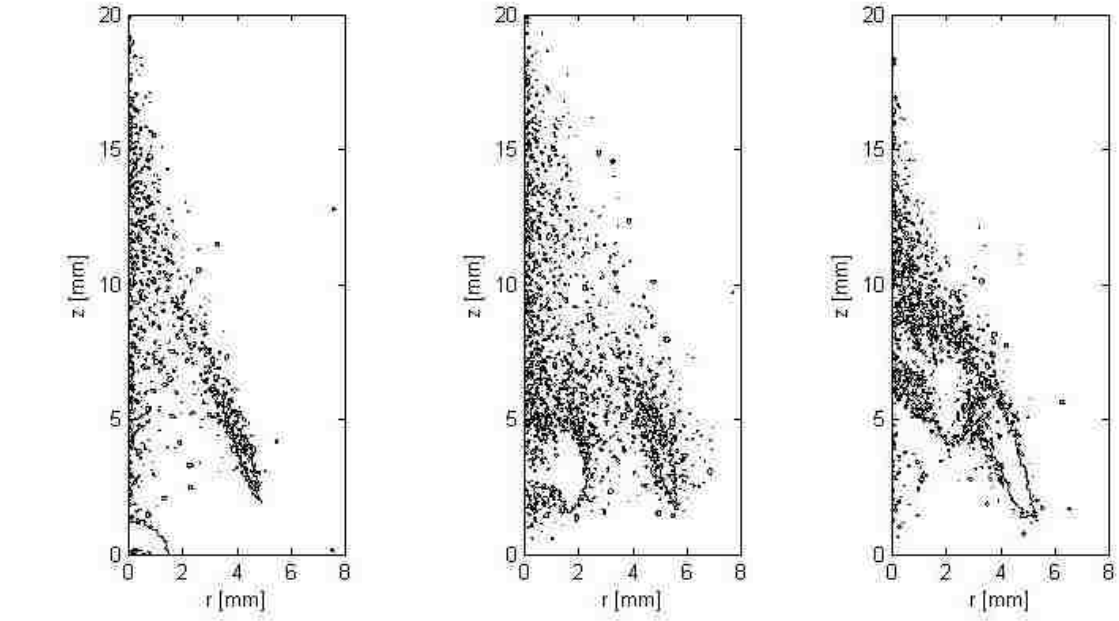
z [mm]
r [mm]
0
5
10
15
20
0
2
4
6
8

From Figure 4.35 to Figure 4.40, relative CH* contours with 20% filter on is a little bit miss leading because outer reaction zone or outer flame region do exist in these conditions, but they get filtered out to look like there is no reaction in these region. When only values low than 5% of the peak pixel value are filtered, the CH* contours show the distribution of CH* at outer flame region more close to the actual acquired images. In all cases, they shows no clear thin flame front which existed in non-preheating cases and pre-heated co-flowing air case, instead small CH* pockets is formed and concentrated at the region outside inner flame. Especially in flame configuration ⑥ in Figure 4.41, the CH* is minimum outside inner flame. The pockets of CH* distributed from center axis to almost 8 mm in radius. The characteristics of outer flame region in this flame type is match with the description of a distributed reaction zone. Despite there is a very dim visible flame exists in the outer flame region, the CH* contours shows the characteristics which can also been identified in flameless oxidation mode. With pre-heated co-flowing simulated combustion products, the flame structures are changed towards a more uniformed reaction as the reaction does not occur at one particular thin region, and the reaction occurs across the center axis to further more away from it.

4.3 Flame Structure Based On Temperature Measurements

To find out more firm evidence of flame structure change which towards flameless oxidation mode, temperature measurements has also been introduced to explore the temperature distribution inside reaction zone. Temperature data points have been measured at four different elevation for flame configuration ⑥ in Figure 4.41 as under this operation condition, the flame structure is showing most promising behaviour that flameless oxidation could happen. As Figure 4.42 indicates, the peak temperature appears above 1200℃ since inner flame presented at lowest elevation. Moving to higher elevation, 3 mm and 5 mm above the burner surface, the measured points located in the gap between inner flame and outer flame which is shown in Figure 4.43. There is no reaction occurring in the gap region, so the temperature of these two levels is not higher

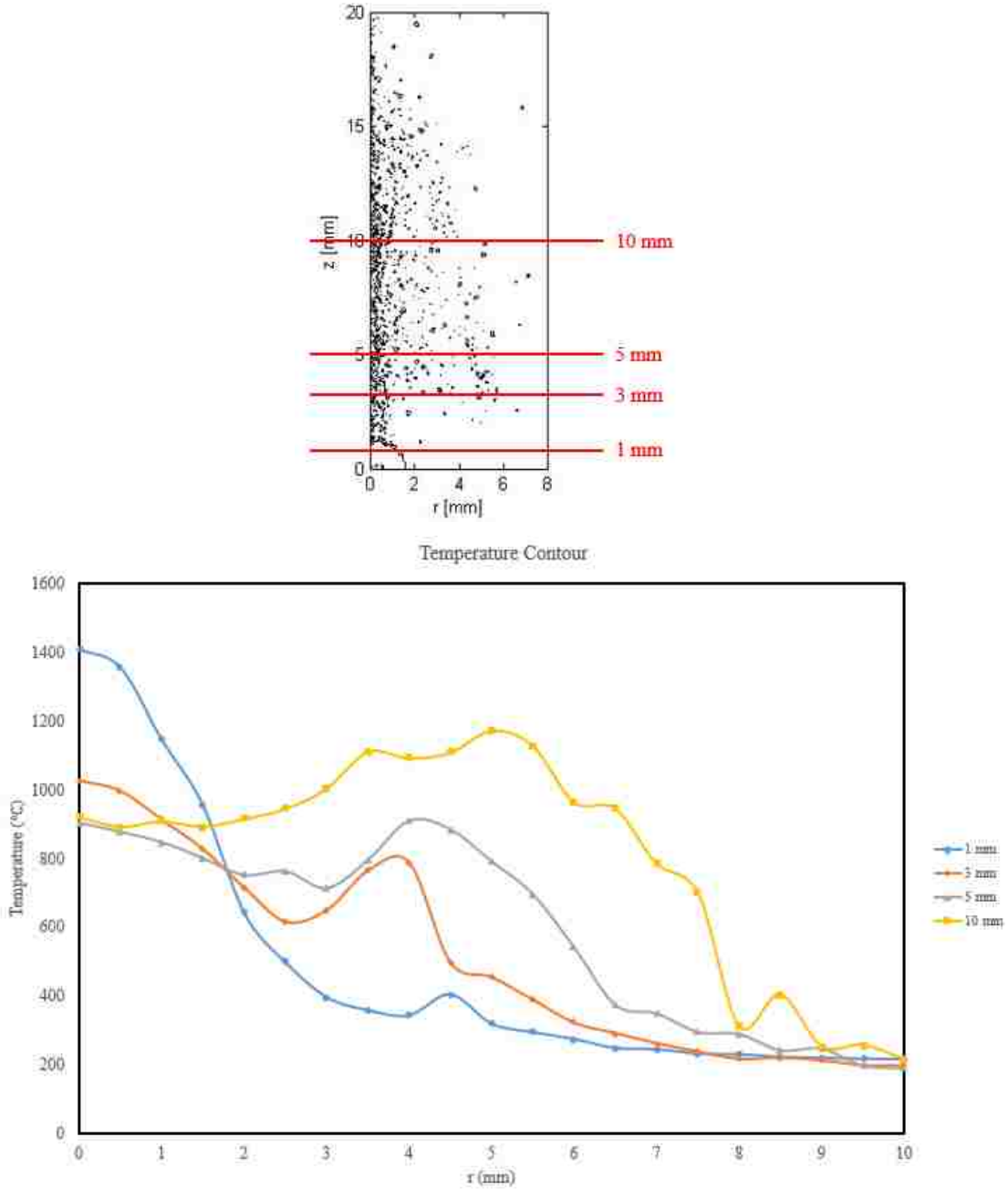

Figure 4.42: CH* contour of flame configuration ⑥ for IDF with pre-heated co-flowing simulated combustion products (top); temperature profile of flame configuration ⑥ for IDF with pre-heated co-flowing simulated combustion products at 1mm, 3mm, 5mm and 10mm above burner surface

than 900℃. Without heat transfer of both inner flame and outer flame to gap region, the temperature in this zone could be much lower. At the level of 10mm away from burner surface, the peak temperature becomes much higher as it enters outer flame region. CH* distribution of this flame indicates outer flame radius is no more than 6mm, and the difference between peak and minimum temperature inside the outer. flame is around 300℃. Temperature contour inside outer flame indicates the temperature is more uniformly distributed, and peak region appears close to the edge of outer flame The uniform distribution of temperature is the essential feature when distributed reaction zone occurs, and temperature distribution at 10 mm away from burner top is tending to match the feature. Both CH* distribution and temperature contour of this flame type somehow confirms the flameless oxidation occurs at the outer flame region in this type of flame structure.

Meanwhile as the temperature contours help to confirm the flameless oxidation, there are experimental uncertainties caused by the nature of temperature measurements. Figure 4.44 shows how the thermocouple and flame interact with each other, and in results the uncertainty occurs. When thermocouple in this setup expose to the high temperature region when flame presents, the entire exposed wire gets heated up, and this phenomenon affects the temperature reading from the

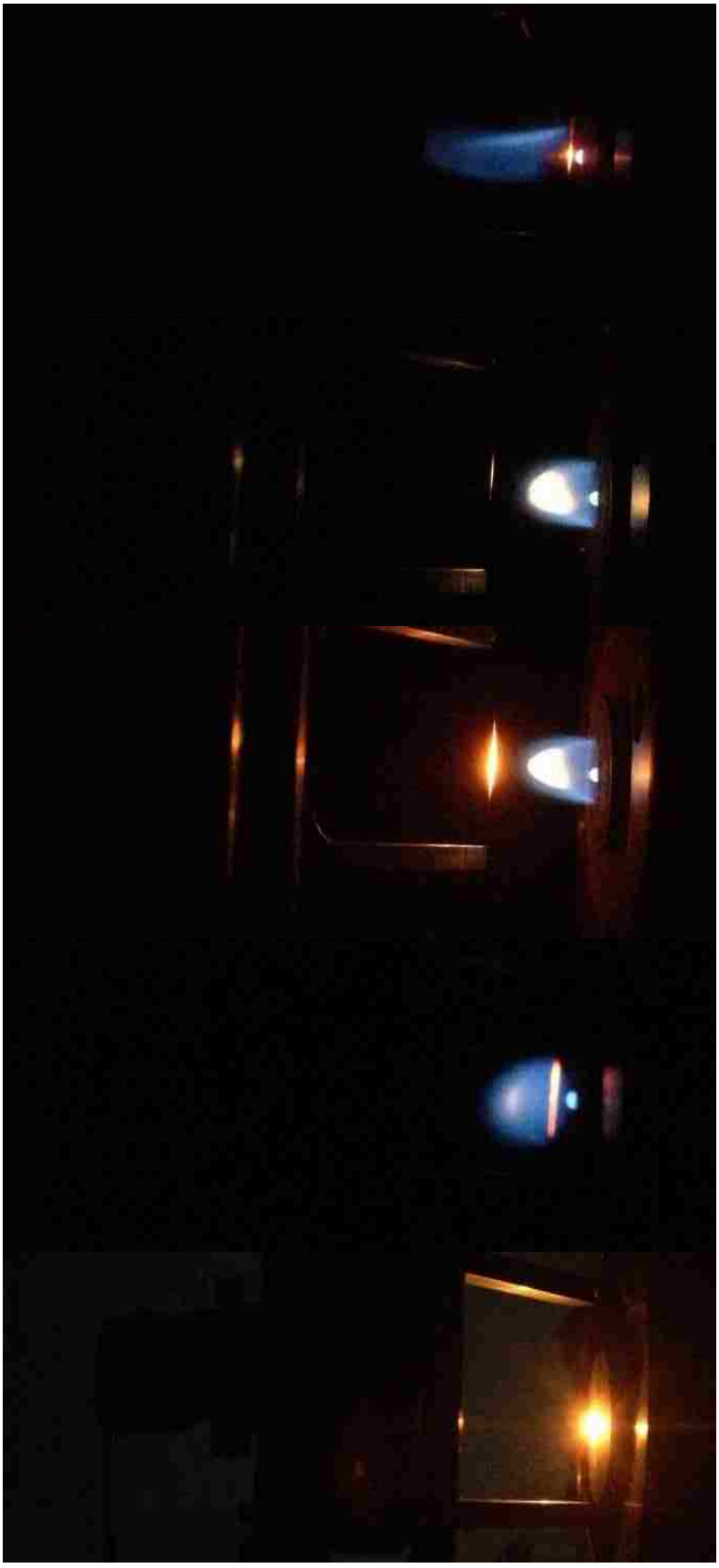

bead. In Figure 4.44, the four pictures on the left shows how the thermocouple presents at different height when temperature measurements have been taken. In all four pictures, the thermocouple wire is more or less got heated up. In results, due to the heat transfer on the wire, the measured temperature is higher than actual temperature. Another feature which is the cause of uncertainty occurring is when thermocouple enters the flow field of the flame, it changes flame position as the flow has been changed as well. As the last picture in Figure 4.44 is showing, when flame moves to the higher elevation when thermocouple presents inside the flame, the actual position of the flame should be lower in this picture. Because of the same reason, the temperature measurement results at 3mm and 5mm away from the burner surface in Figure 4.42 looks similar. At the level of 5mm, the bottom edge of outer flame is supposed to be located at, and the peak temperature should be higher than the measured data. In reality, when thermocouple traversed at 5mm level, the entire outer flame moved to higher elevation, so the gap between inner flame and outer flame became larger. In results, the temperature measured at 5 mm level is the temperature in the gap region instead of the temperature at the bottom of the flame. Flame with small mass flow rate of fuel and oxidizer, the intrusion of thermocouple could result in a large flow field change. When thermocouple expose to the region where large amount of soot get produced from the flame, the soot would accumulate on the thermocouple wire which is another source can measurement uncertainty could have. Because of these uncertainties which temperature measurement could have, the temperature measurement results is mainly served as a reference to validate CH* distribtuion measurement.

CHAPTER 5

Summary/Conclusions/Future Work

The structure of nominally non-premixed methane-air flames with several co-flow selections was studied experimentally under different operating conditions and reactant delivery configurations which favour flameless oxidation and fuel reformation. The flow arrangement of the burner is inversed delivery of methane and air, surrounded with co-flow. Several delivery methods have been studied with the central air tube raised above the burner surface, and angled fuel stream delivery with an inverted cone installed. Four kinds of co-flow have been tested namely air, nitrogen, combustion products produced a premixed lean flat methane/air flame at $\varphi = 0.78$ and simulated combustion products. The simulated combustion products have the same composition of exhaust gas generated from the premixed lean flat flame, except the water portion is replaced by nitrogen. The co-flow is pre-heated to temperature which enhance flameless oxidation and fuel reformation mechanisms.

- **Co-flow of combustion products from the premixed flame**

With co-flow of combustion products produced by the premixed lean flat flame at $\varphi = 0.78$, the flame is comprised of an inner inversed flame and an outer normal diffusion flame. As fuel flow enters the combustion products from a flat flame, the outer diffusion flame broadens its radius. The broadening of this diffusion flame is even more pronounced for the angled fuel delivery with inverted cone installed. By raising the central air tube to the same level, the broadening phenomenon is less pronounced than what can be observed from the angled fuel delivery. The extra mixing time provided by delaying the combustion taking place between fuel and oxidizer from angled fuel delivery allows to form a more homogeneous mixture. The broadening phenomenon is strongly related to the homogeneity of fuel and oxidizer mixture. The temperature of combustion products directly coming from the flat flame is far greater than the temperature which fuel reformation and flameless oxidation could occur.

- **Co-flow of simulated and pre-heated combustion products and air**

Distinct eight flame structures have been identified for varied central air and co-flow velocities when no pre-heating was applied. Pre-heating (both air and combustion products) brings in an additional destabilizing effect. The number of the stable flame structures is reduced to six, as two of the original structures are replaced with more stable configurations. The inversed diffusion flame space diagram is proposed to illustrate these configurations, and the relation of flame structure change with variation of central air and co-flow velocities. Replacing co-flow of air with co-flow of simulated combustion products introduces instability; stable flame structures are feasible only at dramatically reduced co-flow velocities. Experimental CH* distributions indicate that at some operating conditions (pre-heated combustion products and higher flow velocities) the flameless oxidation can indeed occur. The CH* is scattered across the extended reaction zone as no flame front can be identified. The temperature measurement results confirmed this trend and the potential for flameless oxidation. The area of ultra-high temperature region has reduced with more uniformed temperature distribution across the reaction zone, and peak temperature has decreased. With co-flowing simulated combustion products, the mixing time of fuel, oxidizer and co-flow gets extended to form a more homogeneous mixture before combustion taking place. The extended reaction zone favours flameless oxidation to occur. Pre-heating of co-flow reduces the co-flow density, and co-flow can expand more broadly to mix with other jet. This mixing enhancement helps to form the extended reaction zone as well. As the extended reaction zone in the inner flame region strongly depends on the co-flow conditions, precise specification of all the co-flows is critical to achieve flameless oxidation and fuel reformation.

- **Future Work**

For the follow up work, by careful adjustments of the pre-heating temperature and flow rate of the co-flowing combustion products, the flameless oxidation zone can be verified, and fuel reformation zone will be finally identified with numerical simulation. Optimizing the data selection by improving online image processing program is needed to overcome the instability of the

inversed diffusion flame. The mixing time of central fuel and co-flow can be further elongated by different flow arrangement before combustion occurs.

REFERENCES

Alejo, L., Lago, R., Pena, M., & Fierro, J. (1997). Partial oxidation of methanol to produce hydrogen over cu/ zn-based catalysts. *Applied Catalysis A: General, 162*(1), 281-297.

Bell, R. D., & McGill, E. C. (1983). Process for Reduction of Oxides of Nitrogen. *Google Patents.*

Burke, S. P., & Schumann, T. E. W. (1928). Diffusion flames. *Industrial & Engineering Chemistry, 20*(10), 998-1004.

Cho, E., Danon, B., De Jong, W., & Roekaerts, D. (2011). Behavior of a $300kW_{th}$ regenerative multi-burner flameless oxidation furnace. *Applied Energy, 88*(12), 4952-4959.

Crosley, D. R. (1989). Semiquantitative laser-induced fluorescence in flames. *Combustion and Flame, 78*(1), 153-167.

Danon, B., De Jong, W., & Roekaerts, D. (2010). Experimental and numerical investigation of a FLOX combustor firing low calorific value gases. *Combustion Science and Technology, 182*(9), 1261-1278.

Devriendt, K., Van Look, H., Ceursters, B., & Peeters, J. (1996). Kinetics of formation of chemiluminescent CH (A 2 Δ) by the elementary reactions of C 2 H (X 2 Σ+) with O (3 P) and O 2 (X 3 Σ g−): A pulse laser photolysis study. *Chemical physics letters, 261*(4), 450-456.

Flamme, M. (2004). New combustion systems for gas turbines (NGT). *Applied Thermal Engineering, 24*(11), 1551-1559.

Grandmaison, E. W., Yimer, I., Becker, H. A., & Sobiesiak, A. (1998). The strong-jet/weak-jet problem and aerodynamic modeling of the CGRI burner. *Combustion and Flame, 114*(3), 381-396.

Haryanto, A., Fernando, S., Murali, N., & Adhikari, S. (2005). Current status of hydrogen production techniques by steam reforming of ethanol: A review. *Energy & Fuels, 19*(5), 2098-2106.

Haynes, B. S., & Wagner, H. G. (1981). Soot formation. *Progress in Energy and Combustion Science, 7*(4), 229-273.

Higgins, B., McQuay, M., Lacas, F., & Candel, S. (2001). An experimental study on the effect of pressure and strain rate on CH chemiluminescence of premixed fuel-lean methane/air flames. *Fuel, 80*(11), 1583-1591.

Hoang, D., & Chan, S. (2004). Modeling of a catalytic autothermal methane reformer for fuel cell applications. *Applied Catalysis A: General, 268*(1), 207-216.

Huang, Y., Yan, Y., Lu, G., & Reed, A. (1999). On-line flicker measurement of gaseous flames by image processing and spectral analysis. *Measurement Science and Technology, 10*(8), 726.

Jeong, Y. K., Jeon, C. H., & Chang, Y. J. (2006). Evaluation of the equivalence ratio of the reacting mixture using intensity ratio of chemiluminescence in laminar partially premixed CH 4-air flames. *Experimental Thermal and Fluid Science, 30*(7), 663-673.

Johnson, M. B. (2009). *Methane Inverse Diffusion Flames with Co-flowing Air and Combustion Products* (Doctoral dissertation). Retrieved from Ottawa: Library and Archives Canada = Biblioth èque et Archives Canada, 2012.

Johnson, M. B., & Sobiesiak, A. (2011). Hysteresis of methane inverse diffusion flames with co-flowing air and combustion products. *Proceedings of the Combustion Institute, 33*(1), 1079-1085.

Katta, V. R., Blevins, L. G., & Roquemore, W. M. (2005). Dynamics of an inverse diffusion flame and its role in polycyclic-aromatic-hydrocarbon and soot formation. *Combustion and Flame, 142*(1), 33-51.

Kojima, J., Ikeda, Y., & Nakajima, T. (2000). Spatially resolved measurement of OH*, CH*, and C 2* chemiluminescence in the reaction zone of laminar methane/air premixed flames. *Proceedings of the Combustion Institute, 28*(2), 1757-1764.

Kojima, J., Ikeda, Y., & Nakajima, T. (2005). Basic aspects of OH (A), CH (A), and C 2 (d) chemiluminescence in the reaction zone of laminar methane–air premixed flames. *Combustion and Flame, 140*(1), 34-45.

Mancini, M., Weber, R., & Bollettini, U. (2002). Predicting NO_x emissions of a burner operated in flameless oxidation mode. *Proceedings of the Combustion Institute, 29*(1), 1155-1163.

Mikofski, M. A., Williams, T. C., Shaddix, C. R., & Blevins, L. G. (2006). Flame height measurement of laminar inverse diffusion flames. *Combustion and Flame, 146*(1), 63-72.

Otsuka, K., Wang, Y., Sunada, E., & Yamanaka, I. (1998). Direct partial oxidation of methane to synthesis gas by cerium oxide. *Journal of Catalysis, 175*(2), 152-160.

Pimentel, G. C., Bass, A. M., & Broida, H. P. (1960). Formation and Trapping of Free Radicals. *By AM Bass and HP Broida, Academic Press, New York*, 69-115.

Plessing, T., Peters, N., & Wünning, J. G. (1998, December). Laseroptical investigation of highly preheated combustion with strong exhaust gas recirculation. In *Symposium (International) on Combustion* (Vol. 27, No. 2, pp. 3197-3204). Elsevier.

Rabenstein, G., & Hacker, V. (2008). Hydrogen for fuel cells from ethanol by steam-reforming, partial-oxidation and combined auto-thermal reforming: A thermodynamic analysis. *Journal of Power Sources, 185*(2), 1293-1304.

Schefer, R. (1997). Flame sheet imaging using CH chemiluminescence. *Combustion Science and Technology, 126*(1-6), 255-279.

Snelling, D. R., Thomson, K. A., Smallwood, G. J., & Gülder, Ö. L. (1999). Two-dimensional imaging of soot volume fraction in laminar diffusion flames. *Applied Optics, 38*(12), 2478-2485.

Sobiesiak, A., Rahbar, S., & Becker, H. A. (1998). Performance characteristics of the novel low-NO x CGRI burner for use with high air preheat. *Combustion and flame*, *115*(1), 93-125.

Sobiesiak, A., & Wenzell, J. C. (2005). Characteristics and structure of inverse flames of natural gas. *Proceedings of the Combustion Institute*, *30*(1), 743-749.

Spalding, D. B. (2013). *Combustion and mass transfer: A textbook with multiple-choice exercises for engineering students* Elsevier.

Sze, L., Cheung, C., & Leung, C. (2004). Temperature distribution and heat transfer characteristics of an inverse diffusion flame with circumferentially arranged fuel ports. *International Journal of Heat and Mass Transfer, 47*(14), 3119-3129.

Veríssimo, A., Rocha, A., & Costa, M. (2013). Importance of the inlet air velocity on the establishment of flameless combustion in a laboratory combustor. *Experimental Thermal and Fluid Science, 44*, 75-81.

Williams, A., & Smith, D. B. (1970). Combustion and oxidation of acetylene. *Chemical Reviews, 70*(2), 267-293.

Wu, K. T., & Essenhigh, R. H. (1985, December). Mapping and structure of inverse diffusion flames of methane. In *Symposium (International) on Combustion* (Vol. 20, No. 1, pp. 1925-1932). Elsevier.

Wünning, J., & Wünning, J. (1997). Flameless oxidation to reduce thermal NO-formation. *Progress in Energy and Combustion Science*, *23*(1), 81-94.

APPENDICES

Appendix A

Modified Chemiluminescence Imaging

The modification of chemiluminescence imaging program is based on a PhD dissertation project (Johnson, 2009). The CH* radical from flame chemiluminescence is imaged with Di-Cam Pro ICCD camera. This appendix provides a detailed description of modifications for the imaging processing program of Johnson (2009).

A.1 Centerline Finding

```
bw=im2bw(flame,60/250);
bwcrop=imcrop(bw,[1 678 1024 0]);
counter=0;
counter1=0;
for i=1:645
d=bwcrop(i);
if d==0
 counter=counter+1;
else
 break
end
end
rbw=imrotate(bwcrop, 180);
for j=1:645
d=rbw(j);
if d==0
 counter1=counter1+1;
else
 break
end
end
centerline=(1024-counter-counter1)/2+counter;
```

An example MATLAB codes to find the centerline from a flame image. The MATLAB image tool has been used to predetermine the pixel level where flame has the most symmetrical shape.

That value in this example is 678, and this value has later on be used to be the reference pixel level to determine the centerline. As the first line of the MATLAB code shows, the preloaded flame first gets converted to a binary image with the threshold value of 60/250. All the flame region converts to white color, and the rest is black. The binary image then gets cropped to a line of pixels and this location of the pixel line is chosen by the reference pixel level which has predetermined. Two

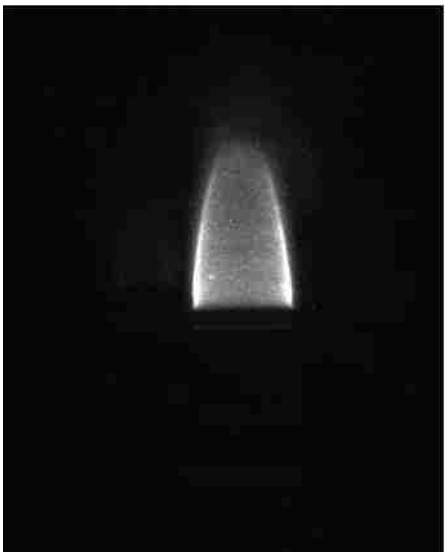

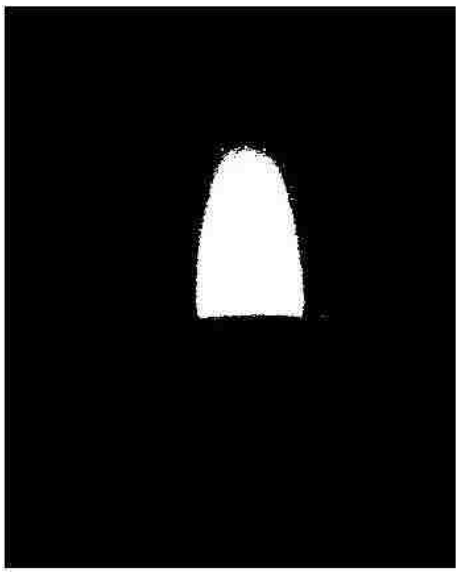

counters has been introduced to count from two side of the binary image, and they count the number of black pixels before they reaches the white pixels which is actually the flame region. The flame region can be determined from this pixel level, and the centerline is set to be half way of this flame region. This centerline determined from this reference pixel level is set as the centerline of this flame image.

A.2 CH Contour Plot*

```
c=[0.2];
dat=load(strcat('H:/141202/Process_Data/Abel_141202_',num2str(run),'.mat'));
figure;contour(dat.r,dat.z,dat.CHl,[c],'Linecolor','k');
axis image
ylim([0 20]);
ylabel('z [mm]');
set(gca,'YTick', (0:5:20));
set(gca, 'YTicklabel',(0:5:20));
xlim([0 8]);
xlabel('r [mm]');
set(gca,'XTick',(0:2:8));
set(gca, 'XTicklabel',(0:2:8));
```

This an example MATLAB code to plot the CH* contour. After completing the Abel transform, the transformed CH* image is saved with total radial length r and height z. The variable c is the filtering threshold value when the artificial filter has applied on the processed CH* image. The final CH* contour is plotted based on the threshold value c, total radial length r and height z.

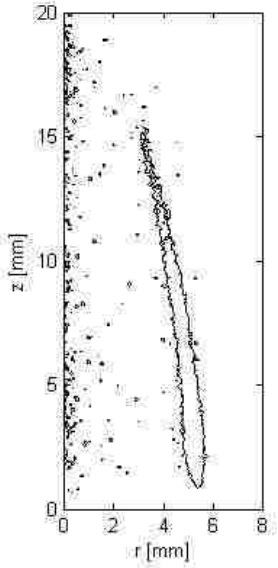

[redacted]

A.3 CH Image Color Inversion*

```
for run=2

flame=imread(strcat('H:/141202/141202_',num2str(run),'.tif'));

[hei,wid] = size(flame);

flame2=double(flame);

for i=1:hei

for j=1:wid

f=flame2(i,j);

g(i,j)=4096-f;

end

end

inverse=mat2gray(g);

figure,imshow(inverse)

end
```

This is an example MATLAB code for CH* image color inversion. As the flame image gets loaded to the program, the size of the image height and width is saved as *hei* and *wid*. Pixel value of flame image is formatted by function "*double*", the pixel value is falling in the range from 0 to 4096. The image later converts to the matrix *f*, and g matrix invert the *f* the pixel value. Function "*mat2gray*" brings *g* matrix back to a grayscale image. The *inverse* becomes the CH* image with color inversion image.

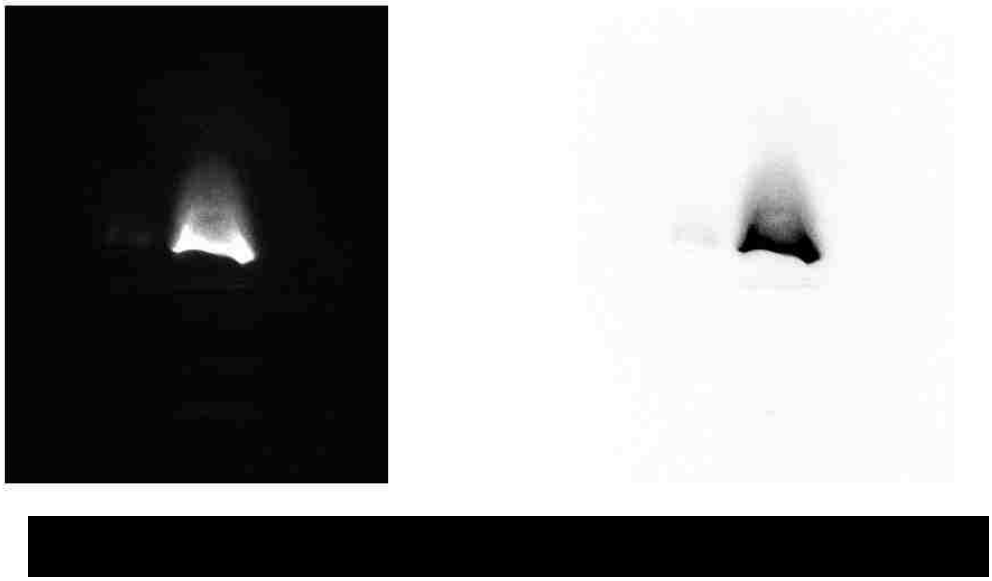

Appendix B

Temperature Monitoring and Measurement Program

In Chapter 2, it describes the temperature monitoring and meausrement system is conducted with a specified LabVIEW program. This appendix provide a detailed description of the LabVIEW program.

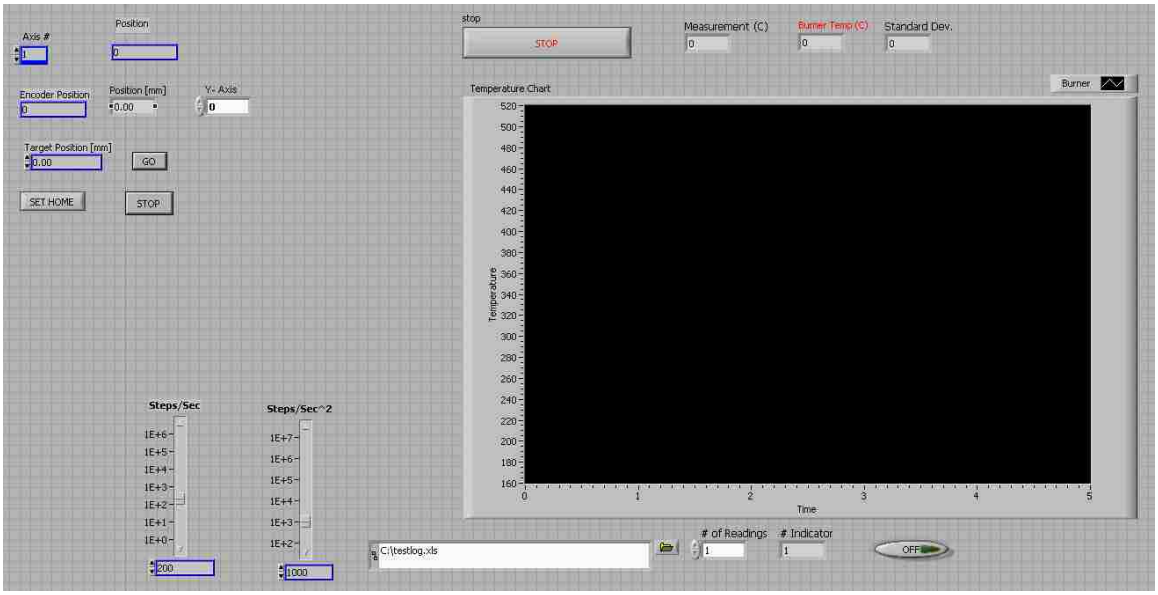

[redacted]

Figure A.4 shows the front panel of this LabVIEW program. It is in charge of controlling the traverse mechanism, monitoring burner temperature and temperature measurement of the flame. The module at the left corner controls the traverse mechanism. Two axis can be controlled, axis #1 is horizontal axis, and axis #2 is normal axis. The target position input sets the destination of traverse mechanism. The temperature chat on the right is displaying burner temperature from thermocouple inserted to the burner and temperature measured by thermocouple from the flame field. The standard deviation of flame temperature has been calculated as well by the program. The temperature monitoring of burner is running all the time once the program starts, and thermocouple measurement of the flame has an on and off button which is showing on the bottom right corner of

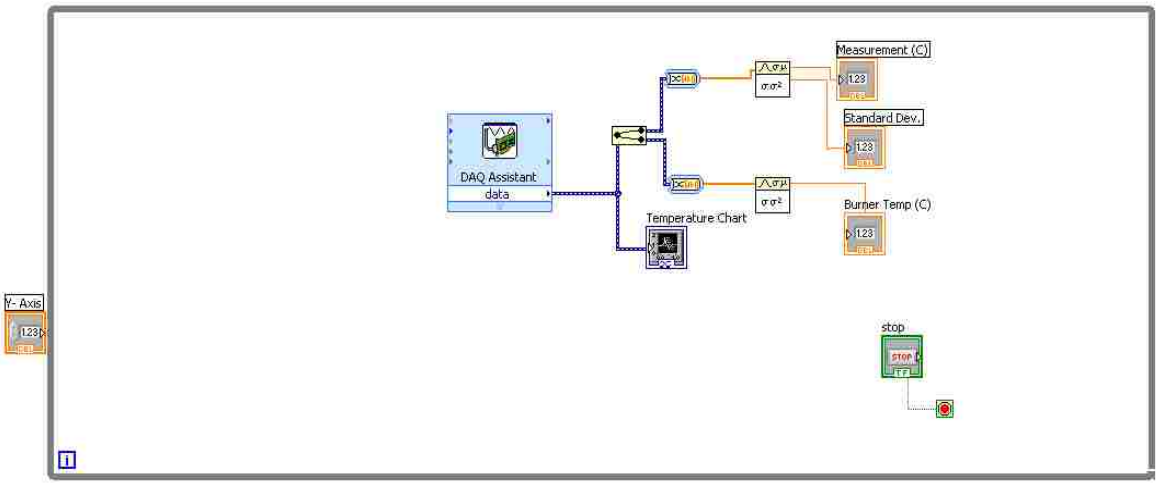
Measurement (C)
Standard Dev.
DAQ Assistant
data
Burner Temp (C)
Temperature Chart
Y- Axis
stop

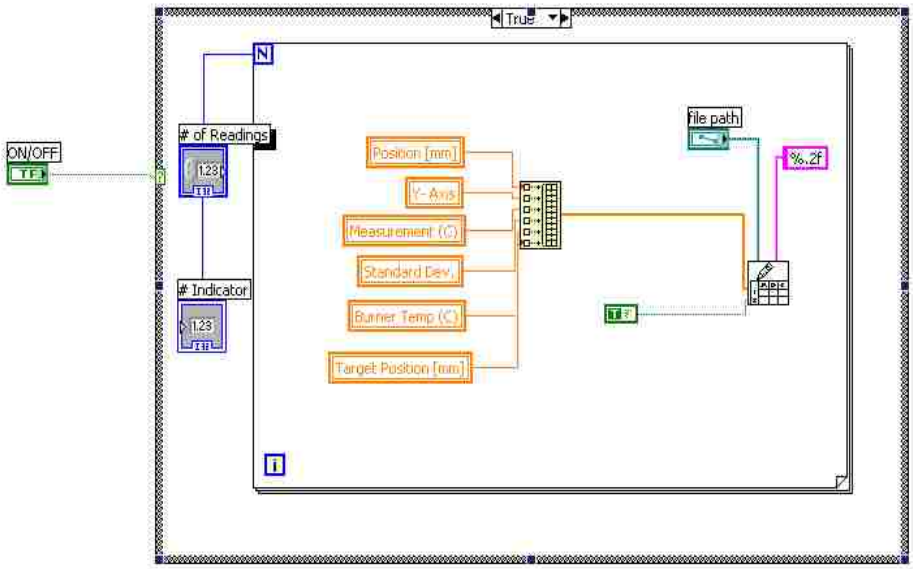
True
N
ON/OFF
# of Readings
file path
%.2f
Position [mm]
Y- Axis
Measurement (C)
Standard Dev.
Burner Temp (C)
Target Position [mm]
Indicator

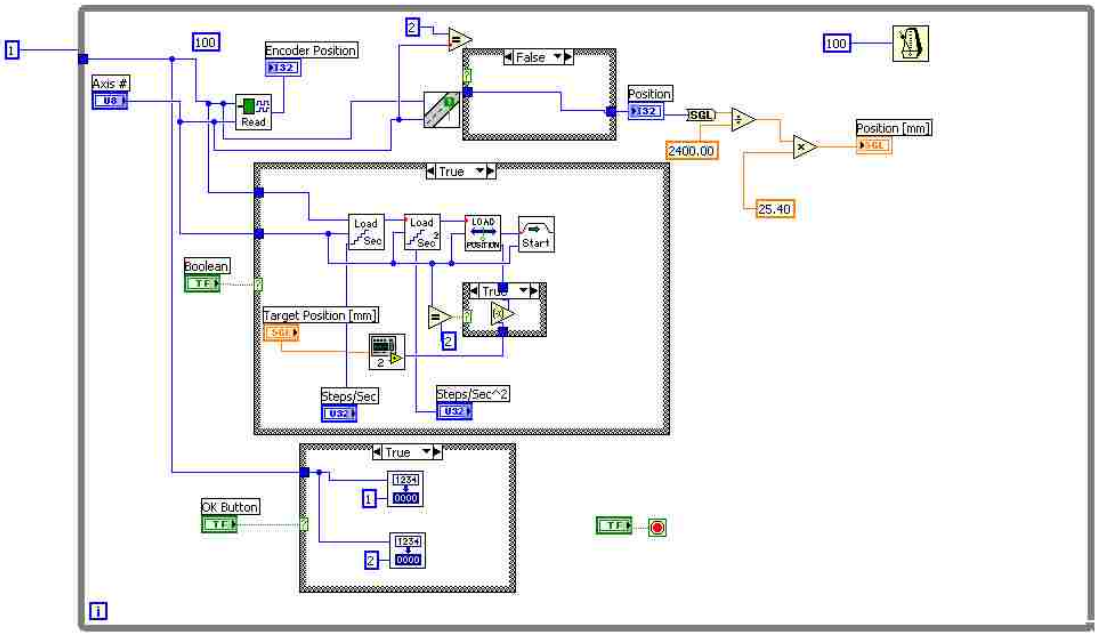

[redacted]

Figure A.4. The readings are saved to an Excel sheet which the path has been set initially. The number of reading which will be write to Excel sheet can be modified in "*# of readings*". From Figure A.5 to Figure A.7, they shows the block diagram of three different modules of the LabVIEW program. The modules are running independently to control the traverse mechanism, measure and monitor temperatures and record the measured temperature.

Appendix C

Flame Stability Measurement Program

The flame stability program has been explained in Chapter 2, the flame images are recorded through a webcam. This appendix describes the detail of the MATLAB program controlling the flame stability measurement system and online image processing.

```
clear all
clc
webcamlist;
cam=webcam(1);
counter=0;
for i=1:100
f=snapshot(cam);
imwrite(f,strcat('H:/Test/IMG_',num2str(i),'_snapshot.jpg'));
s=imread(strcat('H:/Test/IMG_',num2str(i),'_snapshot.jpg'));
fcrop=s(327:334,408:430,:);
imwrite(fcrop,strcat('H:/Test/IMG_',num2str(i),'_crop.jpg'));
BW=im2bw(fcrop,100/256);
q=nnz(BW);
total=numel(BW);
percentage_of_intrusion=q/total;
Y(i)=percentage_of_intrusion;
if sum(sum(BW))>1
   counter=counter+1;
else
   counter=counter;
end
num_of_pictures=counter;
end
Probability=counter/100
totalI=sum(Y)
clear('cam')
```

The MATLAB code showing above are serving the purpose for acquiring and processing the flame images. The stability measurement identifies an unstable flame which jumps into the region underneath certain flame height. The number of frames which flame jump into this region has been counted and how much is intrusion percentage has been calculated over 100 frames. The intrusion area is counted from converted image which acquired by the webcam.

The flame stability measurement quantifies the instability of a flame. Normally acquiring data from an unstable flame could have high uncertainty. The selection of data acquired from the unstable flame can be made based on the flame stability measurement to eliminate some sources for experimental uncertainty.

The image tool from MATLAB has been used to predetermine the capture area from image acquired by the webcam. In this case, it from pixel 327 to pixel 334 in normal direction, and from pixel 408 to pixel 430 in horizontal direction. This 22 pixels by 7 pixels region is preset to be the area of interest.

Once the acquiring and processing starts, the webcam will capture the first image. The first image then is cropped that only area of interest is left. Function "*im2bw*" converts the cropped image to binary image with a threshold value which in this case is 100/256. After this process, the flame region in the cropped image becomes white, and rest is black. Function "*nnz*" counts number of white pixels in the cropped image, and function "numel" is taking charge of counting the total pixels in the cropped image. The percentage of total white pixels in the image which is defined as intrusion level per frame is calculated by:

$$intrusion\ level = \frac{number\ of\ white\ pixels}{total\ number\ of\ pixels}$$

The total intrusion level is calculated by the summation of intrusion percentage over 100 frames. Another parameter can be calculated is number of times flame jump into the area of interest over 100 frames. After the cropped image converts to binary image, an *if* loop start to count number of

frames which flame has intruded over 100 frames. The percentage of flame intrusion is calculated by:

%Probability=counter/100%

The calculation of flame intrusion percentage and total intrusion level helps the selection of experimental data. The primary selection reference is intrusion percentage, because there is much less chance of flame will jump into the area of interest in a stable. Sometimes, the percentage of flame intrusion could be the same from two measurements. The total intrusion level serve the purple to distinguish this two measurements. As more stable the flame is, the value of total intrusion level would be less. Figure A.8 shows how the acquired images gets processed in the MATLAB program.

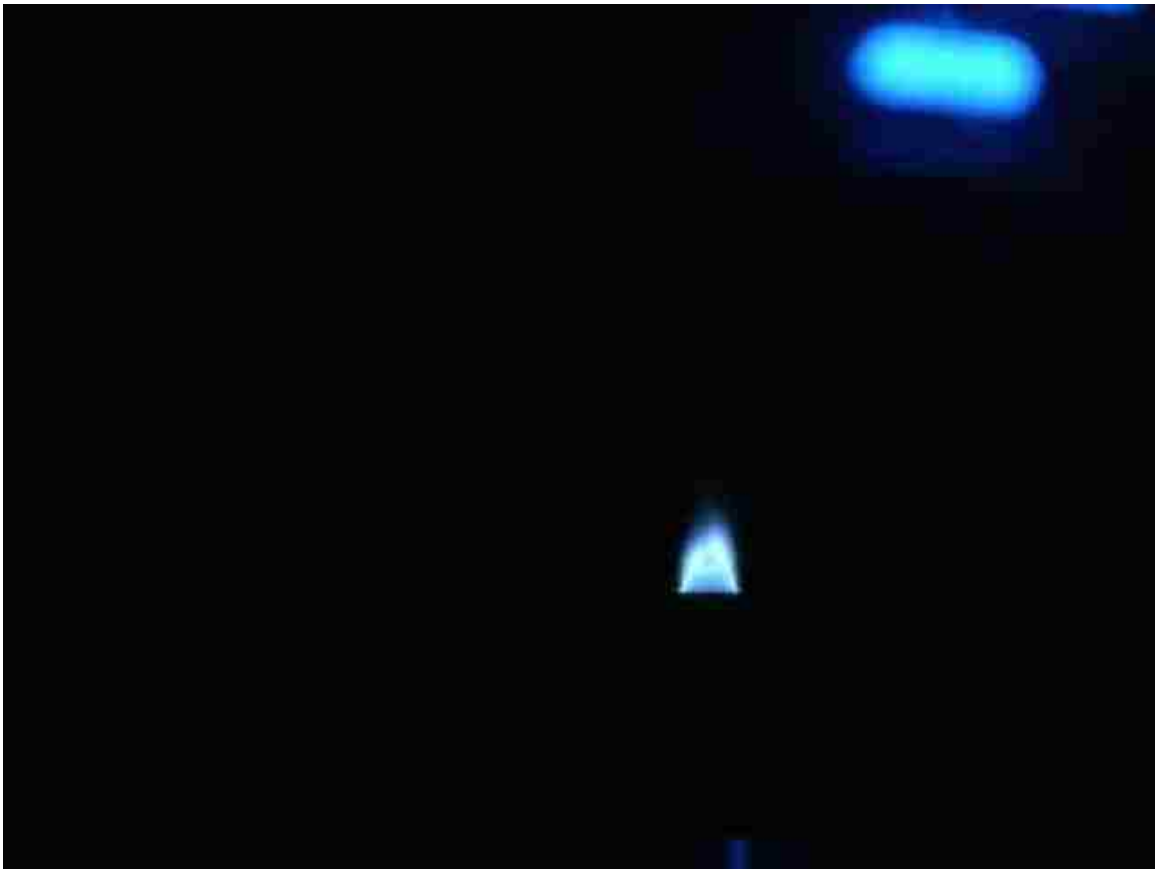

VITA AUCTORIS

NAME:	Xisheng Zhao
PLACE OF BIRTH:	Chengdu, Sichuan, P.R. China
YEAR OF BIRTH:	1988
EDUCATION:	University of Windsor, B.A.Sc. in Mechanical Engineering (Automotive option), Windsor, ON, 2011
	University of Windsor, M.A.Sc in Mechanical Engineering., Windsor, ON, 2015